

Diss. ETH No. 29011

Acoustic Robot Gripper

A thesis submitted to attain the degree of

DOCTOR OF SCIENCES of ETH ZURICH
(Dr. sc. ETH Zurich)

presented by

MARC FABIAN RÖTHLISBERGER

MSc ETH

born on 06.08.1995

citizen of Ballwil, Switzerland

accepted on the recommendation of

Prof. Dr. Johann W. Kolar, examiner
Prof. Dr. Elena Lomonova, co-examiner

2023

ETH Zurich
Power Electronic Systems Laboratory
Physikstrasse 3 | ETL H23
8092 Zurich | Switzerland

<http://www.pes.ee.ethz.ch>

© 2023, Marc Röthlisberger

Acknowledgments

I would like to thank everyone who supported me during my time at ETH Zurich and the Power Electronic Systems Laboratory.

First, I would like to express my sincere gratitude to Prof. Dr. Johann W. Kolar for the opportunity to carry out this PhD thesis at his institute and for his support during the entire research.

Furthermore, I would like to thank Prof. Dr. Elena Lomonova for co-examining my PhD thesis.

I would also like to thank Prof. Dr. Jörg Hugel for his financial support through the Else & Friedrich Hugel Fund. His interest in my research was always a motivating factor.

I also want to thank my co-doctoral students for the pleasant time, great discussions and exciting events. The atmosphere in the office, in the laboratories and in the coffee room was always very comfortable.

Special thanks go to Dr. Marcel Schuck for his extraordinary support during my time at the Power Electronic Systems Laboratory. His encouragement and motivation was very important for the outcome of my thesis. His assistance for my research and especially for publications was very important to make this work possible. I would also like to thank him for the great time at Technopark and ieLab.

I am very thankful to Dr. Pascal Püntener, Dr. Marcel Schuck and the employees of Levitronix GmbH for the pleasant working atmosphere during the time at Technopark.

Furthermore, I am grateful for all students who conducted their bachelor thesis, studies on mechatronics, semester thesis, or master thesis under my supervision. Their motivation and interest in my research was inspiring and resulted in valuable contributions to this work.

Last but not least, I would like to thank my family for their great support which kept me motivated throughout my studies at ETH Zurich.

Zurich, October 2022

Marc Röthlisberger

Abstract

MANUFACTURING processes are more and more automated by robotic grippers in order to save costs, increase the quality of the products and to be able to produce larger quantities. However, for the transport of small and fragile objects, there are often no grippers capable of transporting the objects without damage. In order to be able to automate such processes in the future, contact-less grippers, which can pick up, transport and position objects on a target without mechanical contact using ultrasonic waves, are developed in this work.

Acoustic levitation forces can be used to manipulate small objects and liquid droplets without mechanical contact or contamination. To use acoustic levitation for contact-less robot grippers, automated insertion of objects into the acoustic pressure field is required. This work presents analytical models based on which concepts for the controlled insertion of objects are developed. Three types of acoustic grippers are implemented and used to experimentally verify the lifting of objects into the acoustic field. Lifting high density objects ($\rho \leq 7.3 \text{ g/cm}^3$) from acoustically transparent surfaces is demonstrated using a double-sided robot gripper and standing acoustic waves with dynamic adjustment of the acoustic power. A single-sided gripper using a combination of different acoustic traps is used to lift lower density objects ($\rho \leq 0.1 \text{ g/cm}^3$) from acoustically reflective surfaces. A third method presented in this work uses a gripper with a thin and moveable reflector and standing acoustic waves to lift high density objects ($\rho \leq 7.3 \text{ g/cm}^3$) from acoustically reflective surfaces.

A novel method for the stabilization of objects levitating in the gripper during the transport is presented and compared to state-of-the-art stabilization methods. Novel manipulation methods are investigated, which can be used to deposit the levitating object on a target. A closed-loop control system is designed to achieve high precision position and orientation control.

Apart from transporting solid objects, ultrasonic forces can also be used for the transport of liquid droplets. This can be used for the contamination-free transport of substances, for which physical contact with syringes or pipettes would cause chemical reactions. In this work, a gripper was developed, which is capable of transporting liquid droplets in the micro litre range. It uses ultrasonic pulses to eject droplets from a liquid pool and a novel droplet levitator, which can catch the ejected droplet. This device presents the first air-coupled droplet ejector and

the first contact-less method for the insertion of liquid droplets into an acoustic levitation field.

The provided results open up new possibilities for the implementation of acoustic levitation methods in robotic grippers, which have the potential to be used in a variety of industrial applications.

Kurzfassung

PRODUKTIONSPROZESSE werden mehr und mehr durch Robotergreifer automatisiert, um Kosten zu sparen, die Qualität der Produkte zu erhöhen und größere Mengen produzieren zu können. Für den Transport von kleinen und empfindlichen Objekten gibt es jedoch oft keine Greifer, die in der Lage sind, die Objekte ohne Beschädigung zu transportieren. Um solche Prozesse in Zukunft automatisieren zu können, werden in dieser Arbeit berührungslose Greifer entwickelt, die mittels Ultraschallwellen Objekte berührungslos aufnehmen, transportieren und auf einem Ziel positionieren können.

Mit Hilfe von akustischen Schwebekräften lassen sich kleine Objekte und Flüssigkeitstropfen berührungslos und ohne Verschmutzung manipulieren. Um Robotergreifer zu entwickeln, welche Objekte akustisch schwebend transportieren, müssen die Objekte automatisch in das akustische Druckfeld gebracht werden. In dieser Arbeit werden analytische Modelle vorgestellt, auf deren Grundlage Konzepte für das kontrollierte Einsetzen von Objekten entwickelt werden. Drei Arten von akustischen Greifern werden implementiert und zur experimentellen Verifizierung des akustischen Aufhebens von Objekten verwendet. Das Aufheben von Objekten hoher Dichte ($\rho \leq 7.3 \text{ g/cm}^3$) von akustisch transparenten Oberflächen wird mit einem doppelseitigen Robotergreifer und stehenden Wellen mit dynamischer Anpassung der Schalleistung demonstriert. Ein einseitiger Greifer mit einer Kombination verschiedener akustischer Fallen wird verwendet, um Objekte geringerer Dichte ($\rho \leq 0.1 \text{ g/cm}^3$) von akustisch reflektierenden Oberflächen aufzuheben. Eine dritte in dieser Arbeit vorgestellte Methode verwendet einen Greifer mit einem dünnen und beweglichen Reflektor und stehenden akustischen Wellen, um Objekte mit hoher Dichte ($\rho \leq 7.3 \text{ g/cm}^3$) von akustisch reflektierenden Oberflächen aufzuheben.

Eine neuartige Methode zur Stabilisierung von im Greifer schwebenden Objekten während des Transports wird vorgestellt und mit aktuellen Stabilisierungsmethoden verglichen. Es werden neuartige Manipulationsmethoden untersucht, mit denen das schwebende Objekt auf einem Ziel abgelegt werden kann. Um eine hochpräzise Positions- und Orientierungsregelung zu erreichen, wird ein Regelsystem, welches mit Hilfe von Kameras die Position und Orientierung eines Objektes erkennen kann, entworfen.

Neben dem Transport von Festkörpern können Ultraschallkräfte auch für den Transport von Flüssigkeitstropfen genutzt werden. Dies

kann für den kontaminationsfreien Transport von Substanzen genutzt werden, bei denen der physische Kontakt mit Spritzen oder Pipetten zu chemischen Reaktionen führen würde. Im Rahmen dieser Arbeit wird ein Greifer entwickelt, der in der Lage ist, Flüssigkeitstropfen im Mikroliterbereich zu transportieren. Er nutzt Ultraschallimpulse, um Tropfen aus einem Flüssigkeitsbehälter auszuwerfen, und ein neuartiges akustisches Schwebegerät, welches die ausgeworfenen Tropfen auffangen kann. Dieses Gerät ist der erste luftgekoppelte akustische Tropfenauswerfer, mit welchem das Einbringen von Flüssigkeitstropfen in ein akustisches Schwebefeld ermöglicht wird.

Die erzielten Ergebnisse eröffnen neue Möglichkeiten für die Implementierung von akustischen Schwebemethoden in Robotergreifern, welche das Potenzial haben, in einer Vielzahl von industriellen Anwendungen eingesetzt zu werden.

Abbreviations

ADE	Acoustic Droplet Ejection
ARIS	Akademische Raumfahrt Initiative Schweiz
BA	Bachelorarbeit
BVD	Butterworth - Van Dyke
CMOS	Complementary Metal-Oxide Semiconductor
CV	Coefficient of Variation
DMAP	Distribution of the Maximum Attainable Pressure
EPS	Expanded Polystyrene
ESA	European Space Agency
EuRoC	European Rocketry Challenge
FOV	Field of View
FPGA	Field Programmable Gate Array
FPS	Frames Per Second
HTT	Horizontal Twin Trap
IMU	Inertial Measurement Unit
IC	Integrated Circuit
LED	Light-Emitting Diode
LiDAR	Light Detection and Ranging
MA	Masterarbeit
MF	Multi-Frequency
MOSFET	Metal-Oxide-Semiconductor Field-Effect Transistor
NASA	National Aeronautics and Space Administration
ODE	Ordinary Differential Equation
OpenCV	Open Source Computer Vision
PC	Personal Computer
PCT	Piezoelectric Ceramic Transducer
PLA	Polylactic Acid
PSD	Position Sensitive Device
RMS	Root Mean Square
RPM	Revolutions Per Minute
SA	Semesterarbeit
SIT	Switching-In-Time
StoM	Studies on Mechatronics
UART	Universal Asynchronous Receiver / Transmitter
USB	Universal Serial Bus
VTT	Vertical Twin Trap

Contents

Acknowledgments	iii
Abstract	v
Kurzfassung	vii
Abbreviations	ix
1 Introduction	1
1.1 Applications of Acoustic Levitation	2
1.2 Development of Acoustic Levitation Technology	2
1.3 Manipulation of Acoustically Levitating Objects	4
1.4 Robotic Grippers for Solid Objects	5
1.5 Robotic Grippers for Liquid Handling	6
1.6 Piezoelectric Transducers	7
1.7 Signal Generation and Power Electronics	10
1.8 Aims and Contributions	11
1.9 List of Publications	13
1.10 Supervised Student Theses	15
1.11 Thesis Outline	15
2 Acoustic Levitation	19
2.1 Introduction	19
2.2 Piezoelectric Transducers	20
2.3 Acoustic Pressure	23
2.4 Acoustic Radiation Force and Torque	23
2.5 Multi-Frequency Acoustic Levitation	25
2.6 Traps	26
2.7 Power Electronics and Control	27
3 Manipulation of Acoustically Levitating Objects	29
3.1 Introduction	29
3.2 Position Control	30
3.3 Stabilization of Asymmetric Objects	32
3.4 Closed-Loop Control	39
3.5 Acoustic Catching	57
3.6 High-Bandwidth Manipulation	67

4	Solid Gripper	83
4.1	Introduction	83
4.2	Environment	84
4.3	Acoustic Levitation in Reflective Environments	85
4.4	Distribution of the Maximum Attainable Pressure	87
4.5	Grippers	87
4.6	Transport with the Single-Sided Gripper	88
4.7	Transport with the Reflector Gripper	91
4.8	Orientation Control with the Reflector Gripper	95
5	Liquid Gripper	103
5.1	Introduction	103
5.2	Acoustic Droplet Ejection	105
5.3	Droplet Levitation	109
5.4	Droplet Catching	111
6	Outlook	117
6.1	Solid Grippers	117
6.2	Liquid Grippers	119
	Appendices	121
A	Measurements of Acoustic Pressure Fields using Schlieren Photography	123
A.1	Introduction	123
A.2	Schlieren Photography	123
B	Stability Evaluation for an Acoustic Levitator During a Rocket Launch	129
B.1	Introduction	129
B.2	Rocket Launch	129
	Bibliography	133
	Curriculum Vitae	151

1

Introduction

THE automation of manufacturing processes is advancing rapidly in a number of industries. In micro-manufacturing processes, however, many tasks are still performed manually, as robotic grippers are reaching their limits. Some grippers are not sensitive enough to handle fragile components and would therefore damage the components during the transport. Other grippers with the required sensitivity are not capable of picking up small objects.

These challenges are currently addressed through the development of soft robotic grippers [1–3], which adjust their shape to the shape of the object to be gripped and inflatable grippers based on the controllable adhesion mechanism of micro-fiber adhesives [4], which grip objects using micro structures inspired by geckos. However, these grippers are mainly used for larger objects such as food and plants and are not suitable for very small objects < 1 cm. Additionally, these grippers are still based on mechanical contact and can therefore contaminate or damage the objects.

In order to develop a robot gripper for the automation of processes containing small objects in the size range < 1 cm, which reduces the stress acting on the objects to be transported and prevents contamination, grippers using acoustic radiation forces to levitate the object to be transported are investigated during this work. This involves an investigation of the picking process for objects located in different environments without mechanical contact, the stabilization during transport, and the placement on a target in a controlled, gentle and contamination-free manner.

Transportation processes for liquid droplets are more and more carried out in an automated manner as well. Currently used methods and

devices for the automated transport of liquid droplets reduced the time consumption of processes in the medical chemistry and biochemistry industries significantly. However, the methods require mechanical contact using a pipette, a nozzle, or a pin, which causes chemical reactions and contamination of the liquid [5]. Acoustic droplet ejection (ADE) is a contact-less method for the transport of liquid droplets from a liquid pool to a target substrate. Despite solving the aforementioned issues with other automation devices, the methods used for ADE are complex, the devices are expensive, and the catching process carried out by the target substrate requires mechanical contact with the liquid.

During this work, an acoustic levitation device capable of ejecting and catching liquid droplets without mechanical contact was developed. The liquid does not get in contact with any material during the transport, which prevents contamination and chemical reactions. The device can be used to study a levitating liquid droplet (e.g. using spectroscopy), or to transport liquid droplets using the device as an ultrasonic liquid gripper.

1.1 Applications of Acoustic Levitation

Acoustic levitation systems are currently used in various fields such as chemical analysis [6], study of living animals in microgravity [7, 8], research of biomaterials [9], spectroscopy [10–12] and control of nanomaterial self-assembly [13]. Squeeze film levitation methods can be used for the contact-less transport of small and large objects with flat or curved surfaces, where the shape of the gripper has to be adjusted to the shape of each object [14–17]. Of particular interest for the development of acoustic robot grippers are the applications in the field of containerless processing [18–20] and the studies of physical properties and dynamics of levitating liquid droplets [21–24].

1.2 Development of Acoustic Levitation Technology

Until recently, acoustic levitation was mainly achieved using standing waves. Visualizing standing waves was already possible over 200 years ago. Ernst Chladini has observed that powder located on top of vibrating

plates and membranes concentrates along lines during excitation at resonance. These lines are referred to as nodal lines [25].

About 100 years later, August Kundt developed an experiment that can visualize standing waves in gases such as air. Kundt's tube uses a sound source at one end of the tube and a movable piston at the other end to adjust the length of the tube. The sound source is operated at a constant frequency and the piston is then moved until the sound becomes significantly louder. This is the case when the distance between the source and the piston is a multiple of half the wavelength and thus a standing wave is formed. Fine powder, which is previously placed in the tube, collects at the nodes of the standing wave. This apparatus can also be used to measure the speed of sound in various gases [26].

In 1933, the first device enabling acoustic levitation using standing waves was built. Bücks and Müller formed a standing wave between an oscillating quartz and a reflector and were able to levitate alcohol droplets at the pressure nodes of the standing wave [27, 28].

In the years that followed, various devices were developed which levitate objects using single-axis standing waves. They consist of a transducer and a reflector [29–33], two opposing transducers [34], or two opposing arrays of transducers [35, 36]. The devices using a transducer and a reflector are limited to separating distances of a multiple of half the wavelength in order to achieve resonance. For two opposing transducers or arrays of transducers the separating distance can be chosen arbitrarily.

Another method to achieve acoustic levitation with standing waves are resonance chambers [37–39]. Three orthogonally aligned loudspeakers are used to generate three standing waves. The superposition of these standing waves results in a pressure field in which the position of the object can be controlled using acoustic radiation forces [40].

This technology was developed for NASA [31, 33, 41–44] and ESA [45] to enable contact-less positioning in microgravity environments. The devices were later modified to be used and commercialized on earth [45–47].

Using standing wave devices, the levitation of coins [48, 49], liquid drops [40, 50], lead shots [51], living animals [7, 8], liquid mercury [52] and iridium [52] was demonstrated.

Heavier and larger objects can be levitated using near-field or squeeze film acoustic levitation. Thereby the levitating object acts as a reflector. With this method, planar objects can levitate tens to hundreds of micrometers above the transducers. For small levitation heights, objects

with a mass of up to a few kilograms can be levitated [14, 28, 53–57]. Near-field acoustic levitation can also be used to levitate spheres [58] and objects of cylindrical shape [59].

Furthermore, it is possible to levitate objects in the far field while using the levitating object as a reflector. A standing wave is thereby formed between one or more transducers and the surface of the levitating object. Usually, a distance of $\lambda/2$ is used, due to the maximum radiation force at this distance. The forces that can be achieved are relatively large and objects that are significantly larger than the wavelength [60, 61] can be levitated, which was demonstrated for the first time in 1975 [31]. The radial stability of devices using a single transducer are low and, thus, mechanical contact is sometimes required to ensure stability [60]. Using a tripod arrangement of three transducers can solve this issue for certain object shapes as demonstrated for an expanded polystyrene sphere with a diameter of 50 mm in [61].

For all aforementioned methods, two opposing elements are required. Recently, a method capable of levitating objects using a single-sided emitter [62] was presented. This method is referred to as single-beam levitation.

1.3 Manipulation of Acoustically Levitating Objects

Acoustic forces can not only be used to levitate objects, but also to manipulate the position and orientation of the objects. In robotic grippers, the manipulation of orientation is important to place objects in the desired orientation on a target. Manipulation of the position can be used to compensate for inaccuracies in the positioning of the gripper by the robot arm, thereby achieving high precision.

The position of an object levitating in a standing wave, which is generated by a transducer and a reflector, can be adjusted by moving the reflector while simultaneously adjusting the excitation frequency in such a way that the reflector is always separated from the transducer by a multiple of half the wavelength [63]. For a fixed separating distance between transducer and reflector, it is possible to adjust the frequency stepwise in such a way that separating distance always corresponds to a multiple of half the wavelength. This allows a movement of the object in discrete steps [37].

When two opposing transducers are used to generate the standing wave, adjusting the phase shift between the two transducers can move the nodes of the standing wave and therefore adjust the position of the levitating object [34, 64–67].

To be able to manipulate the position of the levitating object in three dimensions without moving the transducer or reflector, two opposing arrays of transducers can be used. By adjusting the phases of the transducers, the standing wave can be moved arbitrarily in the space between the two arrays.

The previous methods are all used to manipulate the position. To manipulate the orientation of objects levitating in orthogonal standing waves in a resonance chamber, acoustic viscous torques can be used [50, 68]. This method can also be used to rotate levitating liquid droplets [50].

Position manipulation and rotation of objects levitating in single-beam levitators were examined in 2015 using arrays of transducers [62]. This was possible by individually controlling the phase of the transducers and using pressure distributions referred to as twin traps.

The rotation of acoustically levitating objects was further investigated in 2017 by using orbital angular momentum transfer in acoustic vortex fields [69] achieving rotational speeds up to 15 krpm. In 2022 orbital angular momentum was used to achieve rotational speeds up to 390 krpm [70].

Manipulation of the position and orientation in six degrees of freedom was achieved in 2020, using an array of 444 transducers to generate an asymmetric pressure field [71].

Recently, methods that minimize a cost function designed to describe trapping forces were used to levitate objects larger than the acoustic wavelength using a flat array of transducers [72, 73].

1.4 Robotic Grippers for Solid Objects

Automation of the transport processes of sensitive objects develops towards soft gripping or contact-less gripping technology. Until recently, acoustic forces were mainly used with near-field levitators to transport objects without mechanical contact. However, near-field levitation can only be used for planar or slightly curved objects, which limits the applications of this method.

The use of far-field acoustic levitators as robot grippers has been studied sparsely. The manipulation of objects which are levitating in acoustic levitators has been intensively studied. However, the objects were mostly put into the pressure field in a contact-based manner. The contact-less gripping process for objects located on acoustically reflective surfaces was only studied for light objects with a density $\rho < 0.1 \text{ g/cm}^3$ [74, 75].

During the transport with acoustic grippers, standing waves are the preferred type of pressure fields, due to their high radiation forces. Thus, objects with high density can be transported. However, this causes the levitating objects to have a tendency to spin around the symmetry axis of the pressure field [76, 77]. This is not only a problem for robot grippers and has accordingly been studied several times. It has been shown that the spin can be stopped by time multiplexing two acoustic traps [78]. Rapid switching back and forth between two acoustic traps results in a loss of acoustic power due to the inertia of the transducer and causes an audible tone at the switching frequency. Furthermore, by generating two perpendicular standing waves of different strengths, an asymmetric pressure field can be generated, which can also stop the spin [71]. However, this has only been demonstrated for light objects ($\rho < 0.1 \text{ g/cm}^3$).

The depositing process is usually accomplished in the same way as the picking process, as long as the environments are similar. The orientation of asymmetric objects can be controlled during the depositing process.

1.5 Robotic Grippers for Liquid Handling

A major advantage of acoustic levitation over other levitation methods is its independence from physical properties of the material to be levitated. With acoustic forces it is also possible to levitate liquid droplets. Thus, if it is possible to insert a droplet into an acoustic levitation system without mechanical contact, levitate the droplet stably, and deposit it on a target, a contact-less and contamination-free transport of liquids with an acoustic gripper would be possible.

Already in 1933, it was shown that alcohol droplets can be levitated in standing waves [27]. The droplets were introduced manually into the nodes of the standing wave using a pipette or a syringe. To achieve the contact-less insertion of liquid droplets into an acoustic levitation

system, a method is needed which can separate a liquid droplet from a larger quantity of the liquid in a contact-less manner and insert it into the acoustic field.

A method for the contact-less ejection of droplets using acoustic forces, referred to as acoustic droplet ejection (ADE), is already used for commercial applications. It uses a piezoelectric transducer that is coupled via a liquid interface to the liquid container. The transducer emits ultrasonic waves through the liquid interface, the container and the liquid such that they are focussed on the surface of the liquid. Droplets in the nano and pico litre range can be ejected using this method. The droplets are caught using a target substrate on top of the liquid container. However, this method requires a target substrate that can collect the droplets upside down and in a contact-based manner. Furthermore, the high complexity of the liquid coupling results in high costs and large volume [5].

Additionally, there are contact-based ejection methods, which allow the ejection of liquid droplets. By dropping a solid object into a liquid source, an air cavity is created which subsequently collapses. Under certain conditions Worthington jets are formed, which can eject a droplet from the liquid pool. This was investigated in detail in [79, 80]. This ejection method was adjusted during this work by generating the air cavity using an ultrasonic pulse, allowing contact-less ejection of droplets in a controlled manner.

This droplet is then to be caught by a droplet levitator. Due to the vertical ejection of the droplet, no transducers can be placed below the droplet during the ejection and catching process. Since this would be necessary for levitation systems that use standing waves, a droplet catcher that is capable of levitating liquid droplets by means of laterally arranged transducers has to be developed for contact-less ultrasonic liquid grippers.

1.6 Piezoelectric Transducers

There are two basic types of piezoelectric transducers that are used for acoustic levitation systems. Large high-power transducers with an acoustic horn were the only option for a long time, until it was discovered that small lower-power transducers, which were initially developed for parking sensors, can be used in arrays for acoustic levitation [62].

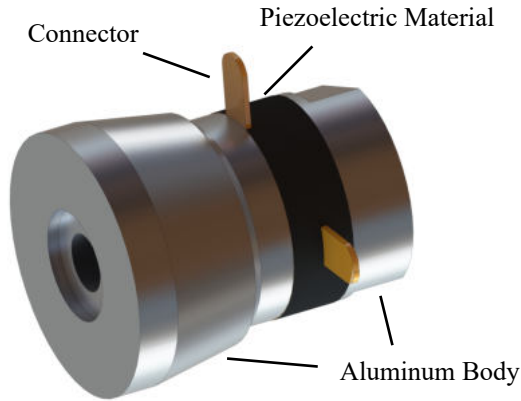


Fig. 1.1: Structure of a piezoceramic sandwich transducer.

High-power transducers consist usually of a piezoceramic sandwich structure, as shown in Fig. 1.1, due to their small dimensions and good efficiency [81].

A piezoceramic element extends and contracts due to the piezoelectric effect. Piezoelectric ceramic transducers (PCTs) are generally fabricated in circular plates or rings [82]. An impedance measurement of a PCT with a resonance frequency of about 41 kHz is shown in Fig. 1.2. The impedance of such a transducer can be approximated using a Butterworth-Van Dyke equivalent circuit.

Due to the impedance mismatch between the transducer and air, an ultrasonic horn and a radiator are required to generate high amplitude pressure waves [81]. Ultrasonic horns, also known as concentrators or sonotrodes, consist of a metal rod with constant or variable cross section, which extends and contracts according to the excitation frequency. Its purpose is the amplification of the vibration amplitude, which is achieved with different horn shapes such as stepped, tapered or exponential horns as shown in Fig. 1.3.

Due to the varying cross sectional area of all horn shapes, the vibration amplitude in the slimmer part is increased. The resonance frequency of the horn needs to approximately match the resonance

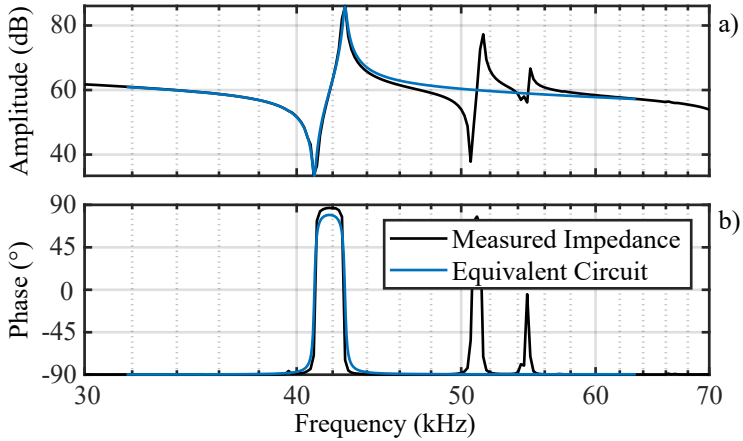


Fig. 1.2: Impedance measurement of a high power transducer and the BVD Model equivalent circuit (see Fig. 2.1).

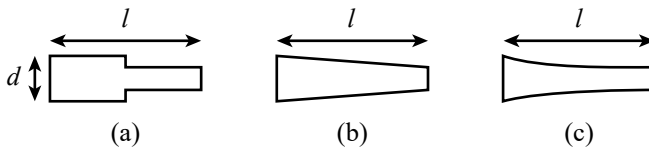


Fig. 1.3: Commonly used horn shapes for high-power piezoelectric transducers: (a) stepped horn, (b) tapered horn, and (c) exponential horn.

frequency of the PCT in order to increase the output vibration amplitude. The longitudinal length l of the acoustic horn needs to be a multiple of half the wavelength to maximize the displacement. The ultrasonic horn should not have a diameter d larger than a quarter of the wavelength to suppress unwanted modal coupling [82]. Ultrasonic horns are produced out of high durability and high mechanical strength materials, such as stainless steel, duraluminium or titanium [83]. A radiator, which is typically a round metal plate, is mounted to the tip of the horn in order to increase the cross-sectional area and match the impedance between the transducer and air.

The second type of transducers are low-power transducers that generate pressure waves with significantly smaller amplitudes and therefore have to be operated in an array. They consist of a piezoelectric element, a beamformer and two dampers. For the development of ultrasonic robt grippers, weight and size is very important. Thus, small low-power transducers are preferred, which additionally allows manipulations of the levitating object due to the operation in an array. This work therefore focuses on acoustic levitation systems using low-power transducers with a diameter of 10 mm or 16 mm.

1.7 Signal Generation and Power Electronics

For the systems consisting of a high-power transducer and a reflector or two high-power transducers, signal generators were mostly used for signal generation and operational amplifiers [84] or audio amplifiers [85] for signal amplification. This is no longer practical for larger arrays of transducers with individual phase and amplitude. Therefore, micro-controllers and FPGAs are used to generate the signals. For amplification, different amplifier ICs can be used depending on the number of transducers operating at the same phase. For systems with several transducers in phase, L298N dual H-bridge boards are mostly used. For individual control of the transducers, gate driver ICs (e.g. IX4428), MOSFET ICs (e.g. FDMQ8403) or pulse generator ICs (e.g. HV7355) can be used.

1.8 Aims and Contributions

The objective of this work is to investigate acoustic levitation in terms of its usability for the development of contact-less robot grippers. Thereby, methods are developed which allow the transport of small and fragile objects and liquid droplets in a compact, cost-effective, contact-less and contamination-free manner.

1.8.1 Picking Process

For this purpose, the most challenging part of the transport, i.e. the picking process, is investigated for objects located in different environments and for different object densities. The picking of objects with low density ($\rho < 0.1 \text{ g/cm}^3$) can be carried out by a single-sided gripper for objects located on acoustically reflective and transparent surfaces. High density objects are more challenging to pick up and therefore require different grippers for reflective or transparent environments. A double-sided gripper is used to demonstrate contact-less picking of objects with a density of up to $\rho = 7.3 \text{ g/cm}^3$ located on an acoustically transparent surface. A gripper with a movable reflector is developed to pick up objects with a density of up to $\rho = 7.3 \text{ g/cm}^3$ located on an acoustically reflective surfaces.

1.8.2 Stabilization and Manipulation in an Acoustic Gripper

During the transport in an ultrasonic gripper that uses standing waves, which is the case for the reflector gripper or the double-sided gripper, the objects start to spin around the symmetry axis due to the symmetry of the pressure field. This work presents a method to stop this spin, which requires a lower number of controlled channels and no rapid phase adjustments, resulting in reduced complexity and increased stability compared to state-of-the-art methods.

Manipulation of objects levitating in the acoustic gripper can be used to precisely position an object on a target. Methods are developed that can manipulate the position and orientation of objects. The previously mentioned stabilization method, that uses two different types of transducers operating at different frequencies, is extended to also manipulate the orientation around the symmetry axis. The forces acting on objects in this gripper are calculated by deriving an approximation for

the acoustic forces acting on small objects in multi-frequency pressure fields.

Furthermore, a method for controlling the rotations around the horizontal axes is developed using tilts of the standing wave achieved by controlling the phase and amplitude of the excitation signals. Combining these methods facilitates manipulation of the levitating object in six degrees of freedom.

1.8.3 Closed-Loop Control

Micro-manufacturing processes often require very high precision. If ultrasonic robotic grippers are to be used for the automation of such processes, they must be able to reliably achieve the required accuracy. Unfortunately, the propagation of sound waves is highly dependent on the environment. Slight changes in temperature and humidity can cause the levitation position or orientation of the levitating object to change significantly enough to no longer meet the requirements. Furthermore, simplifications are often made when calculating the forces and torques acting on the object, and in some cases even the object geometry and material properties are not taken into account. The resulting inaccuracies are compensated by a closed-loop system using two CMOS cameras to detect the position and the orientation of the object. High precision control is achieved with the closed-loop system despite inaccurate open-loop algorithms.

1.8.4 Acoustic Catching

As an alternative for the previously mentioned methods for inserting objects into the acoustic field, it is also possible to drop objects and subsequently decelerate and catch them acoustically. For this purpose, a demonstrator is developed, which can acoustically catch expanded polystyrene objects. The controllers developed in the process can be used in the future to acoustically catch liquid droplets.

1.8.5 High Bandwidth Manipulation

For several applications of acoustic levitation, rapidly changing transducer phases are required. The behaviour of the transducers, which are commonly used in transducer arrays, is investigated for this mode of

operation using a ring shaped arrangement of piezoelectric transducers. The arrangement rotates a levitating object with high rotational speeds. The control of the transducers requires two phase shifts of 180° during each revolution and therefore results in rapidly changing phases. The device is capable of achieving rotational speeds up to 216 krpm, which was the highest rotational speed achieved using acoustic levitation devices up to the time of publication. Simulations and measurements have shown, that the commonly used equivalent circuit of piezoelectric transducers (BVD model [86]) has to be extended for such application in such a way that resonances at higher frequencies are considered as well. This is relevant for the levitation of objects larger than the acoustic wavelength [87], the stabilization of asymmetric objects levitating in standing waves [78] and for ultrasonic haptic devices [88].

1.8.6 Liquid Gripper

The currently used droplet ejection methods either are contact-based or eject droplets in the nano or pico litre range, which can not be caught acoustically. A new method using air-coupled transducers that generate ultrasonic pulses focused on the surface of the liquid is presented in this work. The pulse forms an air cavity inside the liquid, which collapses and ejects a Worthington jet. At the tip of the jet, a droplet can be formed and ejected up to a height of a few centimetres. The ejected droplet is in the micro litre range and can be caught by a ring shaped acoustic catcher developed in this work. An improved mounting method for the transducers is presented, which is required for stable levitation of the liquid droplet with such an arrangement. Furthermore, the droplet volume and the ejection height can be controlled by adjusting the pulse length and the excitation voltage of the transducers.

1.9 List of Publications

Key insights presented in this thesis have already been published in international scientific journals, conference proceedings, or in patents. The publications created as part of this thesis are listed below.

1.9.1 Journal Papers

- ▶ M. Röthlisberger, M. Schuck, and J. W. Kolar, “Kilohertz-Frequency Rotation of Acoustically Levitated Particles,” *IEEE Transactions on Ultrasonics, Ferroelectrics, and Frequency Control*, 2022. DOI: [10.1109/TUFFC.2022.3149131](https://doi.org/10.1109/TUFFC.2022.3149131), [PDF].
- ▶ M. Röthlisberger, G. Schmidli, M. Schuck, and J. W. Kolar, “Multi-Frequency Acoustic Levitation and Trapping of Particles in All Degrees of Freedom,” *IEEE Transactions on Ultrasonics, Ferroelectrics, and Frequency Control*, 2022. DOI: [10.1109/TUFFC.2022.3149302](https://doi.org/10.1109/TUFFC.2022.3149302), [PDF].
- ▶ M. Röthlisberger, M. Schuck, L. Kulmer, and J. W. Kolar, “Contactless Picking of Objects Using an Acoustic Gripper,” *Actuators, Selected Papers from the 1st International Electronic Conference on Actuator Technology: Materials, Devices and Applications (IeCAT)*, 2021. DOI: [10.3390/act10040070](https://doi.org/10.3390/act10040070), [PDF].

1.9.2 Conference Papers

- ▶ M. Röthlisberger, M. Schuck, L. Kulmer, and J. W. Kolar, “Automated Insertion of Objects Into an Acoustic Robotic Gripper,” *Proc. of the 1st International Electronic Conference on Actuator Technology: Materials, Devices and Applications*, online, November 2020. DOI: [10.1109/JESTPE.2016.2617620](https://doi.org/10.1109/JESTPE.2016.2617620), [PDF].
- ▶ M. Röthlisberger, M. Schuck, and J. W. Kolar, “Contactless Positioning of Objects on Acoustically Reflective Surfaces by Means of Ultrasonic Forces,” *Proc. of International Ultrasonics Symposium*, Venice, Italy, October 2022. DOI: not available, [PDF].

1.9.3 Further Scientific Contributions

- ▶ M. Alexander-Schuck and M. Röthlisberger, “Method for Handling an Object in a Pressure Amplitude Distribution,” *Patent*, WO2022058281A1 DOI: not available, [PDF].
- ▶ M. Alexander-Schuck and M. Röthlisberger, “Contactless Manipulation of Objects Using Controlled Electroacoustic Transducers,” *Patent*, WO2022002825A1 DOI: not available, [PDF].

1.10 Supervised Student Theses

- ▶ C. Burkard, “Closed-Loop Control of an Acoustic Levitation System,” MA, 2019.
- ▶ L. Kulmer, “Real-Time Calculation of Acoustic Pressure Fields and Forces in Obstructed Environments,” SA, 2020.
- ▶ N. Stephan, “Novel Acoustic Droplet Ejector for Contactless Laboratory Automation,” BA, 2021.
- ▶ E. Bürgisser, and D. Grandjean, “Development of a Schlieren Photography System for the Visualization of Acoustic Pressure Fields,” SA, 2021.
- ▶ G. Schmidli, “Passive Stabilization of Acoustically Levitated Objects Using Ultrasonic Waves of Multiple Frequencies,” BA, 2021.
- ▶ E. Frei, “Horn Design for a Hovercraft Based on Near-Field Acoustic Repelling Forces,” StoM, 2021.
- ▶ S. Gasser, “Power Electronics for a Hovercraft Based on Near-Field Acoustic Repelling Forces,” StoM, 2021.
- ▶ E. Frei, and S. Gasser, “Hovercraft Based on Near-Field Acoustic Repelling Forces,” BA, 2021.
- ▶ P. Wolff, “High Bandwidth Control of Acoustic Levitation Systems,” BA, 2021.
- ▶ D. Bolliger, “Six Degree-of-Freedom Closed-Loop Control of Acoustic Levitation Systems,” SA, 2021.
- ▶ N. Behr, “Development of the First Acoustic Catcher,” BA, 2021.
- ▶ T. Wilhelm, “Development of an Ultrasonic Gripper for Micro-Manufacturing Processes,” BA, 2022.

1.11 Thesis Outline

According to the goals and contributions mentioned above, the content of the thesis is divided into five main chapters and conclusions. All the chapters can be read independently since the interdependencies have been reduced to the strict minimum.

- ▶ **Chapter 2** covers all theoretical basics which are required for an acoustic levitation system. Properties of the piezoelectric transducers are investigated and a suitable electrical equivalent circuit is developed. The achievable pressure, its standard deviation and the standard deviation of the phase of the transducers are compared with similar transducer models. It is shown for various applications how the electrical signals can be generated and with which components they are best amplified. Furthermore, it is shown how the pressure of each transducer and of an entire array of transducers can be calculated if the position and orientation of the transducers and the amplitude and phase of the excitation signals are known. It is shown how the acoustic forces can be calculated based on the pressure field and how the Gor'kov potential can be used as an approximation of the acoustic forces for small spherical objects. Different acoustic traps are presented, which can be used for acoustic levitation. In addition, a novel method for the calculation of multi-frequency pressure fields and the resulting Gor'kov potential is presented.
- ▶ **Chapter 3** describes different methods to manipulate objects levitating in an acoustic levitation system. It is shown how the levitation position can be controlled. A method, which stabilizes asymmetric objects levitating in standing waves through transducers operating at a different frequency is presented and compared to state-of-the-art stabilization methods. Furthermore, an open-loop five degrees of freedom manipulation algorithm is presented and extended with a closed-loop control system based on cameras and image processing algorithms. It is used to control a spheroid shape object in five degrees of freedom and compares the performance to the open-loop system. Additionally, a prototype capable of catching objects travelling through its acoustic field using two different methods is shown. The behaviour of the transducers for fast phase changes is examined with a demonstrator capable of rotating an acoustically levitating object with a rotational speed of more than 200 krpm.
- ▶ **Chapter 4** presents acoustic robot grippers capable of transporting small and fragile objects to and from acoustically transparent and reflective surfaces. A method for the calculation of pressure fields in reflective environments is shown. A single-sided robot grip-

per that is capable of transporting objects to and from transparent surfaces is presented. For this gripper, a method is developed, which allows the picking of light objects from acoustically reflective surfaces. Another gripper using an additional moveable reflector is demonstrated. It is capable of transporting heavy objects to and from acoustically reflective surfaces and is able to control the orientation of the object to be transported.

- **Chapter 5** presents a novel contact-less droplet ejection method, using air coupled transducers to generate an air cavity in a liquid container. During the collapse of the air cavity a Worthington jet is formed and a droplet is ejected at the tip of the jet. The method is compared to state-of-the-art droplet ejection methods. Furthermore, an improved transducer mounting method, which embeds the transducers into the holder in order to prevent vibrations of the transducers is presented. This allows stable levitation at higher operating voltages. Due to the increased forces at high voltages, levitation of liquid droplets in horizontal twin traps using a ring shaped array is achieved. This allows the development of an acoustic liquid gripper by using this levitator to catch the droplet ejected by the aforementioned droplet ejector.

2

Acoustic Levitation

Chapter Abstract

Ultrasonic robot grippers use acoustic radiation forces to transport objects in a contact-less and contamination-free manner. They generate ultrasonic waves resulting in a pressure field that causes acoustic radiation forces acting on a levitating object. This chapter examines the acoustic sources, i.e. piezoelectric transducers, used to generate the ultrasonic waves, provides methods for the calculation of the pressure field and an approximation for the calculation of a force potential. Furthermore, a method for the calculation of pressure fields generated by ultrasonic transducers operating at different frequencies is presented and an approximation for the multi-frequency force potential is derived. Additionally, different ways of excitation signal generation and amplification are examined.

2.1 Introduction

Acoustic forces were first observed and visualized over 200 years ago [25]. Forces resulting from standing acoustic waves were used to make alcohol droplets levitate nearly 100 years ago [27]. In recent years there has been a development from large high-power transducers to small low-power transducers operated in an array [62]. Since the small transducers were developed for parking sensors in cars, their relevant properties for acoustic levitation systems have not yet been examined in detail.

These properties, a comparison between different models of the low-power transducers, and methods for the calculation of pressure fields generated by piezoelectric transducers are presented in this chapter. Furthermore, methods for the calculation of the acoustic radiation force,

the acoustic radiation torque and an approximation of the force potential for small objects are provided. Different ways of signal generation and amplification and their best suited application are presented.

2.2 Piezoelectric Transducers

The pressure fields required for acoustic levitation are generated by a single or multiple piezoelectric transducers. They generate sound waves in the ultrasonic range. For most applications in this work, an array of piezoelectric transducers is required. By superimposing the sound waves of all transducers it is possible to generate pressure fields that allow stable levitation.

There are different types of piezoelectric transducers. Large high-power transducers were used for most standing-wave levitators before small low-power transducers were used in an array to levitate objects acoustically [62]. For robot grippers, the size and weight of the transducers and the achievable pressure amplitude are particularly relevant. Therefore, the small low-power transducers consisting of a piezoelectric element, two dampers, two electrodes and a beamformer, as shown in Fig. 2.1, are best suited.

Different models of small transducers with a diameter of 10 mm and 16 mm and a resonance frequency of 40 kHz can be used for acoustic levitators. Commonly used models are compared in Tab. 2.1 [35].

To maximize the pressure and the trapping forces in a gripper, the pressure of a single transducer per transducer area is relevant. The transducers with a diameter of 16 mm have a cross-sectional area that is 2.56 times larger than that of the transducers with a diameter of 10 mm. This means that 2.56 times more 10 mm transducers can be placed on the same gripper area. Therefore, the highest pressure can be generated by using the MA40S4S model. However, the prices of the models vary significantly. Therefore, using the MSO-P1040H07T model can be considered, since it achieves large pressure amplitudes and is significantly cheaper than the MA40S4S.

Fig. 2.2 shows an impedance measurement of the MSO-P1040H07T transducers. Due to the narrow-band characteristics it is important to operate them close to their resonance frequency in order to generate pressure waves with large amplitudes. The impedance measurements show, that the transducers have more than one resonance frequency. The measurements were carried out in order to find out whether the

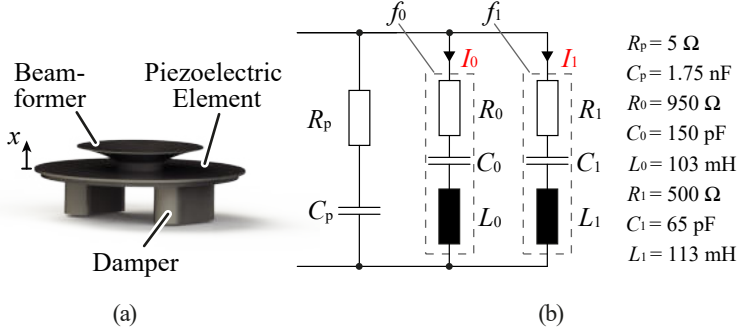


Fig. 2.1: (a) Elements of the employed ultrasonic transducers and (b) an extended Butterworth-Van-Dyke (BVD) equivalent circuit model with two resonances.

Tab. 2.1: Evaluation of different commercially available 40 kHz air transducers. The measurements were repeated for 10 items. The transducers were excited with a square-wave of $10 V_{pp}$ and measured with a wideband microphone ($1/8''$ Brüel & Kjær calibrated microphone Type 4138-A-015) [35].

Model	d (mm)	P (Pa·m/V)	$\sigma(P)$	$\sigma(\varphi)$ ($^\circ$)
MSO-P1640H10TR	16	0.25	0.04	8.7
MSO-A1640H10T	16	0.36	0.02	9.2
MSO-P1040H07T	10	0.13	0.02	13.9
FBULS1007P-T	10	0.14	0.02	13.9
MA40S4S	10	0.17	0.01	3.8
MCUST10P40B07RO	16	0.25	0.04	33.1
MCUSD16A40S12RO	16	0.21	0.03	18.3

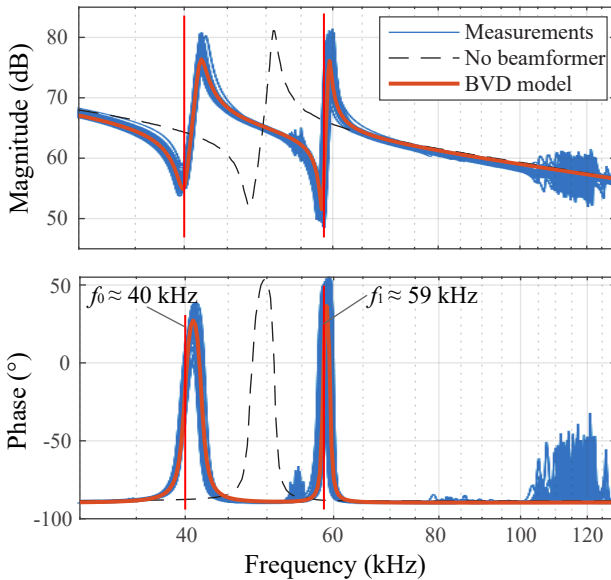


Fig. 2.2: Magnitude (top) and phase (bottom) of impedance measurements of 90 MSO-P1040H07T transducers compared to a fitted multi-resonance BVD model. The dashed lines show the measurement of the impedance of an MSO-P1040H07T transducer with removed beamformer [89].

impedance around the 40 kHz resonance is similar for different transducers of the same model. As shown in Fig. 2.2 the amplitude is very similar for all 90 measured transducers, but there is a slight deviation for the phase. This deviation could be measured and compensated for each transducer in order to increase the pressure amplitude [89, 90].

The beamformer is mounted on the piezoelectric element and is used to maximize the pressure amplitude for a radiation angle of 0° . It has a significant influence on the impedance of the transducer as shown by an impedance measurement without the beamformer in Fig. 2.2.

The piezoelectric transducers can be represented electrically by a Butterworth-Van Dyke (BVD) model [86]. It shows very similar behaviour for the first resonance frequency but ignores any further resonances of the transducer. For applications with excitation signals containing higher frequency components, an extended BVD model is

required as shown in Fig. 2.1b [89]. The impedance of the extended BVD model is shown in Fig. 2.2.

2.3 Acoustic Pressure

The acoustic pressure generated by a single transducer j is calculated as

$$p_j = e^{i\phi} P_0 J_0(kr \sin \theta) \frac{1}{d} e^{ikd}, \quad (2.1)$$

where ϕ , P_0 , J_0 , d , θ , r and $k = \omega/c_0$ denote the phase of the transducer excitation signal, a factor depending on the electrical power ($P_0 = 0.13V_{\text{ex}}$ [35]), the Bessel function of order zero, the distance of the considered point to the transducer, the beam angle, the radius of the transducer, and the wave number, respectively [62].

The incident acoustic pressure field P_{in} , which results from the superposition of multiple sound waves of the same frequency, can be calculated by the sum of the individual pressure values [62] as

$$P_{\text{in}} = \sum_j p_j \quad (2.2)$$

2.4 Acoustic Radiation Force and Torque

The acoustic radiation force acting on a compressible object is calculated as

$$F_{\text{rad}} = - \int_{S_0} \langle p_2 \rangle \mathbf{n} dS - \int_{S_0} \rho_0 \langle (\mathbf{n} \cdot \mathbf{v}_1) \mathbf{v}_1 \rangle dS, \quad (2.3)$$

where p_2 , \mathbf{v}_1 , ρ_0 , \mathbf{n} and S denote the second order effect of the scattered pressure field, the first-order perturbation of the particle velocity, the air density, the normal vector of the object surface and the object surface, respectively [91].

For spherical objects with a radius much smaller than the wavelength ($r \ll \lambda$), the acoustic radiation force can be approximated by the Gor'kov potential U_{rad} as

$$U_{\text{rad}} = \frac{4\pi}{3} r^3 \left(\frac{k_1 \langle P_{1,\text{in}}^2 \rangle}{2\rho_0 c_0^2} - \frac{3k_2 \rho_0 \langle V_{1,\text{in}}^2 \rangle}{4} \right), \quad (2.4)$$

where $k_1 = 1 - \frac{\rho_0 c_0^2}{\rho_p c_p^2}$, $k_2 = \frac{2\left(\frac{\rho_p}{\rho_0} - 1\right)}{2\frac{\rho_p}{\rho_0} + 1}$. ρ , c , $P_{1,\text{in}}$ and $V_{1,\text{in}}$ denote density, speed of sound, incident pressure field and incident velocity field, respectively. Subscripts 0 and p refer to properties of the fluid medium and particle, respectively [91]. The acoustic radiation force is calculated as

$$\mathbf{F}_{\text{rad}} = -\nabla U_{\text{rad}} \quad (2.5)$$

With the Gor'kov potential, a complex analytical solution for the acoustic radiation force can be derived using

$$V_{1,\text{in}} = \left| \nabla \left(\frac{P_{1,\text{in}}}{i\rho_0\omega} \right) \right| \quad (2.6)$$

and the identity

$$\langle \cos^2(\omega t) \rangle = \frac{1}{2} \quad (2.7)$$

resulting in

$$U_{\text{rad}} = K_1 (|P|^2) + K_2 (|P_x|^2 + |P_y|^2 + |P_z|^2) \quad (2.8)$$

$$K_1 = \frac{1}{4}V \left(\frac{1}{c_0^2\rho_0} - \frac{1}{c_p^2\rho_p} \right) \quad (2.9)$$

$$K_2 = \frac{3}{4}V \left(\frac{\rho_0 - \rho_p}{\omega^2\rho_0(\rho_0 + 2\rho_p)} \right) \quad (2.10)$$

with P , $P_{x,y,z}$, ω and V denoting the incident pressure amplitude, its spacial derivatives, the angular frequency and the particle volume, respectively [62,91].

The acoustic radiation torque acting on the levitating object was derived using the conservation of linear momentum and is calculated as

$$T_{\text{rad}} = \rho_0 \int_{S(R)} d\mathbf{S} \cdot \langle \mathbf{r} \times \mathbf{u} \rangle \quad (2.11)$$

where $S(R)$, \mathbf{r} and \mathbf{u} denote the particle surface, the position vector and the fluid velocity, respectively.

For asymmetric objects in acoustic traps the behaviour for small angular deflections can be approximated by a torsional spring. The torsional spring constant K_T can be calculated by exciting an oscillation

of the levitating object and measuring the oscillation frequency f_{osc} using

$$K_{\text{T}} = 2\pi f_{\text{osc}}^2 I \quad (2.12)$$

where I denotes the moment of inertia of the object, which can be calculated depending on the object geometry.

With the torsional spring constant, the acoustic radiation torque can be approximated by

$$T_{\text{rad}} = \alpha K_{\text{T}} \quad (2.13)$$

where α denotes the deflection angle [78, 92].

2.5 Multi-Frequency Acoustic Levitation

Previously presented methods can be used for the calculation of pressure fields, if the transducers are all operated with the same excitation frequency. The time-averaged squared pressure field resulting from the superposition of two pressure fields P_1 and P_2 , which are generated by transducers operating at frequencies f_1 and f_2 with $f_1 \neq f_2$, is calculated as

$$\langle (P_1 + P_2)^2 \rangle = \langle P_1^2 \rangle + \langle P_1 P_2 \rangle + \langle P_2^2 \rangle. \quad (2.14)$$

The pressure fields P_1 and P_2 evaluated at one point in space result in oscillations p_1 and p_2 with an oscillation frequency f_1 and f_2 respectively:

$$\begin{aligned} p_1 &= \sin(2\pi f_1 t), \\ p_2 &= \sin(2\pi f_2 t + \phi), \end{aligned} \quad (2.15)$$

where ϕ denotes an arbitrary phase shift. The time-averaged superposition of these oscillations is calculated as

$$\begin{aligned} \langle (p_1 + p_2)^2 \rangle &= \langle p_1^2 + 2p_1 p_2 + p_2^2 \rangle \\ &= \langle \sin^2(2\pi f_1 t) \rangle + \langle 2 \sin \phi \sin(2\pi f_1 t) \cos(2\pi f_2 t) \rangle \\ &\quad + \langle 2 \cos \phi \sin(2\pi f_1 t) \sin(2\pi f_2 t) \rangle \\ &\quad + \langle \sin^2 \phi \cos^2(2\pi f_2 t) \rangle + \langle \cos^2 \phi \sin^2(2\pi f_2 t) \rangle \\ &\quad + \langle 2 \sin \phi \cos(2\pi f_2 t) \cos \phi \sin(2\pi f_2 t) \rangle. \end{aligned} \quad (2.16)$$

Using $\langle \sin(t) \rangle = \langle \cos(t) \rangle = \langle \cos(t) \sin(t) \rangle = 0$, the time-averaged superposition simplifies to

$$\begin{aligned} \langle (p_1 + p_2)^2 \rangle &= \langle \sin^2(2\pi f_1 t) \rangle + \sin^2 \phi \langle \cos^2(2\pi f_2 t) \rangle + \cos^2 \phi \langle \sin^2(2\pi f_2 t) \rangle \\ &= \langle \sin^2(2\pi f_1 t) \rangle + (\sin^2 \phi + \cos^2 \phi) \langle \sin^2(2\pi f_2 t) \rangle \\ &= \langle \sin^2(2\pi f_1 t) \rangle + \langle \sin^2(2\pi f_2 t) \rangle \end{aligned} \quad (2.17)$$

and the time-averaged superposition of the pressure field is therefore the sum of the time-averaged individual pressure fields [36, 93]:

$$\langle (P_1 + P_2)^2 \rangle = \langle P_1^2 \rangle + \langle P_2^2 \rangle. \quad (2.18)$$

The same applies to the particle velocity field

$$\langle (V_1 + V_2)^2 \rangle = \langle V_1^2 \rangle + \langle V_2^2 \rangle. \quad (2.19)$$

Therefore, the Gor'kov potential of the superimposed pressure field is calculated as [36]

$$\begin{aligned} U_{\text{rad}} &= \frac{4\pi}{3} r^3 \left(\frac{k_1 (\langle P_{1,\text{in}}^2 \rangle + \langle P_{2,\text{in}}^2 \rangle)}{2\rho_0 c_0^2} - \frac{3k_2 \rho_0 (\langle V_{1,\text{in}}^2 \rangle + \langle V_{2,\text{in}}^2 \rangle)}{4} \right) \\ &= U_{\text{rad},1} + U_{\text{rad},2}. \end{aligned} \quad (2.20)$$

2.6 Traps

For a long time, standing waves were the only way to make objects levitate acoustically. They can be generated using a single transducer and a reflector, two opposing transducers, or two opposing arrays of transducers [28]. Using standing waves, high vertical forces can be achieved and correspondingly heavy objects can be levitated. As a result, standing waves are mostly used in robotic grippers for counteracting gravity. With the development of cheap and compact piezoelectric transducers, it became possible to operate the transducers in an array and thus generate different trap shapes [62].

Vortex traps achieve high radial stability due to their rotationally symmetrical pressure distribution. However, they can only be used for

the levitation of light objects and cause the objects to spin [62]. Vortex traps can also be used to levitate objects with a diameter larger than the wavelength. For this purpose, the helicity of the vortex trap has to be increased [87].

Bottle traps are optimized for high vertical forces and can therefore be used for the levitation of heavier objects. The radial stability is rotationally symmetrical but is significantly lower compared to vortex traps [62].

Twin traps are not rotationally symmetrical and can therefore be used to stabilize asymmetric objects or to stop the spin of a levitating object. It is also possible to manipulate the object by means of twin traps with high precision, since the object aligns with the twin trap when the twin trap is moved or rotated [62, 92]. This property makes the twin trap interesting for certain use cases in robotic grippers.

The pressure distribution of twin traps looks very similar to that of standing waves. The difference is that the transducers have to be opposite to each other to generate a standing wave and a twin trap can also be generated from a single side [62]. Usually, standing waves are used in such a way that the vertical forces are maximized to levitate heavy objects and twin traps are used in such a way that the horizontal forces are maximized for maximum stability.

Additionally, it is also possible to create pressure fields containing multiple traps, when a large number of transducers is used [94].

2.7 Power Electronics and Control

The requirements for the excitation signals vary depending on the application. In order to keep an object levitated without manipulating it, it is sufficient to generate a signal of the appropriate frequency (25 or 40 kHz). It does not require an adjustment of its phase or duty cycle. Signal generators or Arduino Nano micro-controllers can therefore be used for such applications.

If the object is to be manipulated, signals with adjustable phase are required such that the pressure field can be altered. Simple movements (e.g. position control in one direction in a standing wave formed by two opposing transducers or transducer arrays) can be achieved by changing the phase shift of two excitation signals. This can also be achieved using signal generators or Arduino Nano micro-controllers. For more complex manipulations (e.g. position manipulation in three dimensions

or orientation manipulation), multiple signals with specific phase shifts have to be generated accurately. Therefore, FPGAs are the best solution for the signal generation.

Additionally, it has to be possible to continuously increase and decrease the acoustic power of the transducers in order to execute certain processes (e.g. picking and deposition) in a smooth manner. This is achieved by reducing and increasing the duty cycle of square wave signals, which can also be done with high precision using FPGA boards.

The signals must then be amplified in such a way that they can deliver the required power to drive the transducers and such that a suitable excitation voltage is applied.

For this purpose, different components can be used depending on the required power and voltage. To drive single transducers with an RMS voltage of up to 35 V, gate driver ICs are best suited because they are very easy to use and are designed for capacitive loads. IX4428 ICs were used for the prototypes developed during this work. An L298N dual H-bridge board can be used to amplify signals for multiple transducers at a maximum of two phases and a maximum RMS voltage of 35 V. To achieve higher voltages MOSFET full-bridges (e.g. FDMQ8403) with suitable gate drivers (MIC4606) can be used. However, it is important to ensure that the currents do not exceed the maximum current rating of the MOSFETs due to the capacitive behaviour of the transducers.

3

Manipulation of Acoustically Levitating Objects

Chapter Abstract

Acoustic manipulation of levitating objects can be used for many applications, such as the inspection of levitating objects and volumetric displays. For acoustic robot grippers it is useful if the levitating object can not only be levitated, but also manipulated. Manipulations can increase the levitation stability, and inaccuracies in the positioning of the gripper can be compensated for by precisely positioning the object acoustically. Furthermore, it is also possible to adjust the orientation of the object in such a way that it can be deposited correctly oriented on a target. In this chapter, a method for the stabilization of objects levitating in standing waves, a demonstrator for high precision position and orientation control using a closed-loop control system and a method for catching objects travelling through the acoustic field are presented. High-bandwidth manipulation using piezoelectric transducers is examined in order derive methods that consider effects resulting from rapid phase changes of the transducers.

3.1 Introduction

Acoustic manipulation methods have developed significantly in recent years. For a long time, devices that generate standing waves between two transducers or a transducer and a reflector were used to manipulate levitating objects [64, 65]. It was also possible to manipulate objects in resonance chambers using up to three transducers generating orthogonal standing waves [46].

In recent years, arrays of transducers were used that are capable of generating customized pressure fields [62]. Using arrays, it is possible to

shift and tilt standing waves, such that high position and orientation accuracy can be achieved.

For the development of ultrasonic robot grippers, acoustic manipulations of objects levitating in the gripper can be relevant for many reasons. Most important during the transport is the stability of the levitation. As asymmetric objects levitating in standing waves tend to spin around the symmetry axis of the pressure field [76, 77], manipulations of the pressure field can be used to generate a stabilizing torque, which stops the spin and increases the stability of the levitation. During the depositing process it can be required to adjust the orientation of the levitating object in order to place it on the target. This can be achieved with high precision using acoustic manipulation methods. Additionally, the gripper is usually positioned using a robot arm. Depending on the arm, significant deviations from the desired location of the gripper can occur, which can be compensated for by moving the levitating object acoustically, allowing for high precision positioning using low cost robot arms.

3.2 Position Control

The position of acoustically levitating objects can be manipulated in different ways. For acoustic robot grippers, the manipulation using arrays of transducers is the most relevant due to the low weight and the manipulation capabilities of such arrays.

A standing wave between two arrays of transducers is usually formed by focussing the acoustic pressure in the center between the two arrays and adding a 180° phase shift between them. Such a standing wave can be used to levitate an object at the center of the arrangement. The standing wave can be moved by focussing the pressure waves at the desired levitation position before adding the 180° phase shift. The resulting standing wave pressure fields for two levitation positions are shown in Fig. 3.1.

Position manipulation of acoustically levitating objects is also possible for other trap types, such as twin, vortex, or bottle traps. The method is very similar to the manipulation of the position using standing waves. First, the pressure is focussed at the levitation position and a phase signature depending on the trap type is added afterwards [62].

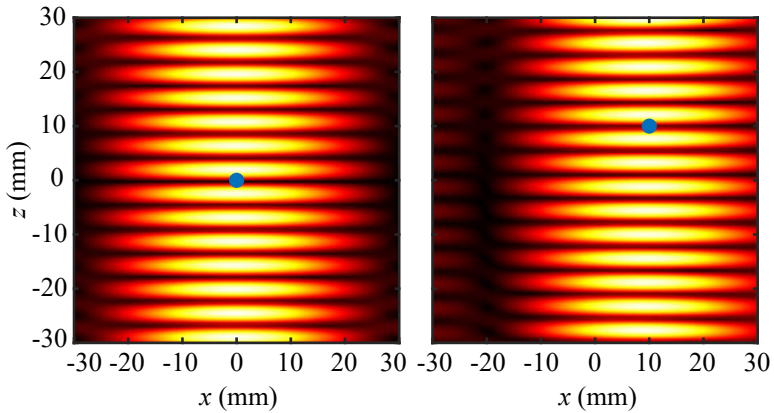


Fig. 3.1: Standing wave pressure field for a device consisting of two opposing arrays at a distance of 200 mm using transducers operating at 40 kHz. The levitation position is set to (a) $x = y = z = 0$ mm and (b) $y = 0$ mm, $x = z = 10$ mm.

Theoretically, this is possible for any arrangement of transducers. The better the pressure can be focussed at the levitation point, the better it is possible to generate a stable trap at this location.

For most robot grippers, the vertical force has to be larger than the horizontal stabilizing forces. Accordingly, an acoustic trap providing a high vertical force to counteract gravity (e.g. standing wave) has to be chosen.

3.3 Stabilization of Asymmetric Objects

Due to the rotationally symmetric pressure field, objects in standing waves tend to spin around the vertical axis [76,77]. To stop this spin and to control all six degrees of freedom, two methods have been developed.

The first method uses a single-axis acoustic levitator, that time-multiplexes a standing wave and a twin trap, for generating high vertical forces and a converging torque that locks the rotation, respectively. Subsequently, this method will be referred to as the switching-in-time (SIT) method. The ratio of the times during which the standing wave and the twin trap are applied can be used to tune the converging torque. However, an increase in torque results in a reduced vertical force for operation at maximum power, which limits the maximum density of the levitating object. Switching between different pressure fields requires two phase shifts of 180° per period for each transducer, resulting in a reduced acoustic power output and a further decreased vertical force during the transition process. With this method, an orientation accuracy of $<10^\circ$ and a torsional spring stiffness of up to 40 nNm/rad can be achieved [36,78].

The second method is presented in this work and allows acoustic trapping of asymmetric objects in all degrees of freedom by using piezoelectric transducers operating at two distinct frequencies. Subsequently, this is referred to as the multi-frequency (MF) method. A vertical standing wave and a horizontal standing wave are generated simultaneously at $f_1 = 40 \text{ kHz}$ and $f_2 = 25 \text{ kHz}$, respectively. The horizontal standing wave results in a pressure field similar in shape to that of a twin trap [78] and results in high forces. Therefore, it is possible to tune the converging torque by adjusting the acoustic power generated at f_2 , without reducing the vertical force generated by the standing wave at the frequency f_1 . The phase inversion is no longer required, making it possible to acoustically lock objects with densities of up to 7.3 g/cm^3 [36].

3.3.1 Multi-Frequency Stabilization

The MF method was experimentally evaluated using the levitator shown in Fig. 3.2. A vertical standing wave is generated by applying a phase shift of 180° between the transducers arranged in the upper and lower arrays. The resulting pressure field can be calculated as

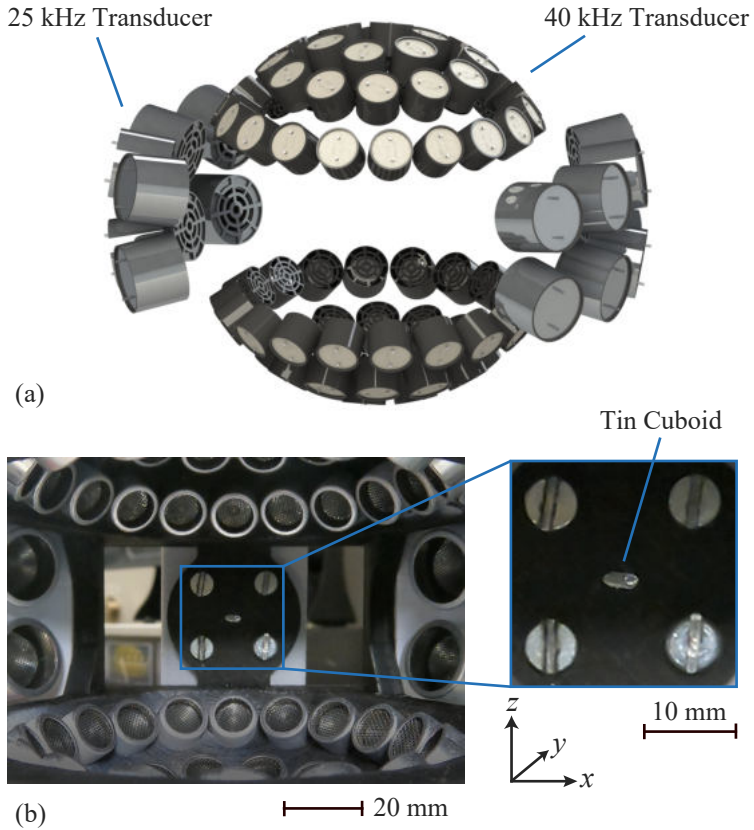


Fig. 3.2: (a) Rendering of the arrangement with ultrasound transducers with different resonance frequencies and (b) annotated photograph with a levitating tin cuboid. The setup was optimized for providing a maximum converging torque to lock the orientation of the levitated object. The shown acoustically locked object is a tin cuboid with side lengths of 0.8 mm x 0.8 mm x 5 mm.

$$p(x, y, z) = P_0 \sum_i J_0(kr_i \sin \theta_i) \frac{1}{d_i} e^{j\phi_i}, \quad (3.1)$$

where d_i , ϕ_i , P_0 , J_0 , k , r_i , and θ_i denote the distance of the i^{th} transducer to the considered point (x, y, z) , the phase shift applied to that transducer, a factor depending on the applied voltage, the zero-order Bessel function of the first kind, the wave number, the transducer radius, and the angle between the normal of transducer i and the point (x, y, z) , respectively.

A horizontal standing wave is generated at a frequency f_2 without affecting the vertical standing wave if $f_2 \neq f_1$. According to Eq. 2.20, the Gor'kov potential of two pressure fields of different frequencies is calculated as

$$U_{\text{tot}} = U_1 + U_2.$$

This is illustrated in Fig. 3.3, where a 40 kHz vertical standing wave (a, b) is superimposed with a 25 kHz horizontal standing wave (c, d), resulting in a Gor'kov potential that is no longer rotationally symmetrical in the xy plane (e, f). The equipotential lines of this Gor'kov potential can be approximated by ellipses. The eccentricity of these ellipses, i.e., the ratio of their semi-major and semi-minor axis lengths a and b , respectively, provides a measure for the converging torque.

For the verification of the MF method, experiments with an arrangement as shown in Fig. 3.2 were carried out. Electroacoustic transducers with a resonance frequency at 40 kHz and a diameter of 10 mm (Manorshi, MSO-A1040H07T) are arranged on three concentric rings of 6, 12, and 18 transducers, respectively. Two such arrays form the pole caps of a sphere with a diameter of 84 mm, i.e., the distance of an object levitated at the center of the arrangement to every transducer is identical, such that high vertical forces can be achieved. Additionally, 16 transducers with a resonance frequency at 25 kHz and a diameter of 16 mm (Manorshi, MSO-A1625H12T) are placed on two concentric rings with a diameter of 100 mm around the symmetry axis of the setup. These rings are arranged at different vertical positions and the transducers are oriented such that they face the center of the arrangement. The setup was designed to maximize the converging torque, i.e., the asymmetry of the Gor'kov potential in the horizontal plane. The asymmetry of the Gor'kov potential was assessed by numerical calculations for different

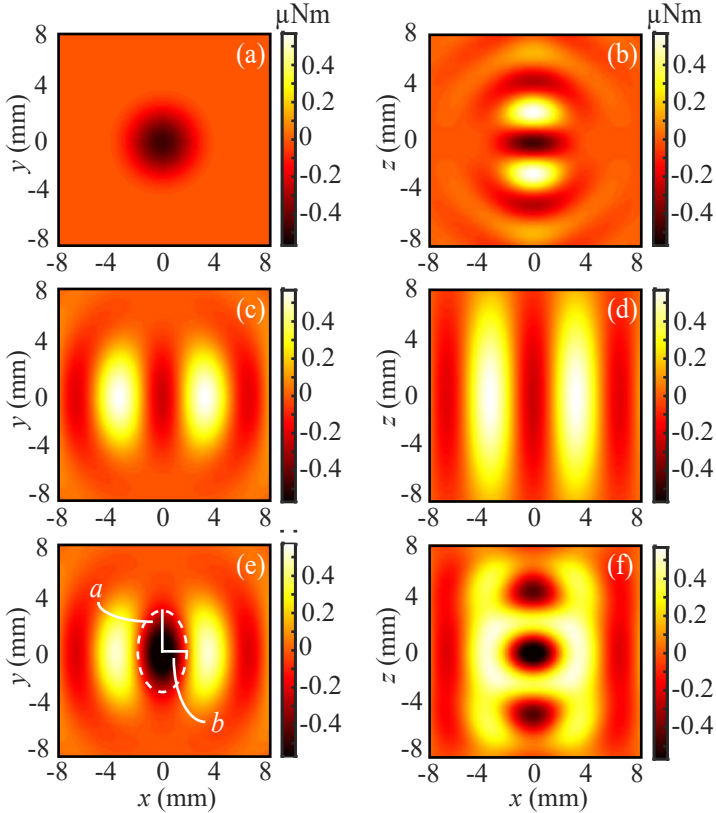


Fig. 3.3: Top view a) and side view b) of the Gor'kov potential generated by transducers operated at $f_1 = 40$ kHz with a voltage of $V_{1,\text{RMS}} = 12$ V. Top view c) and side view d) of the Gor'kov potential generated by transducers operated at $f_2 = 25$ kHz with a voltage of $V_{2,\text{RMS}} = 20$ V. Top view e) and side view f) of the superposition of the two Gor'kov potentials with a voltage ratio of $V_2/V_1 = 1.67$, providing high vertical forces and a converging torque. The eccentricity of the equipotential ellipse (dashed line) shown in e) is $a/b = 2.69$.

arrangements and numbers of transducers. For the selected arrangement, the resulting Gor'kov potentials correspond to those shown in Fig. 3.3.

For each frequency, two inverted signals are required to excite the transducers on opposite sides of the arrangement. These signals were generated using a Cyclone II FPGA board and amplified by an L298N dual H-bridge board. The phase of all transducers remains constant during operation, resulting in considerably higher acoustic power compared to the SIT method. Other methods require a large number of individually controlled channels [62, 71, 87] or careful geometric design [95].

Experiments with 3D-printed cuboids with an aspect ratio of 5:5:3 were conducted to analyze the size range for which stable locking is possible and to measure the orientation stability. Stable locking was defined in accordance with [78] as a maximum oscillation amplitude of 10° and a net zero location and orientation change. The orientation of the levitated cuboids was determined using video footage of the experiments and the Image Processing Toolbox in MATLAB. The obtained orientation stability is shown in Fig. 3.4a for plastic cuboids with average side lengths between 0.9 mm and 3.5 mm. Trapping forces of $7.7 \mu\text{N}$, $3.43 \mu\text{N}$, and $9.72 \mu\text{N}$ were achieved for the 0.9 mm object and $453 \mu\text{N}$, $202 \mu\text{N}$, and $572 \mu\text{N}$ for the 3.5 mm object in x , y , and z direction, respectively.

The torsional spring constant K_T was obtained based on the oscillation frequency ω_0 of the locked object, where ω_0 was again determined from video footage. K_T was then calculated as

$$K_T = \omega_0^2 \frac{m}{12} (L_{\text{long}}^2 + L_{\text{short}}^2), \quad (3.2)$$

where m , L_{long} , and L_{short} denote the mass, the longer side length, and the shorter side length of the cuboid, respectively. For the cuboids used in the experiments, $L_{\text{long}} = L_{\text{short}}$, thus Eq.(3.2) can be simplified to

$$K_T = \omega_0^2 \frac{m}{6} L^2. \quad (3.3)$$

The torsional spring constant depends on the size of the cuboid and the voltage applied to the 25 kHz transducers (acoustic power) as shown in Fig. 3.4b. If the magnitude of the 25 kHz pressure field approaches the same range as that of the 40 kHz pressure field, the object starts to wobble around the horizontal symmetry axis due to the increased rotational symmetry of the pressure field in Fig. 3.3f. Therefore, a limit of 20 V was chosen for the voltage applied to the 25 kHz transducers.

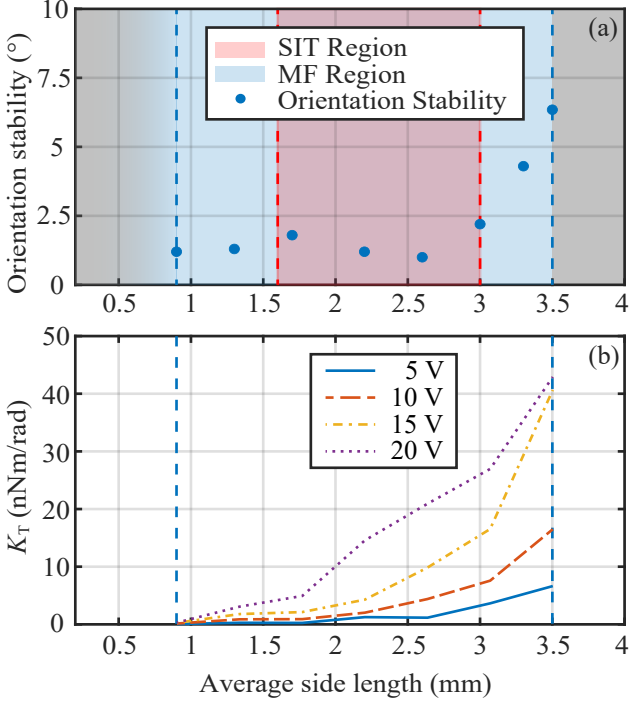


Fig. 3.4: a) Range of average side lengths of plastic cuboids, that can be locked acoustically using the MF method (blue), compared to the SIT method (red). The measured orientation stability for the MF method is shown by blue dots. b) Measured torsional spring constants for the MF method with voltages from 5 V to 20 V applied to the 25 kHz transducers.

The smallest object used for the experiments was a cuboid with an average side length of 0.9 mm. The results show that small objects achieve high orientation stability. Thus, it is expected that the lower limit for the average side length is significantly below 0.9 mm. For cuboids with average side lengths above 3.5 mm, oscillations around horizontal axes cause instabilities or even the ejection of the levitated particle from the acoustic trap. All cuboids between 0.9 mm and 3.5 mm were locked with an orientation stability better than 7.5° . As shown in [78], the approximation of the torque by a torsional spring is valid for oscillation amplitudes α smaller than 15° . The maximum torque for the system demonstrated in this work can therefore be calculated as $T = \alpha K_T$.

The achievable vertical forces were evaluated experimentally using small tin cuboids. Using the MF method, we have demonstrated acoustic locking of a tin cuboid with side lengths of 0.8 mm x 0.8 mm x 5 mm (average side length of 2.2 mm) and a density of $\rho = 7.3 \text{ g/cm}^3$, as shown in Fig. 3.2. An oscillation frequency of 5 Hz was measured resulting in a calculated torsional spring constant of 49.3 nNm/rad.

The MF and SIT methods can both be used for compact devices with a low complexity compared to methods that control the position and orientation of the levitated sample. The MF method provides a large stability region ranging from average side lengths of 0.9 mm to 3.5 mm, which corresponds to an increase of 86% compared to the SIT method. Operation of the 40 kHz transducers at full power and no losses due to phase changes during time-multiplexing facilitates the levitation of objects with a density of up to 7.3 g/cm^3 , which is roughly 6 times higher than the maximum density of 1.18 g/cm^3 achieved with the SIT method [78]. However, the MF method device requires laterally placed emitters, which is not the case with the SIT method. The attainable stiffness for both methods is in the range of 40-50 nNm/rad. Control of the system requires two channels of different frequency with constant phase, whereas the SIT method requires four channels of the same frequency with adjustable phase. The efficiency is higher, as the transducers are operated at constant phase. This facilitates the application of the MF method to novel use cases such as the transport of non-spherical objects by contact-less robotic grippers or the inspection of acoustically levitated samples [36].

3.4 Closed-Loop Control

Micro-manufacturing processes often require high precision for the transport of objects. If ultrasonic robot grippers are to be used for the automation of such processes, they must be able to reliably achieve the required accuracy. Unfortunately, the propagation of sound waves is highly dependent on the environment. Slight changes in temperature and humidity can cause the levitation position or orientation of the levitating object to change significantly enough to no longer meet these requirements. Furthermore, simplifications are often made when calculating the forces and torques acting on the object, and in some cases even the object geometry and material properties are not taken into account. The resulting inaccuracies can be compensated using a closed-loop control system. For this purpose, a system was developed, which can control the position and orientation of a levitating spheroid.

3.4.1 Setup

In order to control the position and orientation of a particle, suitable sensors are required. The sensors need to work in a contact-less manner in order to be considered for the use in a contact-less robot gripper. Various types of contact-less sensors, such as magnetic, capacitive or optical sensors are available. For this work, two CMOS cameras were used since cameras do not require any material properties of the levitating object. Furthermore, the field of view (FOV) of a camera can be made rather large using suitable optics. The distance, at which it can be used effectively, is mainly dependent on the camera resolution. Compared to position sensitive device sensors (PSD sensors), cameras are able to measure more information, which is required to determine the orientation of a levitating object, have a larger FOV and the measurement data is easier to analyse. However, image processing algorithms are more time consuming than analysing the outputs of a PSD sensor and the control bandwidth is therefore limited.

The control of spheroidal objects in five degrees of freedom is investigated using a levitator as shown in Fig. 3.5.

3.4.2 Open-loop Control

A twin trap is used to levitate the spheroidal object acoustically. The phase shifts of the individual sound waves are set in such a way that

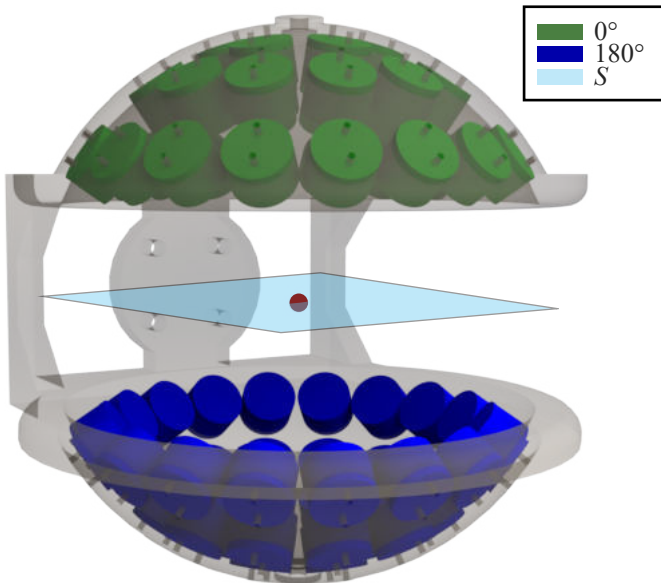


Fig. 3.5: The system, which is used to levitate and manipulate the objects. The light blue separation plane divides the transducers into two halves, which are controlled with a phase of 0° (green) and 180° (blue), respectively.

they constructively superimpose at the levitation point L . Subsequently, the transducers are divided into two halves, which are separated by a plane S . A phase shift of 180° has to be added to one of the two halves. Due to the spherical arrangement of the transducers, no phase shifts are required to focus the ultrasonic waves in the center of the sphere. Therefore, with a horizontal separation plane through the center of the arrangement as shown in Fig. 3.5, a phase shift of 180° between the two halves is sufficient for the horizontal levitation of a spheroidal object at the center of the arrangement. The resulting pressure fields for different levitation positions are shown in Figs. 3.6a,b.

The orientation of a spheroid is determined by a rotation around the y -axis and around the z -axis afterwards. Tilting of the spheroid can be achieved by tilting the separation plane S . The rotation angle of S around the y - and z -axis are referred to as $\alpha_{y,S}$ and $\alpha_{z,S}$, respectively. They do not coincide with the rotation angles of the spheroid ($\alpha_{y,\text{real}}$ and $\alpha_{z,\text{real}}$). An adjustment of $\alpha_{y,S}$ or $\alpha_{z,S}$ will only affect the orientation of the spheroid, if at least one transducer has moved to the other side of S after the adjustment.

This allows rotation in discrete steps. To achieve more precise rotation, the phase transition can be made smoother when a transducer is changing from one side of S to the other. In this case, the duty cycle and thus the acoustic power of the transducer with the original phase is steadily reduced as soon as the transducer is close to the separation plane, in such a way that the power is zero when the transducer is located on the separation plane. Subsequently, the power is continuously increased with the new phase until the maximum power is reached.

For small angles ($\alpha_{y,\text{real}} < 10^\circ$), $\alpha_{y,S}$ is significantly larger than $\alpha_{y,\text{real}}$. To compensate for this, $\alpha_{y,S}$ is increased in this range and decreased accordingly above 10° , in such a way that the actual rotation angle is closer to the nominal value.

The resulting pressure fields for different levitation orientations are shown in Figs. 3.6c,d.

3.4.3 Pinhole Camera

The pinhole or perspective camera is a simple model of a camera. It is illustrated in Fig. 3.7. In this model, all light arriving passes through a single point called pinhole or optical center C . It assumes a planar camera sensor with the sensor coordinate system (u, v) , which is located

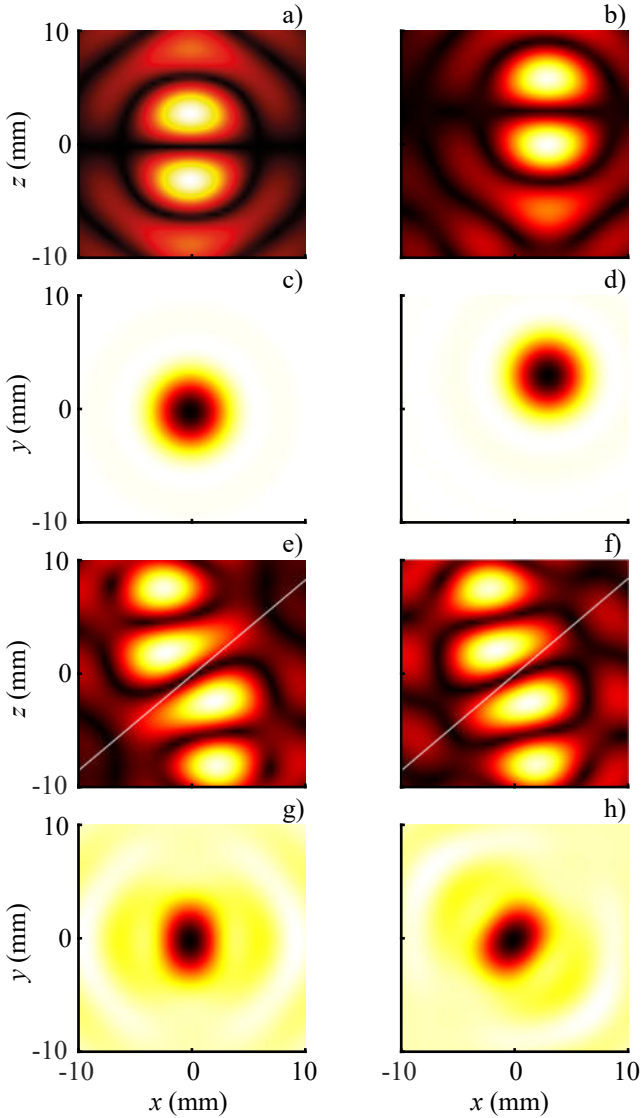


Fig. 3.6: Pressure fields for horizontal levitation at the origin (a, c), for a translation of the object (b, d), for a rotation around the y -axis (e, g) and for a rotation around the y -axis and z -axis (f, h).

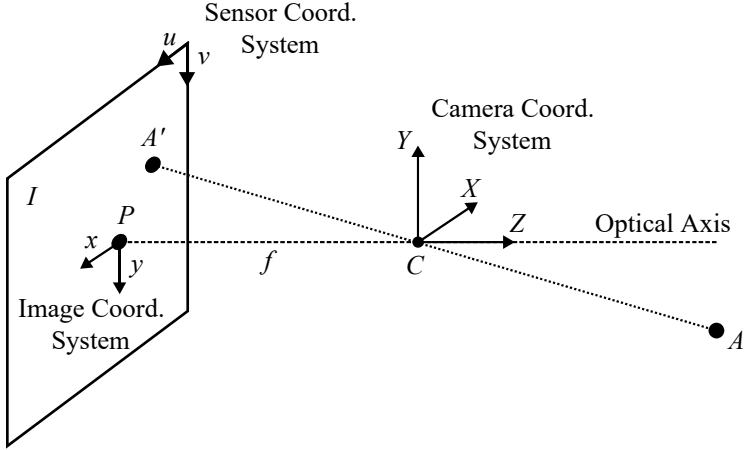


Fig. 3.7: Illustration of the principle of a pinhole camera, which is used to calculate the position of a levitating object with one degree of freedom.

in the plane referred to as image plane I with the image coordinate system (x, y) . The axis orthogonal to I and through C is called optical axis. The intersection between the optical axis and the image plane is referred to as principle point P and is the origin of the image coordinate system. The camera coordinate system (X, Y, Z) describes the position relative to C .

The projection A' of a point $A = (X_A, Y_A, Z_A)'$ to the image coordinate system is calculated as

$$x = f \frac{X}{Z}, \quad (3.4)$$

$$y = f \frac{Y}{Z}, \quad (3.5)$$

where f denotes the focal length, which is defined as the distance between C and P . To obtain the sensor coordinates of a point in the image coordinate system, the sensor coordinates of $P = [x_0 y_0]'$ have to be added to the image coordinates. Furthermore, the metric sensor coordinates are usually converted to pixel sensor coordinates using scaling factors k_u and k_v , resulting in

$$\begin{bmatrix} u \\ v \\ 1 \end{bmatrix} \propto \begin{bmatrix} k_u f & 0 & k_u x_0 \\ 0 & k_v f & k_v y_0 \\ 0 & 0 & 1 \end{bmatrix} \begin{bmatrix} X \\ Y \\ Z \end{bmatrix} \quad (3.6)$$

and the camera intrinsic matrix

$$A = \begin{bmatrix} \alpha_u & 0 & u_0 \\ 0 & \alpha_v & v_0 \\ 0 & 0 & 1 \end{bmatrix}, \quad (3.7)$$

where $\alpha_u = k_u f$, $\alpha_v = k_v f$, $u_0 = k_u x_0$, and $v_0 = k_v y_0$.

In reality, distortions of the projections occur due to the finite size of the aperture. The calculation of the image coordinates can be adjusted as

$$x'_d = x + \delta_x^{(r)} + \delta_x^{(t)} \quad (3.8)$$

$$y'_d = y + \delta_y^{(r)} + \delta_y^{(t)} \quad (3.9)$$

in order to take radial distortions $\delta^{(r)}$ and tangential distortions $\delta^{(t)}$ into account.

The radial distortions can be approximated using Taylor series

$$\delta_x^{(r)} = x(k_1 r^2 + k_2 r^4 + \dots) \quad (3.10)$$

$$\delta_y^{(r)} = y(k_1 r^2 + k_2 r^4 + \dots), \quad (3.11)$$

where $r = \sqrt{x^2 + y^2}$ and k_1, k_2, \dots denote the radial distortion coefficients.

The tangential distortion can be approximated as

$$\delta_x^{(t)} = 2p_1 xy + p_2(r^2 + 2x^2) \quad (3.12)$$

$$\delta_y^{(t)} = 2p_1(r^2 + 2y^2) + 2p_2 xy, \quad (3.13)$$

where p_1 and p_2 denote the tangential distortion coefficients.

In order to determine the intrinsic matrix A and the distortion coefficients, the camera has to be calibrated. This can be achieved by using pictures of a calibration rig with known structure, e.g. a chessboard, from multiple orientations [96, 97].

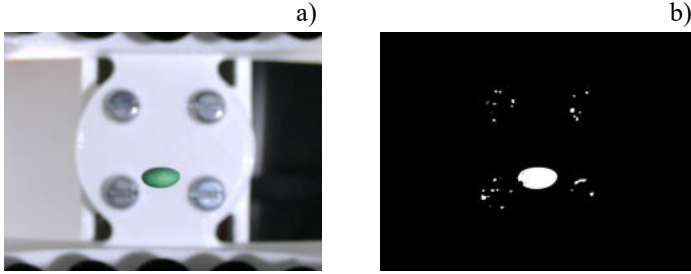


Fig. 3.8: An image of the levitating spheroid taken by the camera (a) and the resulting image after thresholding (b).

3.4.4 Object Detection

After the cameras have been calibrated, the levitating object can be identified using the camera images. Two methods were investigated and compared with each other. Thresholding divides an image based on intensity or color values, as shown in Fig. 3.8. This can be described mathematically with pixel values before $p(x, y)$ and after $q(x, y)$ thresholding with threshold T as

$$q(x, y) = \begin{cases} 1 & \text{if } p(x, y) > T \\ 0 & \text{if } p(x, y) \leq T \end{cases} \quad (3.14)$$

The object is then identified as the largest connected area [98].

The detection of the object using edge detection first finds the edges in an image, and then connects them to find the object boundaries, as shown in Fig. 3.9. There are numerous methods to detect edges, which generally either compare the gradient in an image to a threshold or look for zero crossings in the second derivative. Possible edge detectors would be the Sobel or Canny operators [98]. This method results in inaccuracies for moving or oscillating objects due to blurring of the images. Therefore, thresholding yielded better results for the detection of acoustically levitating objects.

After the object has been detected using thresholding, an ellipse can be fitted to the largest connected area, as shown in Fig. 3.10. The center of the ellipse is used for position determination and the rotation for orientation determination.

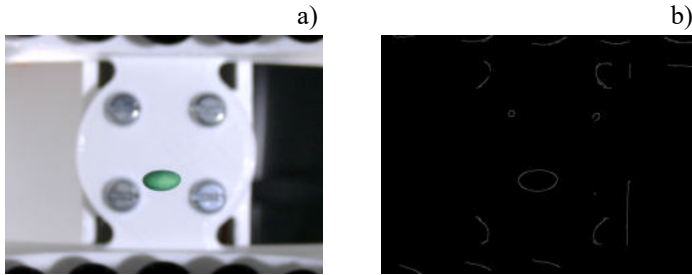


Fig. 3.9: An image of the levitating spheroid taken by the camera (a) and the resulting image after edge detection (b).

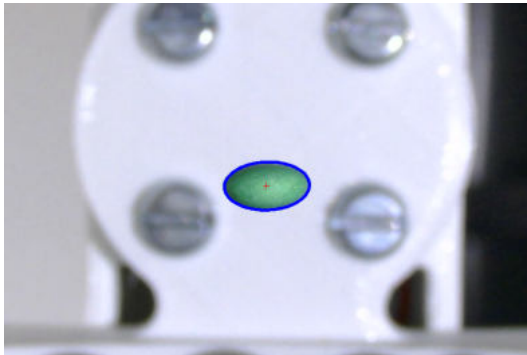


Fig. 3.10: An image of the levitating spheroid taken by the camera with a fitted ellipse and its center point using the thresholding method.

To limit the area in which the object has to be detected and to increase the performance of the algorithm, the image can be cropped in an area around the last known position prior to object detection.

3.4.5 Position Measurement

Position measurement in a three-dimensional space requires at least two cameras. The respective position in the two-dimensional image coordinate system can be determined from the images of both cameras. To determine the coordinates in the three-dimensional global coordinate system, a triangulation, as illustrated in Fig. 3.11, is required.

The measured coordinates in the image coordinate systems 1 and 2 are denoted by $({}^1x_{\text{meas}}, {}^1y_{\text{meas}})$ and $({}^2x_{\text{meas}}, {}^2y_{\text{meas}})$, respectively. The coordinates of a point ${}^c_1p = (x, y, z)$ in the camera coordinate system of camera 1 can be transformed to coordinates in the camera coordinate system of camera 2 by a translation and a rotation as

$${}^c_2p = R {}^c_1p + T. \quad (3.15)$$

Based on the coordinates of the point c_1P projected onto the image coordinate system 1 ${}^c_1P'_1$, the coordinates of c_1P can be determined to within one degree of freedom as

$${}^c_1P = ({}^c_1c_1 - {}^c_1P'_1)s = -{}^c_1P'_1s, \quad (3.16)$$

where s denotes a positive real number and the optical center of camera 1 c_1 is selected as the origin of the camera coordinate system 1.

The point e_2 corresponds to the projection for $s = 0$, which is the projection of the optical center c_1 of camera 1. q_1 is the projection resulting for $s = \infty$.

The line ${}^c_1P = {}^c_1P'_1s$ transformed to the camera coordinate system 2 results in

$${}^c_2P = R {}^c_1P'_1s + T = \begin{bmatrix} c_2x_2 \\ c_2y_2 \\ c_2z_2 \end{bmatrix}, \quad (3.17)$$

which can be projected onto the image coordinate system of camera 2 i_2 as

$$i_2P = \left(f \frac{c_2x_2}{c_2z_2}, f \frac{c_2y_2}{c_2z_2} \right). \quad (3.18)$$

These coordinates can be compared to ${}^i_2P_{\text{meas}} = ({}^i_2x_{\text{meas}}, {}^i_2y_{\text{meas}})$ in order to get the value of s and therefore the coordinates of P [96].

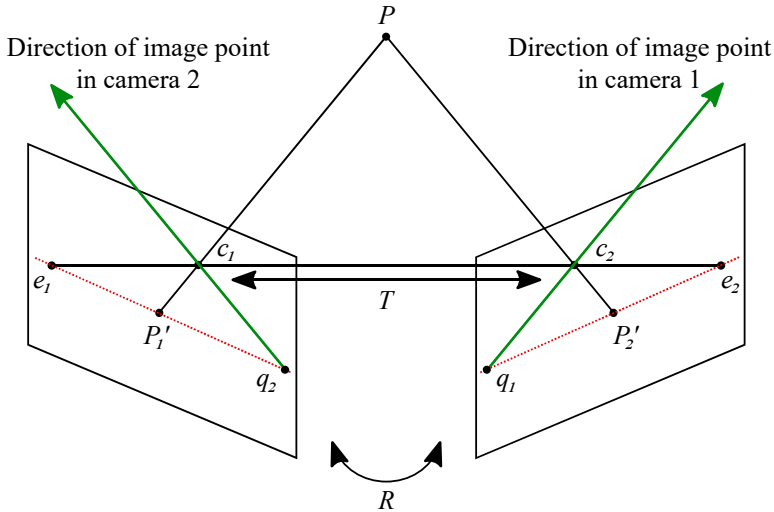


Fig. 3.11: Illustration of the triangulation method, which is used to calculate the global position using the position measurements of two cameras.

3.4.6 Orientation Measurement

Using two cameras, it is not possible to determine the orientation of an ellipsoidal object in six degrees of freedom without knowing more information about the texture or the dimensions of the object. This would require the use of a third camera. To keep the system as simple as possible, we therefore developed a demonstrator that can control the position and orientation of oblate spheroids. The rotation around the symmetry axis of the spheroid can neither be detected nor controlled with the levitator developed in this work. The demonstrator is shown in Fig. 3.12.

The projection of a spheroid onto a camera always results in an ellipse. The major axis of the ellipse can be used to determine the symmetry axis of the spheroid since the symmetry axis is always perpendicular to the projected major axis. Using one image from both cameras, the symmetry axis and therefore the orientation of the spheroid can be determined using the cross product of the two major axis. This method works as long as the rotation of the spheroid around the y -axis is not exactly 90° or 270° . For these cases, the major axes of the projected



Fig. 3.12: The demonstrator used to verify the developed methods. It uses 72 transducers operating at 40kHz and two cameras for the position and orientation detection.

ellipses are both parallel, the cross product is zero and the rotation around the z -axis can not be determined.

3.4.7 Control System

Two ELP CMOS high-speed cameras were used for the measurements. They offer different resolutions depending on the frame rate. For the experiments, we read out the cameras with a resolution of 1280x720 pixels at 180 FPS. One camera was aligned along the x -axis and the other along the y -axis. The 90 degree angle between the cameras simplifies the evaluation of the position measurement, but is not mandatory. The cameras were calibrated using a chessboard pattern.

All five degrees of freedom are controlled independently. The controllers generate five parameters, which are used to calculate the required excitation signals. These are then generated on an FPGA board and amplified by gate driver ICs (IX4428). An overview of this system is shown in Fig. 3.13.

The input to the controller is low-pass filtered to ensure the stability of the levitation, as shown in Fig. 3.14.

The five degrees of freedom are filtered independently with lowpass filters F_L of the form

$$F_L = \frac{\omega_L}{\omega_L + s}, \quad (3.19)$$

where ω_L denotes the cutoff frequency and was set to $\omega_L = 1$ rad/s for the position controllers and to $\omega_L = 2$ rad/s for the orientation controllers. The filters are implemented in discrete time using the trapezoidal integration method [99].

For the closed-loop controller, the five parameters x , y , z , α , and γ were assumed to be independent. Therefore, the closed-loop controller could be obtained using loop shaping [99]. All controllers are of the form

$$K(s) = \frac{g(1 + a\tau s)}{s(1 + \tau s)} \quad (3.20)$$

with $\tau > 0$ and $0 < a < 1$, which then results in an integrator with additional phase lag between τ and $a\tau$. The parameter g can be used to scale the transfer function and thereby adjust the crossover frequency ω_c .

The parameters for a maximum phase lag of P_L at the crossover frequency can be calculated as

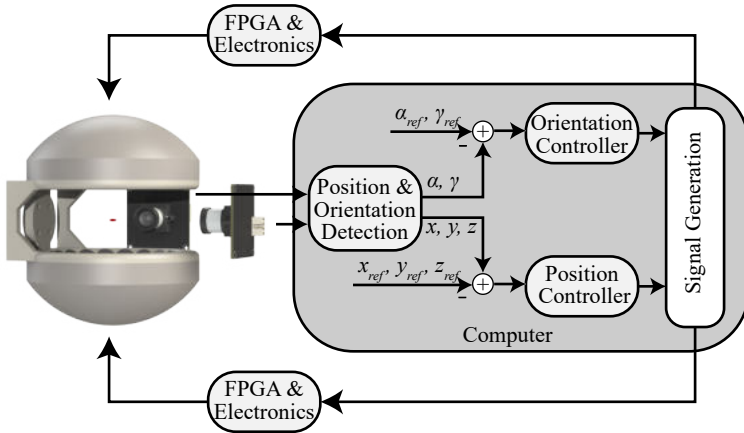


Fig. 3.13: An overview of the closed-loop control system. Two cameras and image processing algorithms are used to determine the position and orientation of a levitating spheroid. The measured values are fed to five individual controllers resulting in five parameters for the open-loop algorithm, which determines the phase and duty cycle for each transducer. The signals for the transducers are then generated on an FPGA board and amplified by gate driver ICs.

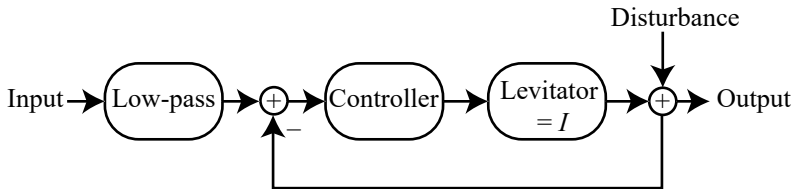


Fig. 3.14: The schematics of the closed-loop controller used to control the position and orientation of the levitating spheroid. The input is low-pass filtered for the stability of the controller.

$$a = \frac{1 - \sin(P_L)}{1 + \sin(P_L)} \quad (3.21)$$

$$\tau = \frac{1}{\omega_c \sqrt{a}} \quad (3.22)$$

$$g = \left| \omega_c \frac{1 + \tau j \omega_c}{1 + a \tau j \omega_c} \right|. \quad (3.23)$$

The crossover frequencies and the maximum phase lag were determined experimentally as $\omega_c = 2$ rad/s (position control), $\omega_c = 1$ rad/s (orientation control) and $P_L = 10^\circ$.

3.4.8 Results

The experiments have shown that the open loop algorithm is not accurate for all positions and orientations. If only the position is adjusted and the object is located close to the center of the arrangement, the deviations are relatively small. Nevertheless, there is a small error that the closed loop controller can compensate. This is shown in Fig. 3.15 for a step response of 5 mm in x direction and 5 mm in $-z$ direction.

Furthermore, it was evident that the individual parameters are not independent of each other. If the object is to be rotated around the y -axis, the orientation around the z -axis is affected as well, as shown in Fig. 3.16. However, the closed-loop controller is able to compensate for this. Due to the good performance and the increasing complexity of the controller when the coupling between the five parameters is taken into account for the open-loop control algorithm, it was decided not to include it.

To investigate the performance of the controller, a tilted circle of object positions was traversed while the object was tilted 30° around the y - and z -axis, as shown in Fig. 3.17. It showed that the position and orientation with the open-loop controller can deviate strongly from the reference. The coupling between the parameters is also clearly visible, since the orientation reference does not change, but it varies strongly when using the open-loop controller. The closed-loop controller can compensate both effects and achieves precise control of the position and orientation.

The measurements have shown that the control of position and orientation can be improved if a closed-loop system is used. This effect

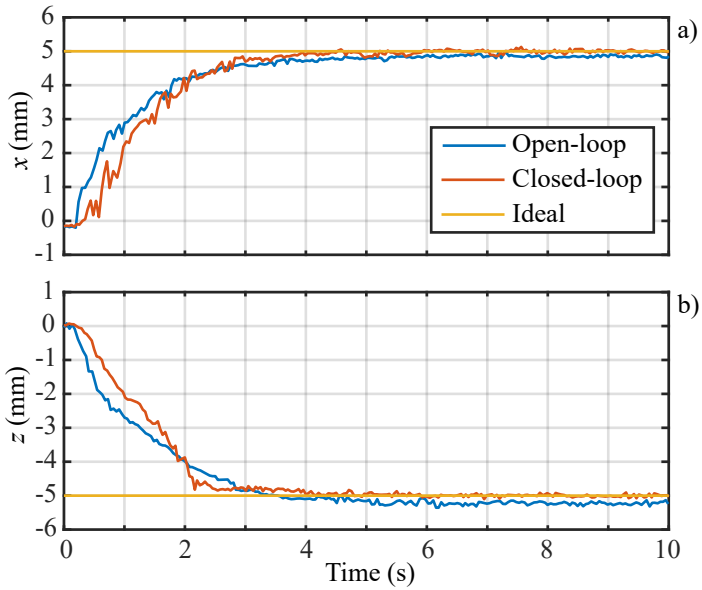


Fig. 3.15: Position measurement after a step response in x -direction (a) and $-z$ -direction (b). The closed-loop controller is capable of compensating the small steady state error occurring with the open-loop system.

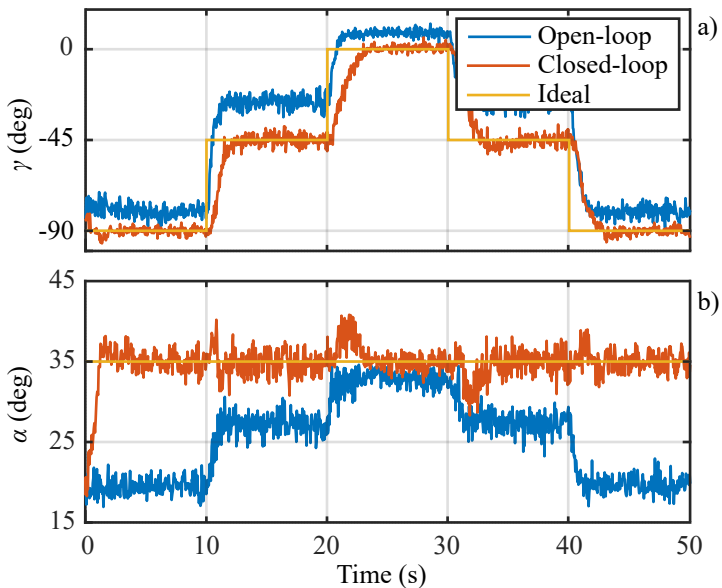


Fig. 3.16: Orientation measurement for multiple reference steps for the rotation angle γ (a) and a constant reference angle of $\alpha = 35^\circ$ (b). The open-loop controller shows steady state errors for both rotation angles and a strong coupling between the two individually controlled angles. The closed-loop controller is capable of compensating the steady state errors and allows the individual control of the rotation angles.

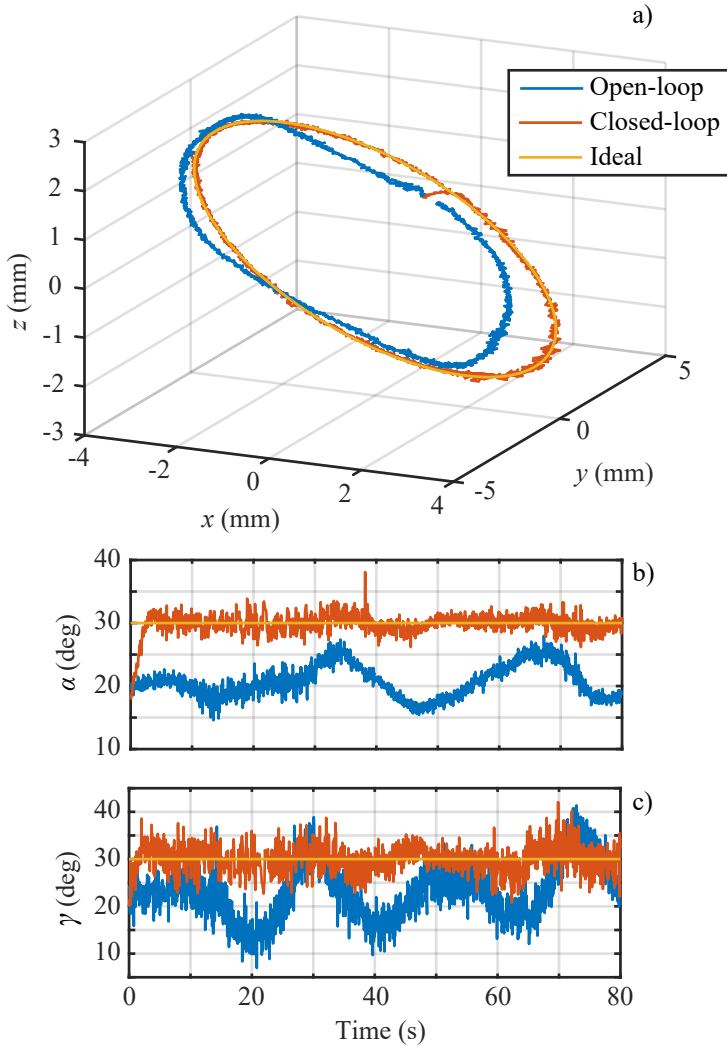


Fig. 3.17: Traverse of a tilted circle of object positions with constant orientation. The measurements show accurate position (a) and orientation (b,c) control with the closed-loop controller, while the open-loop system deviates strongly from the reference value.

becomes more significant the larger the inaccuracies with the open loop system are. These inaccuracies can originate from simplifications applied to the open-loop system in order to keep the algorithm as simple as possible. However, other factors such as transducer manufacturing tolerances, temperature, and humidity can also affect the accuracy of the open-loop control.

In order to implement a closed-loop controller, the object geometry must be known and the image processing algorithms must be able to recognize the degrees of freedom to be controlled based on the camera images. For some applications, which require the control of complex shaped objects, LiDAR technology could be used to detect the position and orientation of a levitating object. If high bandwidth position control is required, the cameras could be replaced by PSD sensors, that are evaluated using FPGAs.

3.5 Acoustic Catching

There are several ways to insert objects into an acoustic levitation field. Besides contact-based solutions like tweezers, there are also contact-less methods, which are discussed in Chapter 4. However, for certain processes the best solution is to drop an object and then decelerate and catch it using acoustic forces. This would also be possible for the contact-less transfer of an object between two grippers. Furthermore, this method can be used to catch ejected liquid droplets as described in Chapter 5.

A demonstrator was developed to investigate the extent to which acoustic forces can be used to catch a solid object. The demonstrator consists of two opposing flat arrays of transducers, which are operated at their resonance frequency of 40 kHz. The separation distance between the two arrays was chosen to be 80 mm such that the axial and radial stiffness were in a suitable range. By appropriately adjusting the phase of each transducer, the position of the levitated object can be manipulated. For the catching experiments, expanded polystyrene balls with a diameter of approximately 2.7 mm were acoustically brought to a specific height and dropped by switching off the transducers. Two cameras were positioned to capture a cube-shaped volume with a side length of 40 mm. Using the two images and image processing algorithms, the position of the particle was determined. The demonstrator is shown in Fig. 3.18.

The particle was then caught using two methods. Static catching generates an acoustic trap, which is able to decelerate and catch the falling ball without moving the trap. The dynamic catching method decelerates the particle by moving the trap with the particle during the dynamic interval and then applies a static trap to stop the particle.

3.5.1 System and Delays

The system uses two ELP-USBFHD08S-L36 cameras to take pictures of the object, which are then used for the position evaluation. The cameras communicate with a PC and provide images with a frame rate of 260 FPS at a resolution of 640x360 pixels. The position of the particle is calculated on the computer before a controller determines the reference value of the acoustic trap in such a way that the particle can be decelerated and caught. The controller also takes into account the delays that occur in the system. Subsequently, the reference value is transferred via a UART interface to an FPGA board, which calculates the phase

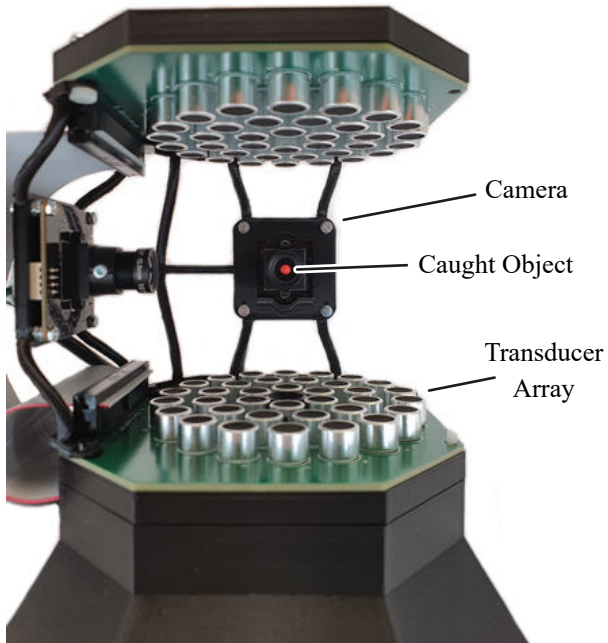


Fig. 3.18: The demonstrator used to verify the two developed methods to catch objects using acoustic levitation forces.

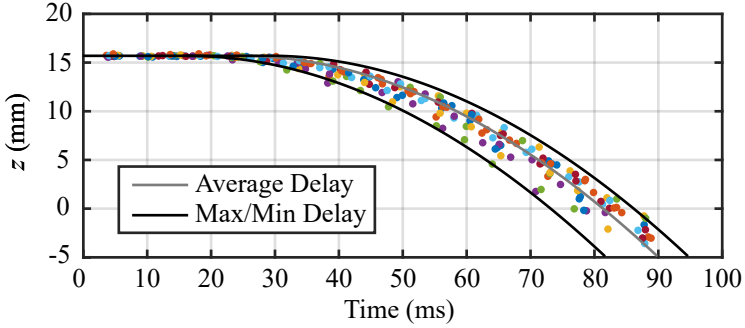


Fig. 3.19: Position measurements of 16 particles falling from a height of 16 mm. The signal to turn off the transducers is sent from the computer to the FPGA at $t = 0$ ms. An average delay for the internal camera video pipeline, the USB request to the cameras and the image transmission of 23.683 ms with high variance was measured.

shifts of the individual transducers and generates the corresponding excitation signals. These are then amplified by IX4428 gate driver ICs and applied to the transducers.

During this process, several delays occur, which must be taken into account by the controller. The triangulation of the particle position which requires about 5 ms can be measured and taken into account by the controller. The communication between the computer and the FPGA board (measured) and the wave propagation from the transducers to the particle (calculated) take about 0.28 ms and 0.24 ms, respectively. The remaining delay caused by the internal camera video pipeline, the USB request to the cameras and the image transmission can not be measured independently, but the total delay was measured to be about 23.683 ms in average with significant variance. The delay was measured by sending a signal to turn off the transducers at $t = 0$ ms and measure the position of the falling particle afterwards. The image arrival time is then compared with the time when the particle was located at the calculated position using Eq. 3.30. The position measurements and the predicted trajectory for a delay of 23.683 ms, for the minimum delay of about 16 ms, and for the maximum delay of about 29 ms are shown in Fig. 3.19.

Due to the high variance caused by the cameras, an open-loop approach using a calculated time difference between switching off the transducers and generating a static or dynamic trap was used for the experiments. For a reliable closed-loop system, cameras with constant delays or cameras that provide a timestamp of when the image was taken would have to be used.

3.5.2 System Modelling

For the experiments, it was assumed that the object (ball) is falling in the negative z -direction, i.e. vertically. The external forces acting on the object are the weight force in the negative z -direction and the drag in the positive z -direction. In addition, acoustic forces from the catcher act in the positive z -direction.

The drag force on a spherical object with cross-sectional area A is calculated as

$$F_d = \frac{1}{2} C_d A \rho_0 \dot{z}^2, \quad (3.24)$$

where $C_d = 0.47$ and $\rho_0 = 1.18 \text{ kg/m}^3$ denote the drag coefficient and the density of air, respectively. To account for this force in a linear system it can be linearised as

$$F_{d,\text{lin}} = C_d A \rho_0 \dot{z} = k_d \dot{z}. \quad (3.25)$$

The acoustic radiation force can also be linearised around the levitation position as

$$F_{r,\text{lin}} = k(z_{\text{trap}} - z) = ku. \quad (3.26)$$

During the first phase of the experiment, the particle is in free fall and the acoustic force is $F_r = 0$. In this case, the system can be described as

$$m \cdot \ddot{z} = F_d - F_g. \quad (3.27)$$

The maximum velocity that can be reached is calculated as

$$\lim_{t \rightarrow \infty} v_z(t) = v_\infty = -\sqrt{\frac{2mg}{k_d}}. \quad (3.28)$$

Thus, by solving the differential equation, the trajectory of the particle can be calculated as

$$v_z(t) = -v_\infty \tanh\left(\frac{gt}{v_\infty} - \operatorname{arctanh}\left(\frac{v_0}{v_\infty}\right)\right), \quad (3.29)$$

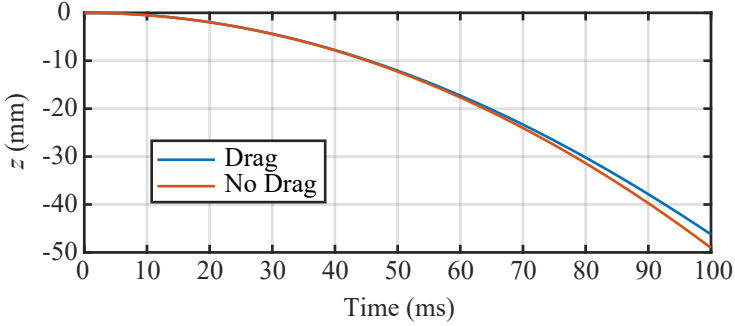


Fig. 3.20: Trajectory of a falling expanded polystyrene ball with a diameter of $d = 2.7$ mm and a density of $\rho = 0.04$ g/cm³ with (blue) and without drag (red).

$$z(t) = -\frac{v_\infty^2}{g} \ln \left(\sqrt{1 - \frac{v_0^2}{v_\infty^2}} \cosh \left(\frac{gt}{v_\infty} - \operatorname{arctanh} \left(\frac{v_0}{v_\infty} \right) \right) \right) + z_0. \quad (3.30)$$

For low velocities, which are achieved for drop heights < 40 mm, the drag can be neglected and the resulting error of the position calculation is less than 5%. For this case the trajectory can be calculated as

$$v_{z,\text{approx}}(t) = -gt + v_0 \quad (3.31)$$

$$z_{\text{approx}}(t) = -\frac{1}{2}gt^2 + v_0t + z_0. \quad (3.32)$$

The comparison of the trajectories with and without consideration of the drag is shown in Fig. 3.20.

For the second phase of the experiment, the catcher is turned on. During this phase the system can be described as

$$m\ddot{z} = ku - mg - k_d\dot{z}. \quad (3.33)$$

This ODE can be put into linear affine state space as

$$\vec{x} = \begin{bmatrix} z \\ \dot{z} \end{bmatrix}, \quad w = u - \frac{mg}{k} \quad (3.34)$$

$$\dot{\vec{x}} = A\vec{x} + Bw \quad (3.35)$$

$$z = C\vec{x} + Dw \quad (3.36)$$

with

$$A = \begin{bmatrix} 0 & 1 \\ 0 & -\frac{D}{m} \end{bmatrix}, \quad B = \begin{bmatrix} 0 \\ \frac{k}{m} \end{bmatrix}, \quad C = [1 \quad 0], \quad D = [0]. \quad (3.37)$$

3.5.3 Measurement of the Trap Stiffness

The system is modelled as a damped spring oscillator as shown in Eq. 3.33. The analytical solution of this ODE is

$$z(t) = R \exp\left(-\frac{k_d}{2m}t\right) \cos(\omega t - \varphi) + z_0 - \frac{mg}{k}. \quad (3.38)$$

To determine the parameters of this equation, step responses in radial and axial directions were measured. It was found that the approximation by a damped spring oscillator is not very accurate and the stiffness at low deflection is higher than at high deflection. Therefore, the equation was adjusted to

$$\hat{x}(t) = c_1 \exp(c_2 t) \quad (3.39)$$

$$z(t) = \hat{x}(t) \cos\left(\frac{2\pi t}{c_3 + c_4 \hat{x}(t)^{c_5}} + \frac{2\pi}{c_6}\right) + c_7 \quad (3.40)$$

with seven parameters c_1 to c_7 and fitted to the measurement data as shown in Fig. 3.21.

The spring stiffness can then be calculated as

$$k = \omega(\hat{x})^2 m \quad (3.41)$$

with

$$\omega(\hat{x}) = \frac{2\pi}{c_3 + c_4 \hat{x}^{c_5}} \quad (3.42)$$

resulting in a force of

$$F(\hat{x}) = -k\hat{x} = -\omega(\hat{x})^2 m \hat{x} = -\left(\frac{2\pi}{c_3 + c_4 \hat{x}^{c_5}}\right)^2 m \hat{x}. \quad (3.43)$$

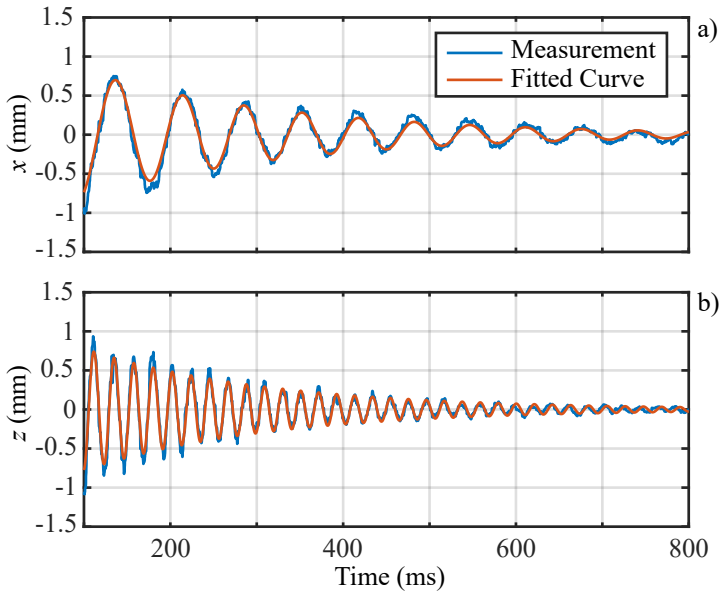


Fig. 3.21: Step response measurement in radial (a) and axial (b) direction used to measure the stiffness.

Using these equations, the radial and axial stiffness for the range between -1 mm and 1 mm can be linearised as

$$k_{\text{radial}} = \left(\frac{2\pi}{c_3 + c_4 10^{-3c_5}} \right)^2 m \hat{x} = 1.3 \text{ uN/mm} \quad (3.44)$$

$$k_{\text{axial}} = \left(\frac{2\pi}{c_3 + c_4 10^{-3c_5}} \right)^2 m \hat{z} = 21.3 \text{ uN/mm} \quad (3.45)$$

for an excitation voltage amplitude of $V_{\text{ex}} = 6$ V. Due to the linear relationship between excitation voltage and stiffness, the radial and axial stiffness for arbitrary excitation voltages can be calculated as

$$k_{\text{radial}} = 0.22 \mu\text{N}/(\text{V} \cdot \text{mm}) \cdot V_{\text{ex}} \quad (3.46)$$

$$k_{\text{axial}} = 3.55 \mu\text{N}/(\text{V} \cdot \text{mm}) \cdot V_{\text{ex}}. \quad (3.47)$$

3.5.4 Static Catching

The static catching method was tested with a expanded polystyrene ball with a diameter of $d = 2.7$ mm and a mass of $m = 0.41$ mg. For an excitation voltage of 13 V, the maximum velocity of the particle could be $v_{\text{max}} = 1.12$ m/s, if the trap would be placed perfectly. This velocity is reached after falling a distance of 8.8 cm. However, in our experiments drop heights of about 25 mm were the limit for reliable catching. The measurement of the position during the drop and the catching process is shown in Fig. 3.22a. For larger drop heights, the timing accuracy of the trap generation was too low and it was not possible to catch the objects reliably.

3.5.5 Dynamic Catching

The dynamic catching method was tested with the same particle as the static catching method. The dynamic catching method uses a moving trap to decelerate the object before a static trap is generated to stop the object. Therefore, the maximum drop height should be increased compared to the static method. However, due to the limited control volume of our demonstrator (-20 mm $< z < 20$ mm), only a very short interval of a few millimetres can be used for a dynamic trap as shown in Fig. 3.22b, resulting in small differences of maximum drop height

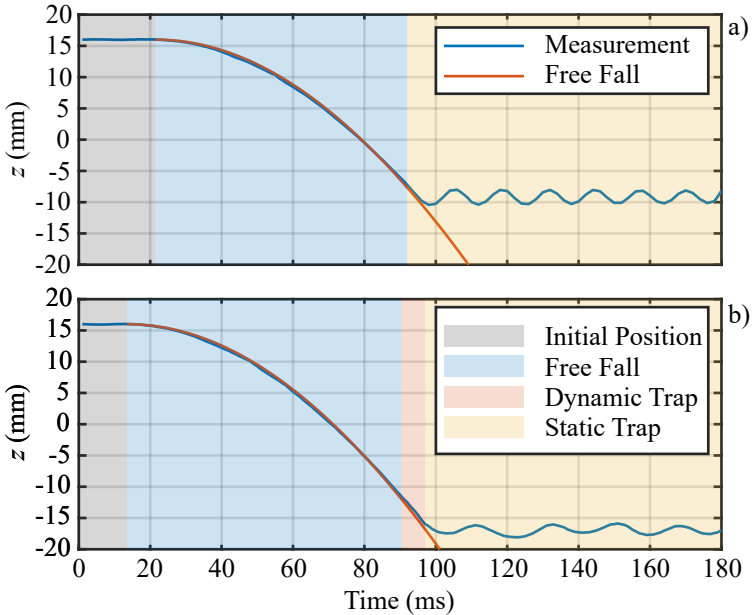


Fig. 3.22: The position measurement of an expanded polystyrene particle with a diameter of 2.7 mm caught after 25 mm of falling using the static catching method (a) and caught after falling 29 mm using the dynamic catching method with a dynamic zone of 4 mm (b).

between the two methods. With the dynamic catching method, objects dropping from heights up to 29 mm were caught reliably. The difference to the static catching method is caused by the small deceleration during the dynamic trap interval in Fig. 3.22. Furthermore, the dynamic trap interval causes the particle to be better positioned inside the trap at the beginning of the static trap interval resulting in a smaller oscillation amplitude.

3.5.6 Conclusion

The experiments with the demonstrator have shown that it is possible to catch objects by means of acoustic forces. Due to the limited control volume, only drop heights of up to 29 mm were possible. In addition, a

closed-loop system would require cameras that send a timestamp with the image or cause a constant delay. For applications where the object moves at low speed through the acoustic pressure field, a closed-loop catcher can also be realized based the control system developed here. This is the case for catching ejected liquid droplets, as described in Chapter 5.

3.6 High-Bandwidth Manipulation

Multiple methods of acoustic manipulations, which can be used for robot grippers, require fast phase adjustments of the piezoelectric transducers. However, the transducers used in this work have not yet been studied in sufficient detail to predict the behaviour during fast phase adjustments. For this reason, a demonstrator was built which can rotate objects with rotational speeds in the kilohertz range and requires a frequent adjustment of the phase of all transducers.

A spherical ring array with a radius of 42 mm and a total of 80 air-coupled ultrasonic acoustic transducers, as shown in Fig. 3.23, was used to examine the transducer behaviour. All transducers feature a main resonance frequency of $f_0 = 40$ kHz and are pointed towards the center of the sphere that coincides with the levitation point of a slightly asymmetric particle. Disc-shaped expanded polystyrene (EPS) particles with a radius $a = 1$ mm and thickness $d = 0.35 \pm 0.1$ mm were used for the measurements presented in this work. The goal was to maximize the acoustic pressure at the levitation point, for which a trade-off between the total number of transducers and their distance from the levitation point exists. The distance between the beamformer of all transducers and the center of the sphere is 37.5 mm. The transducers are arranged on four vertically shifted rings, where each ring consists of 20 transducers. Four transducers each are located at the same azimuth angle, which results a favourable acoustic field distribution for high speed rotation.

The ultrasound transducer model MSO-P1040H07T (cf. [35]) with a diameter of 10 mm is used. It consists of a piezoelectric element that is mounted to a damping mass and a beamformer, as shown in Fig. 3.24a. The combination of the piezoelectric element and the damping mass exhibits a resonance frequency of ≈ 47 kHz. Combined with the beamformer, the transducer has resonance frequencies at ≈ 40 kHz and ≈ 59 kHz, as shown by the impedance measurements in Fig. 3.25. At these frequencies, a low variance in the behaviour of individual transducers can be observed, which is favourable for their application in an array. Further resonances that exhibit a large variance in their frequencies exist above 100 kHz.

Piezoelectric transducers are commonly modelled by a Butterworth-Van-Dyke (BVD) equivalent circuit model, as shown in Fig. 3.24b [86, 100]. The mechanical characteristics are accounted for by the elements denoted with a subscript 0 or 1, while the elements R_p and C_p model

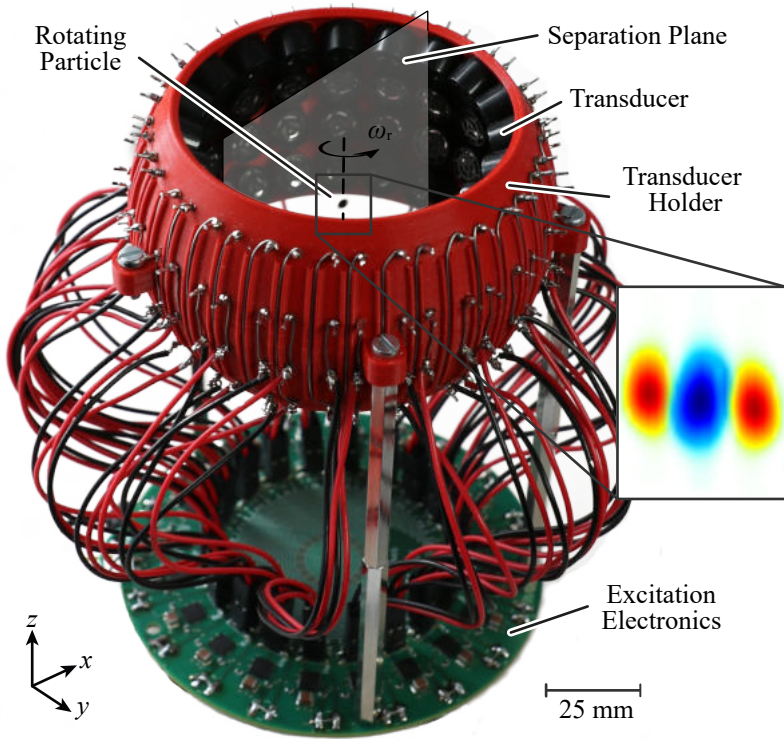


Fig. 3.23: Spherical ring arrangement with 80 transducers and the employed power electronics. The inset qualitatively shows the Gor'kov potential around the levitated particle.

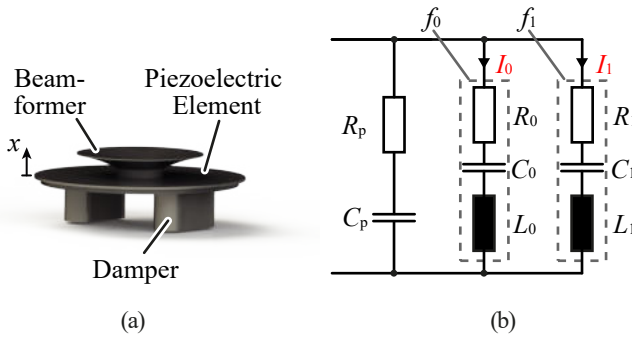


Fig. 3.24: Elements of the employed ultrasonic transducers (a) and Butterworth-Van-Dyke (BVD) equivalent circuit model with two resonances (b). The considered component values are listed in Table 3.1.

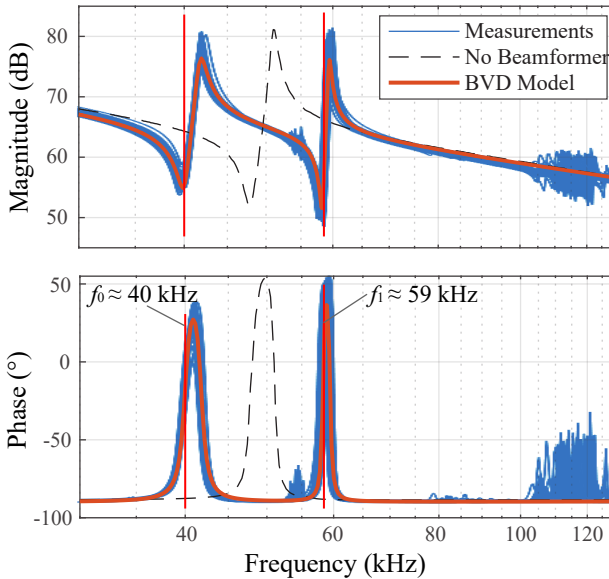


Fig. 3.25: Magnitude (top) and phase (bottom) of impedance measurements of 90 MSO-P1040H07T transducers compared to a fitted multi-resonance BVD model.

Tab. 3.1: BVD Model Parameters.

Component	Value
R_p	5Ω
C_p	1.75 nF
R_0	950Ω
C_0	150 pF
L_0	103 mH
R_1	500Ω
C_1	65 pF
L_1	113 mH

the capacitive electrical behaviour. In most applications, ultrasonic transducers are excited at their main resonance frequency f_0 only. In this case, a single-resonance BVD model (components denoted by a subscript 0 in Fig. 3.24b) is sufficient to model the resulting behaviour. For achieving high rotational frequencies, excitation signals with rapidly changing phase shifts are required that cause the transducer to be excited at additional frequencies. To model the resulting mechanical behaviour of the transducer, a second resonance path, as indicated by the subscript 1 in Fig. 3.24b, that models the second resonance around 59 kHz is required.

The position of the beamformer x_m is proportional to the charge stored in the piezoelectric element and the current i_m is proportional to its velocity v_m

$$x_m - x_0 = \int_0^t v_m dt = c_T \int_0^t i_m dt, \quad (3.48)$$

where x_0 denotes the equilibrium position of the beamformer and c_T denotes a coupling factor between the electrical model and the mechanical behaviour of the transducer.

Acoustic twin traps are used as they have been found to produce high driving torques. The pressure distribution and resulting forces for such a trap generated by the spherical ring array are shown in Fig. 3.26. Square wave voltage signals with a fundamental frequency of $f_0 = 40 \text{ kHz}$ are used to excite the transducers as they can precisely

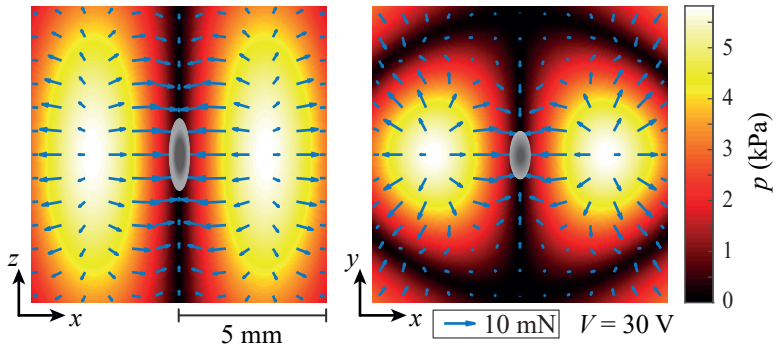


Fig. 3.26: Pressure distribution and forces from top view (right) and side view (left).

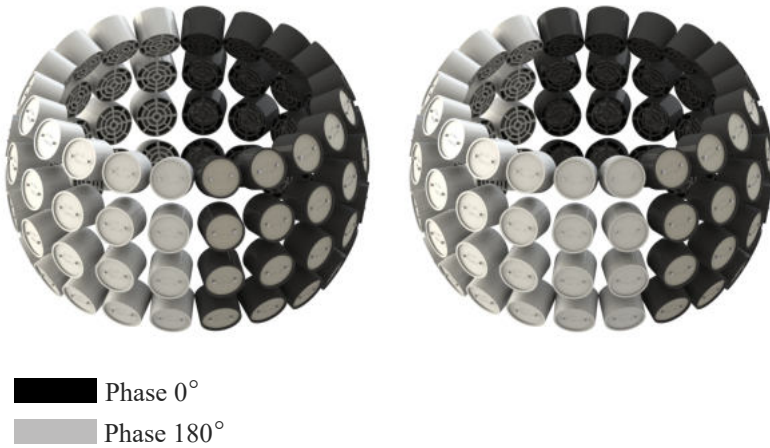


Fig. 3.27: Phase of transducers for rotating the pressure field by 18° .

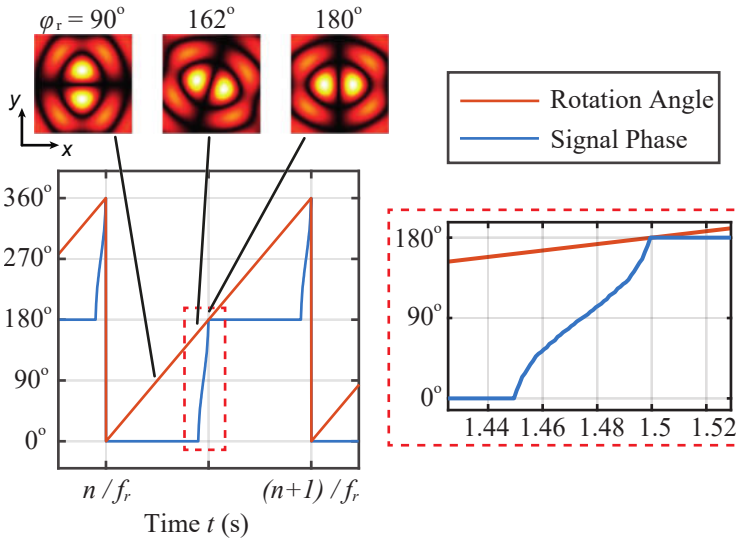


Fig. 3.28: Rotation angle of the particle and phase shift of the employed control concept for a single transducer over one revolution. The pressure fields are visualized for rotational angles φ_r of 90° , 162° , and 180° . The color scale is the same as in Fig. 3.26. The step from 162° to 180° shows the impact of the considered single transducer on the overall pressure distribution, where $\varphi_r = 162^\circ$ corresponds to the point before the phase of the excitation signal is increased. The inset shows a zoomed view of the nonlinear phase increase, where the x -axis labels correspond to the fraction of the considered revolution.

be generated by an FPGA board (Cyclone IV) and a full-bridge power electronic switching circuit. The trap is generated by phase shifting the excitation signals of the transducers on one half of the arrangement by 180° compared to those placed on the other half, as indicated by the plane in Fig. 3.23 and the color separation in Fig. 3.27. A rotation of the particle is achieved by rotating the acoustic field. With the proposed arrangement, the latter can be rotated by 20 discrete steps with an angular resolution of 18° . The phase of the transducers for one of those steps is shown in Fig. 3.27.

To rotate the acoustic field, as exemplary shown for three angles in Fig. 3.28, the phase φ of the excitation signal of each transducer has to be transitioned from 0° to 180° and from 180° to 360° once per revolution

of the particle. To rotate the pressure field by an angle $< 18^\circ$, the aforementioned transition has to be carried out in multiple steps. This is required for a smooth rotation. A nonlinear gradual increase of the phase, as shown in the inset of Fig. 3.28, resulting in a constant rotational speed over one revolution is used. The relation between the phase and the rotation angle was found by calculating the acoustic pressure field using an analytical model based on Eq.(2.1). The number of excitation periods per revolution is $N = f_0/f_r$. One tenth of these periods are used for implementing the phase transitions. For increasing rotational speeds (decreasing N), the interval during which a transducer experiences a phase shift of 180° becomes shorter and additional harmonics are introduced in the excitation signal, resulting in an increased deviation from the desired 40 kHz signal. Particular rotational frequencies exist for which the second resonance of the transducers is excited, resulting in an undesired disturbance of the acoustic field that prevents stable levitation. The capacitive electric behaviour of the transducer yields a decreased impedance at high frequencies, resulting in undesired current harmonics around 120 kHz for high rotational speeds.

The oscillation magnitude of the transducer decreases for increasing rotational frequencies due to the inertia of its moving parts and the decreased amount of time available for the transducer to oscillate with a constant phase before the next phase change is required to rotate the particle. For a given excitation voltage, this decreases the acoustic pressure, the trapping forces, the torque, and the achievable rotational frequency. In order to quantify this effect, we measured the position of the beamformer with a Keyence LK-G5001PV Laser Displacement Sensor for different rotational speeds.

Windage losses result in a drag torque acting on the rotating particle that needs to be counteracted by the driving torque. To model the drag torque, pressure fluctuations due to the acoustic field are neglected in a first approximation. If the rotating particle is approximated by a sphere, the Reynolds number (Re)

$$\text{Re} = \frac{\rho a^2 \omega_r}{\mu}, \quad (3.49)$$

where ρ and μ denote the density of the surrounding fluid (air) and its dynamic viscosity, respectively, is found to be < 6000 for the considered rotational speeds in the kHz range. This corresponds to a laminar boundary layer around the particle that governs the drag torque generation,

while a turbulent flow occurs further away. A model for the drag torque under these flow conditions is provided, e.g., in [101] as

$$T_{\text{drag}} = 186(\rho[\text{kg}/\text{m}^3]\mu[\text{kg}/\text{m} \cdot \text{s}])^{\frac{1}{2}}a^4[\text{m}]\omega_r^{\frac{3}{2}}[\text{rad}/\text{s}]. \quad (3.50)$$

Assuming the air in the spherical volume V_{sphere} , through which the disc rotates, is rotating at the same rotational velocity as the disc, the drag resulting from the two sides of the disc can be neglected and the total drag is reduced compared to Eq.(3.50) due to the decreased disc surface $A_{\text{disc}} = 2\pi ad$ compared to the spherical surface $A_{\text{sphere}} = 4\pi a^2$, where d denotes the thickness of the disc, resulting in

$$T_{\text{drag}} = 186 \frac{A_{\text{disc}}}{A_{\text{sphere}}} (\rho[\text{kg}/\text{m}^3]\mu[\text{kg}/\text{m} \cdot \text{s}])^{\frac{1}{2}} a^4[\text{m}]\omega_r^{\frac{3}{2}}[\text{rad}/\text{s}] \quad (3.51)$$

for a disc shaped object, assuming the air outside of V_{sphere} stands still.

According to [78], the torque on an acoustically levitated object can be calculated as

$$T_{\text{drv}} = \int_{S_0} \mathbf{r}_{\text{CF}} \times \left(\frac{\rho}{2} \langle V^2 \rangle \mathbf{n} - \frac{1}{2\rho c^2} \langle P^2 \rangle \mathbf{n} - \rho(\mathbf{n} \cdot \mathbf{V}) \mathbf{V} \right) d\mathbf{S}, \quad (3.52)$$

where S_0 , \mathbf{r}_{CF} , V , P , and \mathbf{n} denote the surface of the particle, the radius from the centroid of the particle to the point of force application, the particle velocity, the pressure and the normal to the particle surface, respectively.

The drive torque for $\omega_r = 0$ was derived by measuring the oscillation frequency ω_{osc} after an angular step of $\Delta\alpha = 30^\circ$ using a 1000 FPS camera (Sony RX 100 IV) and the OpenCV Python library for image processing [102]. The measurement for an excitation voltage of $V_{\text{ex}} = 7\text{V}$ is shown in Fig. 3.29b.

The torsional spring constant K_T of a disc shaped object with radius a and thickness d is calculated as

$$K_T = \omega_{\text{osc}}^2 \frac{m}{12} (3a^2 + d^2) \quad (3.53)$$

The drive torque depends strongly on the angle between the disc shaped object and the symmetry plane of the twin trap. Hereinafter, this angle is referred to as the lag angle α . During rotation, the lag

angle automatically adjusts, such that the driving torque equals the drag torque. For the maximum rotational speed α reaches the angle α_{\max} , where the maximum driving torque is provided. This angle was determined experimentally to be $\alpha_{\max} \approx 30^\circ$. Since the torsional spring stiffness measurements were taken for a step with $\Delta\alpha = \alpha_{\max}$, the driving torque can be approximated by $T_{\text{drv}} = \alpha K_{\text{T}}$ for $\alpha < \alpha_{\max}$. This method is based on the one published in [78].

A stroboscope (RT Strobe Pocket LED) was used for the verification of the rotational speed. By illuminating the particle with the same frequency as the rotation frequency f_{r} , the particle appears to stand still. Due to the symmetry of the particle, it would appear to stand still for an illumination frequency of $f_{\text{i}} = 2f_{\text{r}}$ as well. To ensure that the particle rotates at f_{i} and not $\frac{f_{\text{i}}}{2}$, an additional measurement with $f_{\text{i},2} = f_{\text{r}} - 1 \text{ Hz}$ was carried out. For $f_{\text{r}} = f_{\text{i}}$, the particle then appears to rotate at 1 Hz, whereas for $f_{\text{r}} = \frac{f_{\text{i}}}{2}$, the particle would appear to rotate at 0.5 Hz.

The measurements of the torsional spring stiffness for different excitation voltages yielded a proportional relation between V_{ex} and the oscillation frequency ω_{osc}

$$\omega_{\text{osc}} = c_{\text{r}} V_{\text{ex}}, \quad (3.54)$$

where $c_{\text{r}} \approx 185.4 \text{ rad}/(\text{Vs})$ as shown in Fig. 3.29. According to Eq.(3.53), this results in a voltage dependent stand still driving torque of

$$T_{\text{drv},0}(V_{\text{ex}}) = \alpha_{\max} c_{\text{r}}^2 V_{\text{ex}}^2 \frac{m}{12} (3a^2 + d^2) \quad (3.55)$$

yielding a driving torque of $2.6 \mu\text{Nm}$ for the maximum excitation voltage amplitude of 37 V . This would result in a maximum rotational speed of about 10.3 kHz according to Eq.(3.51) and assuming $T_{\text{drag}} = T_{\text{drv}}$.

According to the BVD model, the transducers are not capable of switching the phase instantly and the pressure and particle velocity amplitude is reduced during the transition period. This is explained by the mechanical inertia of the piezoelectric element and the beamformer. For high rotational speeds, the transition period lasts for a significant fraction of the total period between two phase shifts and the total acoustic pressure is reduced. The beamformer position for standstill and $f_{\text{r}} = 4 \text{ kHz}$ calculated using the BVD model are shown in Fig. 3.30. For 4 kHz , the excitation of the transducer is reduced approximately five times. Measurements of the beamformer position have confirmed the

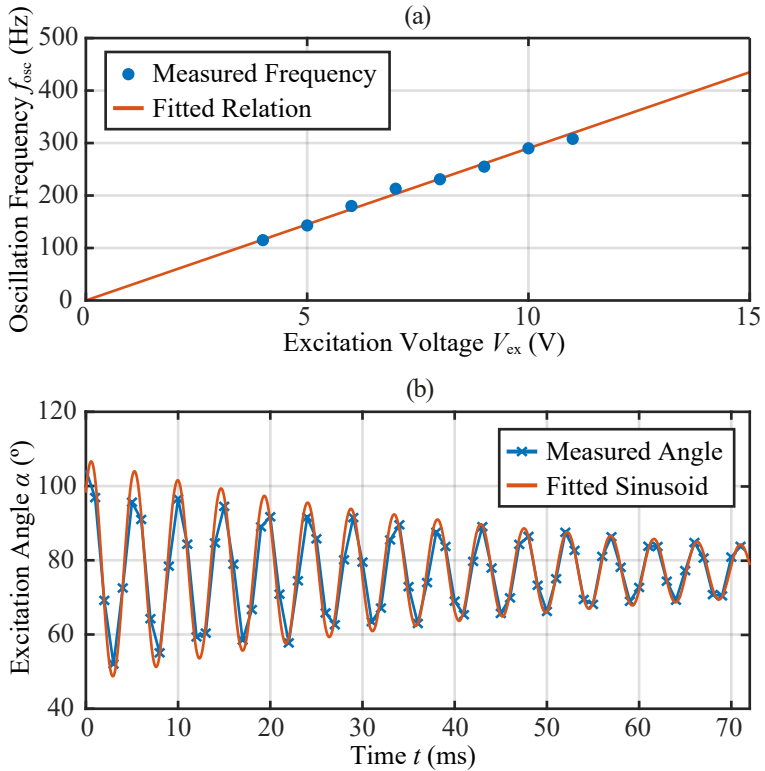


Fig. 3.29: Relation between the excitation voltage V_{ex} and the oscillation frequency f_{osc} measured after an angular step of 30° (a) and the measurement of the excitation angle α for an excitation voltage of 7 V (b).

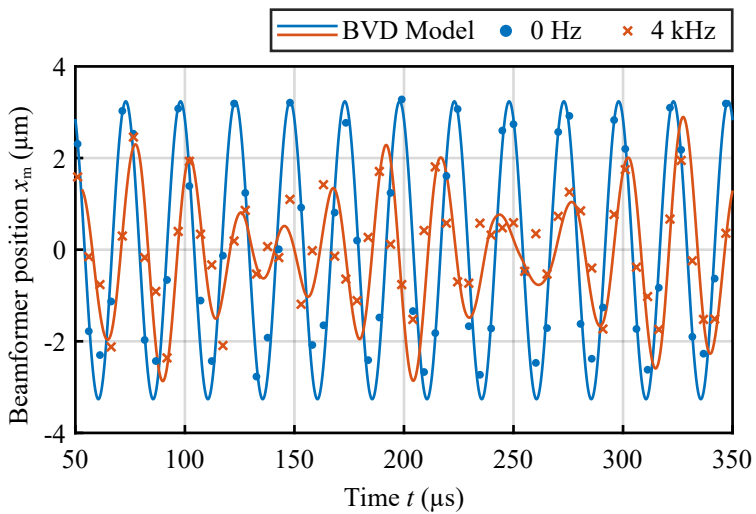


Fig. 3.30: Beamformer positions over time at standstill (0 rpm) and for a rotational speed of 4 kHz (240 krpm) at an excitation voltage of 30 V. The solid lines were obtained from calculations using the BVD model, the markers correspond to measured values.

results obtained from the BVD model as shown in Fig. 3.31. For high rotational speeds, the measurements deviate slightly from the model due to small differences during the transition period. The reduced excitation of the transducers is approximated as

$$E(f_r) = \frac{3}{4 \left(\frac{f_r[\text{Hz}]}{1000 \text{ Hz}} + 1 \right)^2} + \frac{1}{4}, \quad (3.56)$$

as shown in Fig. 3.31. As the driving torque is proportional to the pressure and particle velocity squared (cf. Eq.(3.52)), the driving torque is reduced by

$$T_{\text{drv}}(f_r, V_{\text{ex}}) = E(f_r)^2 T_{\text{drv},0}(V_{\text{ex}}), \quad (3.57)$$

where $T_{\text{drv},0}(V_{\text{ex}})$ and V_{ex} denote the torque at standstill and the excitation voltage, respectively. This decreases the achievable rotational speed for an excitation voltage amplitude of 37 V from 10.3 kHz to 3.2 kHz. The drag torque T_{drag} , driving torque $T_{\text{drv}}(f_r, V_{\text{ex}})$ and measured maximum rotational speed for excitation voltage amplitudes between 8.3 and 37 V are shown in Fig. 3.32. For the calculation of T_{drag} , the air around the disc is assumed to stand still. Due to the rotation of the object, the air around the disc starts to move, which reduces the drag torque. This explains the difference between the drive torque required for the measured rotational speeds and the calculated drag torque shown in Fig. 3.32.

Based on the measurements of the beamformer position, the coupling factor between the charge stored in the transducer and the beamformer position was determined as $c_T = 76.568 \text{ m/As}$ (cf. (3.48)) for the employed MSO-P1040H07T transducers.

The disturbances for rotational speeds where large currents are flowing through resonance paths other than the one at 40 kHz were assessed by analysing the spectrum of the measured beamformer position for rotational frequencies of 500 Hz and 4 kHz. The resulting spectra are shown in Fig. 3.33. For 500 Hz it can be observed that oscillations occur predominantly in the desired region around 40 kHz. However, for $f_r = 4 \text{ kHz}$, additional oscillations occur at the second harmonic around 60 kHz, as well as around 120 kHz. The latter constitutes a parasitic oscillation with a magnitude that exceeds that at lower frequencies and results in unstable levitation. The corresponding current components generate undesired losses and cause heating of the transducers. The excitation of harmonics could be reduced by using sinusoidal signals.

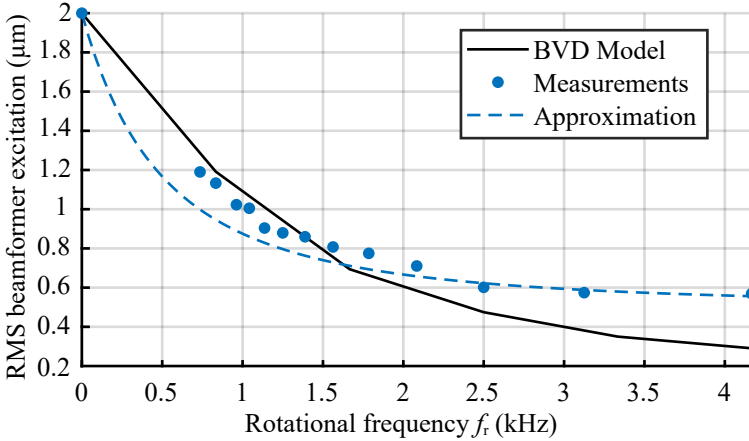


Fig. 3.31: RMS excitation magnitude of the beamformer for various rotational speeds at an excitation voltage of 30 V. The solid line was obtained from calculations using the BVD model, the markers correspond to measured values.

However, such signals are more difficult to generate with switching electronic circuits.

We have demonstrated a maximum rotational speed of an acoustically levitated disc-shaped EPS particle of 216 krpm ($f_r = 3.6$ kHz). This exceeds the highest previously published value [69] by a factor of more than 14 and constitutes the highest rotational speed achieved by an acoustic levitation system, at the time the results were published [92]. Meanwhile, rotational speeds up to 390 krpm were achieved using transfer of orbital angular momentum in acoustic vortices [70].

We have shown that the achievable rotational speed is limited by the decreasing oscillation magnitude due to the narrowband characteristics of the employed piezoelectric transducers and rapid changes of the phase shift of its excitation signals. This limit has not been explored previously but is relevant for other applications, where a temporal superposition of multiple pressure fields is used, such as in [87] for the levitation of objects larger than the acoustic wavelength, in [78] for the stabilization of asymmetric objects trapped in standing acoustic waves, in [103] for acoustophoretic volumetric displays and for ultrasonic haptic devices [88].

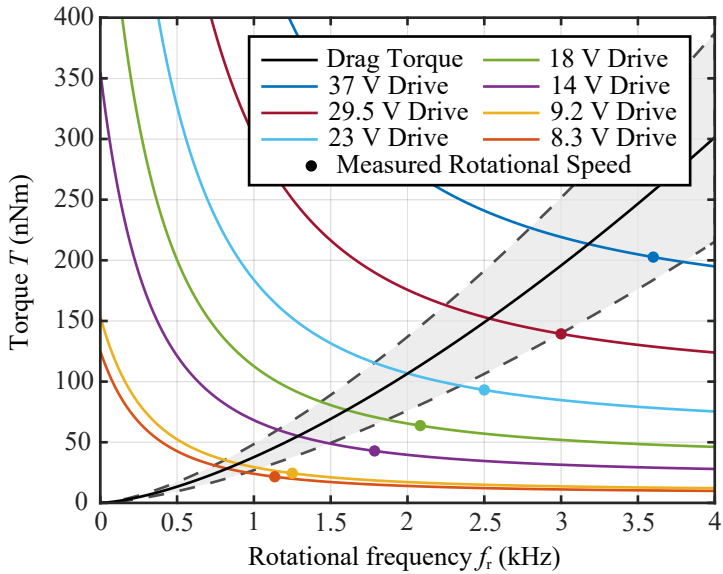


Fig. 3.32: Drag torque, driving torque and measured maximum rotational speed for excitation voltage amplitudes between 8.3 and 37 V. The gray area shows the error area resulting from the uncertainty of the disc thickness, which is between $d = 0.25$ mm and $d = 0.45$ mm.

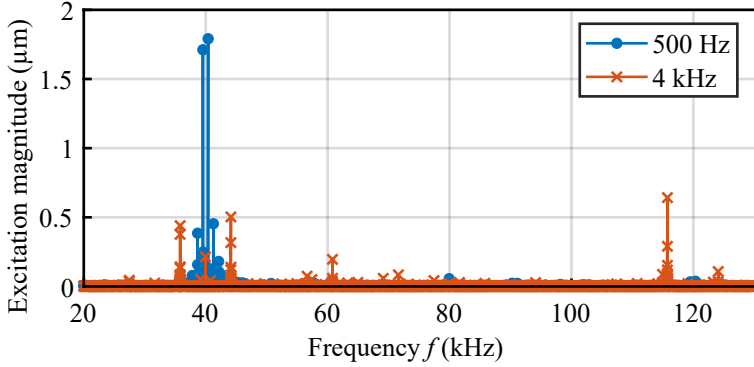


Fig. 3.33: Measured spectrum of the beamformer position for rotational frequencies of 500 Hz and 4 kHz.

Furthermore, we have developed a new control method based on non-linear phase interpolation in order to achieve constant rotational speed.

For rapidly changing phases of the excitation signals, the current and excitation components through resonance paths other than the one at 40 kHz, i.e. particularly second and third harmonics need to be carefully considered. These components can become larger than the one at the fundamental frequency, resulting in unstable levitation and high parasitic losses in the transducers [92].

4

Solid Gripper

Chapter Abstract

Acoustic robot grippers can be used to transport small and fragile objects without damage or contamination. Thereby, they allow the automation of transport processes which are not feasible using other robot grippers. The most challenging part of the transport is the automated picking of objects. If the object to be transported is located on an acoustically transparent surface, a pressure field that could levitate the object without a transparent surface can be used. In realistic applications, however, the object is usually located on an acoustically reflective surface. For those objects the reflections on the surface must be taken into account, which means that new types of acoustic traps and additional components such as reflector plates must be attached to the gripper in order to pick up the object. Using the methods developed during this work, it is possible to transport lightweight objects to and from acoustically reflective surfaces using a single-sided gripper and objects with a density of up to 7 g/cm^3 with a gripper which additionally has a movable reflector. Both the position and the orientation of the object can be manipulated for precise depositing on a target.

4.1 Introduction

During the last decades, more and more industrial manufacturing processes have been automated in order to save costs, but also to increase the quality and quantity of the manufactured products. For this purpose, robots with conventional grippers are often used, which are cost-effective and can be used in a variety of ways. For the transport of fragile objects (e.g. edibles) soft robotics grippers have been developed, which adapt to the shape of the object and minimize the force acting on the object [1–3].

However, these grippers can only be used for the transport of relatively large objects (>1 cm).

Processes involving small and fragile objects are still performed manually. This leads to high production costs and a large number of rejects, which accounts for the large interest in the automation of such processes.

It is possible to use magnetic forces to levitate objects and thus transport them. However, the object to be transported must be ferromagnetic or magnetic. In addition, an active control system is required to ensure the stable levitation of the object.

Acoustic levitation, on the other hand, is passively stable and can be used to levitate any solid object or liquid. However, the acoustic forces are much smaller compared to magnetic forces. To maximize the forces, standing waves are usually used in acoustic levitation systems, which allows the levitation of objects in the nodes, i.e. the pressure minima of the standing wave [27]. The maximum size of the objects is limited to half the wavelength, which is about 4.3 mm for transducers operating at 40 kHz. The levitation of larger objects can be achieved using soft robotic grippers. Therefore, acoustic grippers can be used for processes, which can not be automated otherwise.

The acoustic levitation of objects by means of standing waves has been studied for a long time [27]. Recently, there has been a development from single high-power transducers to arrays of weaker and less expensive transducers [62]. By individually controlling the transducers in these arrays, it has become possible not only to levitate the objects but also to manipulate their position and orientation.

The transportation process using an acoustic gripper consists of three steps. First, the object has to be picked up. This process is usually the most difficult part of the transport, but the difficulty depends on the environment, in which the object is located. Then, using a robot arm, the gripper can be moved to the target of the object before the object can be placed on the target in a controlled manner by manipulating the acoustic pressure field.

4.2 Environment

The environment in which the object is located before the transport has a high influence on the type of robot gripper that can be used. A distinction

is made between whether objects are located on an acoustically reflective or transparent surface.

If the object is located on an acoustically transparent surface, an acoustic trap can be generated around the object neglecting the influence of the transparent surface. The gripper can then be transported with the object levitating in the acoustic trap. It is important to note that the strength of the acoustic trap must be increased slowly, otherwise the object will be ejected if the gripper is not positioned perfectly.

If the object is located on an acoustically reflective surface, as it is the case for most applications, the picking and depositing process is much more complicated. The reflections caused by the surface prevent the use of conventional acoustic traps. Novel methods for picking and depositing objects in such environments are presented hereinafter.

4.3 Acoustic Levitation in Reflective Environments

To generate a pressure distribution that facilitates levitation of an object in free space, the phase for each transducer of an array has to be chosen such that the pressures generated by the individual transducers constructively superimpose at a focal point corresponding to the desired levitation position. This is achieved by calculating the phases of the individual excitation signals as

$$\varphi = -\angle \left(\frac{P_0}{d_d} e^{i \frac{2\pi f d_d}{c_0}} + R \frac{P_0}{d_r} e^{i \frac{2\pi f d_r}{c_0}} \right), \quad (4.1)$$

where the reflection coefficient of an acoustically transparent surface in the acoustic field is $R = 0$ [62]. The factor $P_0 = 0.26 \text{ Pa} \cdot \text{m} / \text{V}_{\text{RMS}}[\text{V}]$ for the transducers used in this work [35]. Further, d_d and d_r denote the distance between the transducer and the focal point for the direct and reflected acoustic wave (see Fig. 4.1), respectively. An acoustic trap is then created by adding a phase signature, depending on the type of trap, to the phases that are used to generate the focal point [62, 87]. In this work, mainly twin traps and standing waves are used to levitate objects. Twin traps are generated by applying a phase shift of 180° to one half of the transducers in the array. Separating the transducers of the array by a horizontal plane results in a trap subsequently referred to

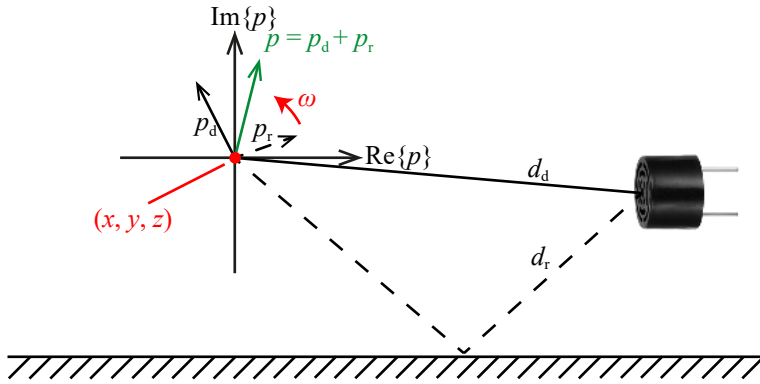


Fig. 4.1: Direct (solid line) and reflected (dashed line) pressure components for a single transducer that are superimposed depending on the relative position of the transducer with respect to the reflecting surface, and total pressure generated by the transducer (green).

as a horizontal twin trap (HTT). Separating the two halves by a vertical plane accordingly results in a vertical twin trap (VTT) [89, 104].

If an acoustically reflective surface is present within the acoustic field, the pressure generated by a single transducer at a point contains an additional component caused by the reflected wave ($R \neq 0$) [105, 106]. The total pressure oscillation has the same frequency as the pressure oscillation without the reflection, but the phase and magnitude are different. This can be illustrated by means of a pointer diagram as shown in Figure 4.1. If the direct pressure component p_d is constructively superimposed with the reflected pressure component p_r , a higher pressure amplitude is achieved. Due to the change in phase, the control must be adjusted according to Eq.(4.1) with R set to the appropriate value. If the transducer arrangement is shifted relative to the reflecting surface, the influence of the reflected wave on the phase of p changes, which has to be taken into account by the control. The phase signatures for the trap generation are the same as for the case without reflective surface.

Using the reflection of sound waves on a surface, a standing wave can be formed between the transducers and the surface by focusing the acoustic pressure on the surface. The distance between the oscillating

elements of the transducers and the reflecting surface should be a multiple of $\lambda/2$ to achieve a high resulting pressure [60, 85].

4.4 Distribution of the Maximum Attainable Pressure

A distribution of the maximum attainable pressure (DMAP) describes the distribution that assumes a constructive superposition of all acoustic pressure sources at each point in space. It is calculated for each point by

$$M(x, y, z) = \sum_j \left| V_{\text{RMS}}[V] P_0 \left(\frac{J_0(kr \sin \theta_{d,j})}{d_{d,j}} + R \frac{J_0(kr \sin \theta_{r,j})}{d_{r,j}} \right) \right|, \quad (4.2)$$

where $\theta_{d,j}$, $\theta_{r,j}$, $d_{d,j}$ and $d_{r,j}$ denote the beam angle of the direct path, the beam angle of the reflected path, the distance of the direct path between the considered point in space (x, y, z) and the transducer, and the distance of the reflected path between (x, y, z) and the transducer for the j^{th} transducer, respectively. In environments without reflective surfaces, the DMAP is approximately constant, i.e. the attainable pressure is approximately the same at each point inside the array of transducers, as shown in Figure 4.2a. This means that it is possible to focus the pressure at each point. For reflective environments, the DMAP becomes relevant since regions can be found where it is not possible to generate an acoustic trap because the maximum achievable pressure is too low.

4.5 Grippers

The transport of small objects from and to acoustically reflective surfaces can be carried out by two types of grippers:

- Single-sided grippers with vertically and horizontally oriented transducers. The methods are verified with a cylindrical single-sided array. Three rings of 6, 12, and 18 vertically oriented transducers are located at the horizontal top face of the arrangement and three rings of 20 horizontally oriented transducers each are located on the side walls of the cylinder.

- Reflector grippers with vertically or quasi vertically oriented transducers and a reflector plate that can be moved relative to the transducers. A spherical cap array of transducers consisting of three rings with 6, 12, and 18 transducers is used for the verification of the methods. Depending on the application, a moveable array of opposing transducers is added.

The transducers are controlled by an FPGA board generating 96 and 36 (72) logic square wave signals for the single-sided gripper and the reflector gripper, respectively. Resolutions of 0.5° and $\approx 1\%$ are achieved for the phase and duty cycle, respectively. The logic signals are then amplified by gate driver ICs (IX4428) and applied to the transducers. The duty cycle and the phase are calculated on a PC for each transducer and transmitted to the FPGA board via a UART interface.

4.6 Transport with the Single-Sided Gripper

Compared to picking an object from an acoustically transparent surface, it is more difficult to pick objects from acoustically reflective surfaces. The reflection of incident waves p_i on a reflective surface does not cause a phase shift. If the incident wave arrives perpendicular to the surface, the superposition between the incident wave p_i and the reflected wave p_r causes a pressure minimum to be formed at a distance of $\lambda/4$ from the surface as shown by Eqs.(4.3 - 4.5) [60, 85].

$$p_i(t, z) = A \sin \left(\omega t - 2\pi \frac{z}{\lambda} \right), \quad (4.3)$$

$$p_r(t, z) = A \sin \left(\omega t + 2\pi \frac{z}{\lambda} \right), \quad (4.4)$$

$$p_i(t, \lambda/4) + p_r(t, \lambda/4) = A \sin(\omega t - \pi/2) + A \sin(\omega t + \pi/2) = 0. \quad (4.5)$$

If the acoustic sources are located far away from the surface, the acoustic waves are perpendicularly incident upon the surface. The DMAP for transducers on the horizontal top of the single-sided arrangement, which are located at a distance of 3.5λ from the reflective surface, is shown in Figure 4.2b. Due to the pressure minimum being formed at $z = \lambda/4$ above the reflective surface, it is impossible to focus the

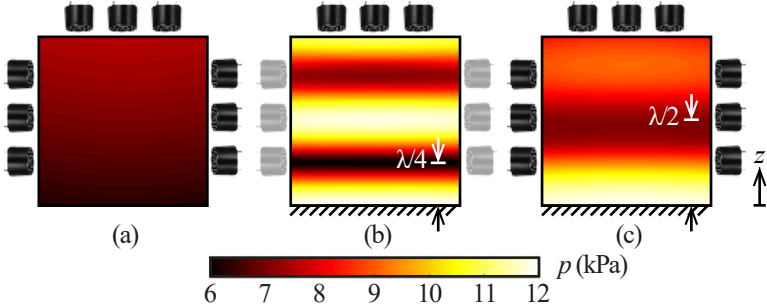


Fig. 4.2: DMAP for (a) a single-sided array in free space, (b) the top part of the single-sided array with an acoustically reflective surface ($R = 1$) at $z = 0$ exhibiting high gradients that prohibit the generation of arbitrary focal points and (c) the single-sided arrangement with an acoustically reflective surface at $z = 0$ with a gradient that allows manipulation above a height of $z = \lambda/4$.

pressure around this location, which would be necessary to generate a twin trap.

If the transducers are located closer to the surface, the distance at which destructive superposition occurs deviates from $\lambda/4$ and the minimum of the DMAP is attenuated. This is shown for the single-sided arrangement in Figure 4.2c. With this arrangement it is possible to focus the pressure for $z \geq \lambda/2$. Therefore, a VTT can be generated at $z = \lambda/2$ as shown in Figure 4.3b. The forces generated by this trap pull the object into the acoustic trap, if the vertical force generated by this trap is larger than the gravitational force. This is the case at $z = \lambda/4$ for all objects that can be lifted with this arrangement, as shown in Figure 4.4.

By forming a standing wave between the transducers and the reflective surface it is possible to levitate objects in a stable manner at $z \approx \lambda/4$, however, without the possibility to move the object vertically due to the minimum of the DMAP at $z \approx \lambda/4$. Nevertheless, it is possible to switch from a standing wave to a VTT located at $z = \lambda/2$ that pulls the object upwards. Taking the reflections at the surface into account, the control can be adjusted such that the object is moved away from the surface until reflections become negligible and the array can be moved away from the surface without further adjustments of the control. An array for this process requires vertically oriented transducers

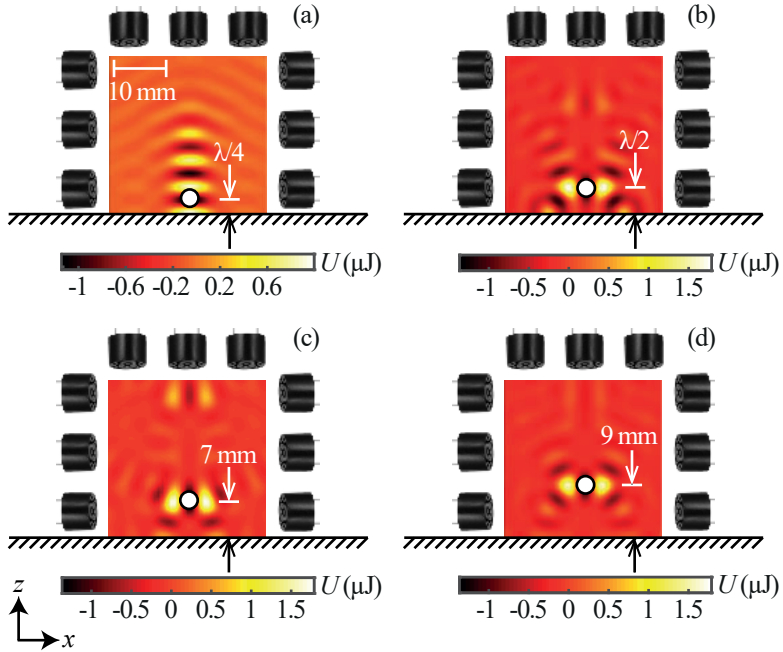


Fig. 4.3: Force potential for (a) a standing wave with a minimum at $z = \lambda/4$, and VTTs at (b) $z = \lambda/2$, (c) $z = 7$ mm and (d) $z = 9$ mm. The potentials are obtained for an acoustically reflective surface ($R = 1$) at $z = 0$.

to generate a standing wave and horizontally oriented transducers to generate a VTT. The resulting forces and force potentials during the process are shown in Figures 4.3 and 4.4 for the single-sided array.

To perform the picking process in a continuous fashion, the power of the vertically oriented transducers is first increased continuously, lifting the object smoothly to $z = \lambda/4$. Subsequently, using stepwise phase changes, the standing wave is altered to a VTT. Finally, by using small steps to shift the location of the trap in the vertical direction, the object is moved further away from the surface while the stress on the object is minimized [89].

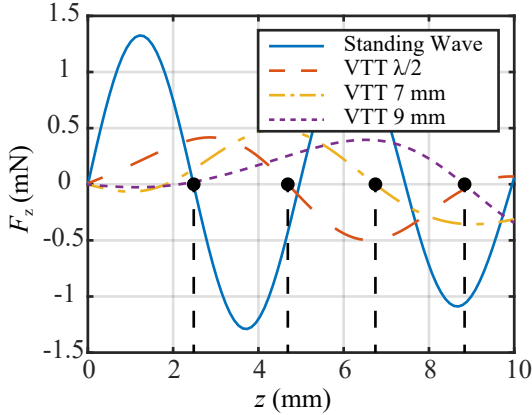


Fig. 4.4: Vertical forces for a standing wave with a minimum at $z = \lambda/4$, and VTTs at $z = \lambda/2$, $z = 7$ mm, and $z = 9$ mm. The forces are obtained for an acoustically reflective surface ($R = 1$) at $z = 0$.

4.7 Transport with the Reflector Gripper

As shown in Figure 4.4 for the single-sided gripper and acoustically reflective surfaces, the forces resulting from standing acoustic waves, which are formed between the transducers and an acoustically reflective surface, are significantly larger compared to the forces resulting from VTTs. The weak vertical forces resulting from VTTs limit the density of the objects that can be lifted. It is not possible to move an object located at the pressure minimum formed at $\lambda/4$ above a reflective surface in the vertical direction without using VTTs.

By inserting a thin and moveable reflector directly above a reflective surface, an object levitating in the lowest pressure minimum of a standing acoustic wave at $z = \lambda/4$, as shown in Figure 4.5a, is moved upwards by the thickness of the reflector, as shown in Figure 4.5b. Afterwards, the entire gripper including the reflector can be moved away from the surface and the object levitates at $\lambda/4$ above the reflector in a standing wave formed between the transducers and the reflector, as illustrated in Figure 4.5c. However, this is only possible, if the surroundings of the gripped object allow the required movement of the reflector. All arrangements of transducers that are capable of forming a standing wave

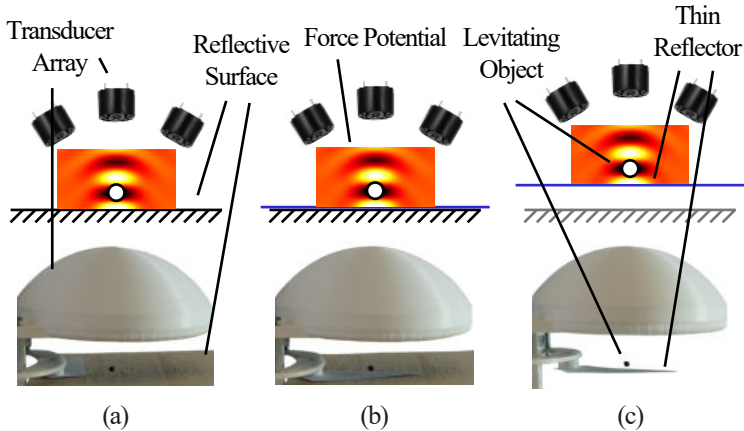


Fig. 4.5: Gripping process of an object located on an acoustically reflective surface using a thin reflector. (a) A standing wave between the transducer arrangement and an acoustically reflective surface is formed which traps the object at the first pressure minimum of the standing wave. (b) A thin reflector is inserted directly above the reflective surface, and (c) the arrangement, the reflector and the levitating object can be moved away from the reflective surface.

can be used to grip objects from acoustically reflective surfaces using this method. It is possible to grip objects from reflective surfaces with a significantly larger density compared to the method that uses VTTs. Gripping of a plastic sphere with a radius of $a = 1$ mm and a density of $\rho = 1$ g/cm³ has been demonstrated using the gripper shown in Fig. 4.5. The maximum density is about four times larger compared to the maximum density achievable with the method using VTTs.

A thin reflector can also be used to achieve a distance between the levitating object and the reflective surface that is larger than $\lambda/4$. After the thin reflector is inserted below the levitating object, as shown in Figure 4.6b, it can be moved vertically until the levitating object reaches the levitation height of the second pressure minimum of a standing wave formed between the transducer arrangement and the reflective surface, as shown in Figure 4.6c. Afterwards, by removing the reflector, the distance between the object and the reflective surface is increased to

$z \approx 3\lambda/4$. This is shown in Figure 4.6d. By reinserting the thin reflector directly above the reflective surface, the gripper and the thin reflector can be moved away with a distance $> \lambda/4$ between the reflector and the levitating object. The same procedure is possible for all levitation heights at which a pressure minimum is formed between the transducer arrangement and the reflective surface. An arrangement of transducers that can form a standing wave containing more than one stable levitation point is required. If the reflector arrangement used in this work is positioned such that the focus point of the transducers is located at the distance of the reflective surface, only two stable levitation positions exist, as shown in Figure 4.5. To form additional stable levitation points, the distance between the arrangement and the reflective surface has to be increased.

A similar method can be used to grip multiple objects simultaneously. By forming a standing wave between the gripper and the reflective surface, inserting a thin reflector, moving the thin reflector vertically until the levitated object reaches the height of the second pressure minimum of the standing wave formed between the transducers and the reflective surface, and removing the thin reflector, the first object is levitated at $\approx 3\lambda/4$ above the reflective surface as shown in Figure 4.6a-d. A second object can be trapped in the lowest pressure minimum by moving the gripper to an object located on the reflective surface. This process can be repeated in order to insert more objects into the gripper. The maximum number of objects that can be gripped depends on the transducer arrangement. The bigger the distance from the gripper to the reflective surface, the more objects can be gripped, but the increased distance reduces the trapping forces and, therefore, the maximum density of the gripped objects. Furthermore, the levitating objects influence the pressure field and may cause unstable traps.

This method can also be used to insert objects from acoustically reflective surfaces into double-sided arrangements. For this purpose, the reflector gripper can be used to generate a standing acoustic wave between the transducers and the reflective surface. The object located on the reflective surface is then lifted to a levitation height of $z = \lambda/4$ as shown in Figure 4.7a. After the thin reflector is inserted just above the reflective surface and the gripper including the reflector are moved away from the reflective surface, a second array of opposing transducers is added to the gripper, as shown in Figure 4.7b. Then the reflector can be removed while a HTT is generated at $z = \lambda/4$ as shown in

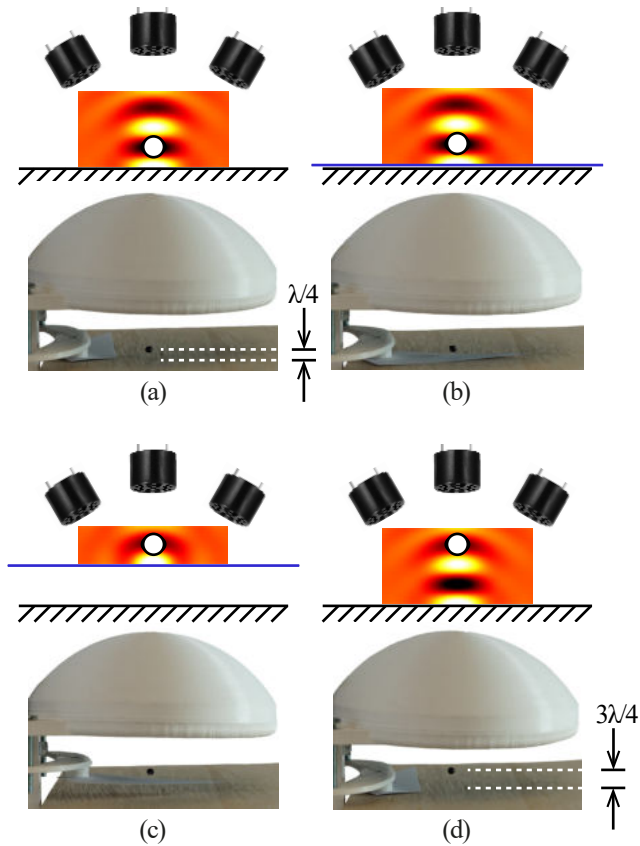


Fig. 4.6: Process of lifting an object located at the lowest pressure minimum in a standing acoustic wave. (a) A standing wave between the transducer arrangement and an acoustically reflective surface is formed. The object is trapped in the lowest pressure minimum of the standing wave. (b) A thin reflector is inserted directly above the reflective surface. (c) The reflector is moved upwards until the levitating object reaches the levitation height of the second pressure minimum of the standing wave between the transducers and the reflective surface, and (d) the reflector is removed and the object is located at the second pressure minimum. The shown elements correspond to those annotated in Figure 4.5.

Figure 4.7c. A levitation point of $z = \lambda/4$ is achieved by exciting all transducers with the same phase. Finally, the HTT is moved to the center of the double-sided arrangement in order to trap the object as stable as possible (Figure 4.7d). This movement can be achieved by applying a phase shift between the two halves of the gripper, which is increased in small steps from 0° to 180° [89].

4.8 Orientation Control with the Reflector Gripper

Due to the symmetry of the pressure field using standing waves between the transducers and the reflector, the object levitating in the gripper has the tendency to spin around the symmetry axis of the gripper and is therefore not in a controlled state [36, 76, 77, 107]. Therefore, a method for the contact-less transport of objects in a controlled state was developed.

It has been shown, that the superposition of pressure fields and force potentials generated by transducers operating at different frequencies can be calculated separately and added up to get the total pressure field and force potential [92, 93]. This method was used for this gripper in order to generate a stabilizing torque, which stops the spin of levitating asymmetric objects. The torque can be adjusted such that the orientation of the levitating object can not only be stabilized but also controlled. Therefore, it is possible to position the object on a target surface in a precise manner, which is required for most micro manufacturing processes that can be automated using ultrasonic grippers.

The developed gripper uses piezoelectric transducers operating at 40 kHz and 25 kHz. The 40 kHz transducers are used to counteract the gravitational force. This is achieved by arranging them on a spherical cap with a radius of $r = 42$ mm and operating all transducers at the same phase. If an acoustically reflective surface is placed near the focus point of the arrangement, a standing wave between the gripper and the reflective surface is formed, as shown in Fig. 4.8b. Objects located on the reflective surface can be picked up using this method, since they are pushed towards the first pressure minimum, which is about a quarter of a wavelength ($\frac{\lambda}{4} \approx 2.15$ mm) above the surface.

When the object is levitating in this pressure minimum, a thin reflector plate can be moved under the levitating object, resulting in a

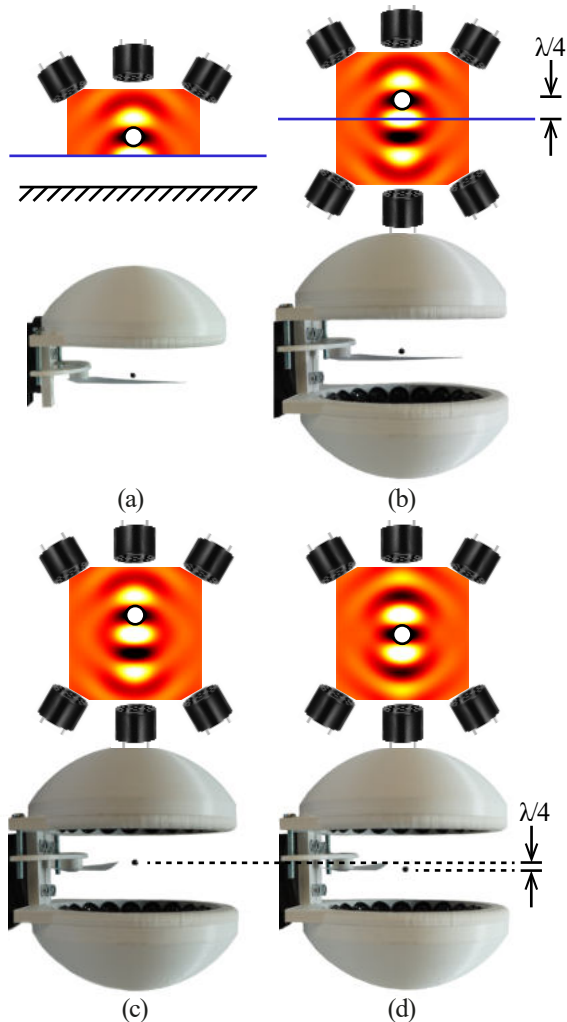


Fig. 4.7: Insertion process of an object located on a acoustically reflective surface into a double-sided acoustic gripper. (a) The arrangement, the inserted reflector, and the levitating object are moved away from the reflective surface. (b) The second half of the double-sided arrangement is moved to the other side of the inserted reflector and the double-sided gripper is controlled such that a HTT is generated at $z = \lambda/4$. (c) The reflector can be removed, and (d) the trap is moved to the center of the double-sided gripper. The shown elements correspond to those annotated in Figure 4.5.

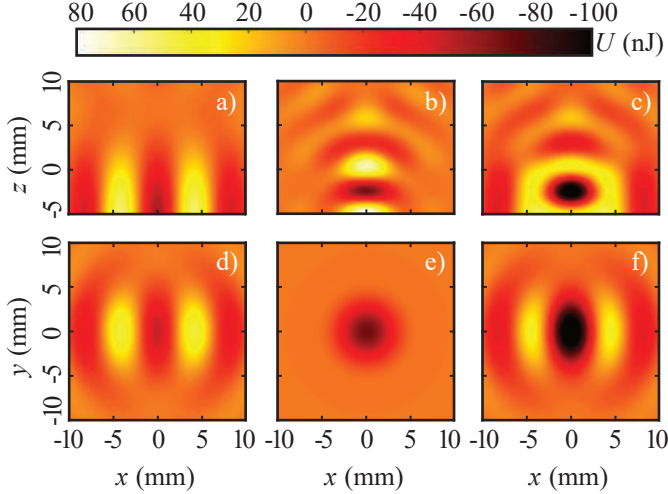


Fig. 4.8: Side and top view of the Gor'kov potential resulting from the transducers operating at (a), (d) 25 kHz, (b), (e) 40 kHz and (c), (f) the combination of both. The focus point of the gripper is at $x, y, z = 0$ mm and the a reflective surface is located at $z = -5$ mm. The asymmetry of the pressure field shown in (f) is required for stabilizing the orientation of the levitating object. The potentials in (a), (b), and (c) are shown for $y = 0$ mm and the potentials in (d), (e), and (f) are shown for $z = 2.15$ mm.

standing wave between the transducers and the reflector plate. The 3D printed reflector plate with a thickness of $t = 0.8$ mm is placed 5 mm below the focus point of the gripper in order to have enough space for the 25 kHz transducers. A slope was added to the edges of the plate to reduce disturbances of the pressure field during the movement of the reflector plate. The gripper (including the reflector plate) can then be moved away from the reflective surface while maintaining stable levitation [89, 108].

A ring shaped arrangement ($r = 53$ mm) of transducers operating at 25 kHz is used to superimpose an asymmetric pressure field, that provides a stabilizing torque and stops the aforementioned spin. Due to the connection to the robot arm, the transducers were only arranged on two sides of the gripper and not in a full circle. A uniform distribution of the transducers on the ring-shaped array could be achieved by an

adjusted connection to the robot arm. However, since the orientation can be controlled with the used arrangement, this is not required. The gripper including the reflector plate is shown in Fig. 4.9. The resulting asymmetric Gor'kov potential, the 40 kHz Gor'kov potential and the 25 kHz Gor'kov potential are shown in Fig. 4.8.

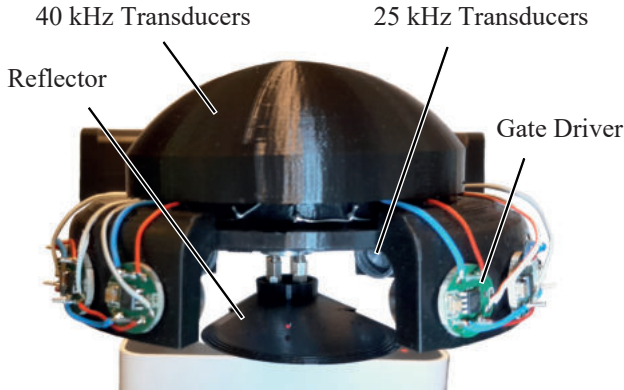


Fig. 4.9: The reflector gripper used to verify the presented methods.

By adjusting the phase shifts of the 25 kHz transducers individually, it is possible to rotate the 25 kHz pressure field and therefore the object around the z -axis. For the initial position, a phase shift of 180° between the two halves of the 25 kHz arrangement is applied. By adjusting which transducers are operating at 0° and 180° phase, the pressure field can be rotated as illustrated in Fig. 4.12. For smoother rotation, the phase shift of the transducers can be increased gradually from 0° to 180° and vice versa.

For placing the object on a target on a reflective surface, the same method as for the picking process can be used. The gripper can be moved to the target surface, such that the reflector is very close to the surface. By removing the reflector and reducing the acoustic power afterwards, the object can be placed on the target while still maintaining the controlled orientation.

The gripper is mounted on a robot arm to allow long distance movement of the objects. The arm and the stepper motor, which is used to move the reflector plate, are controlled by a Raspberry Pi, which also

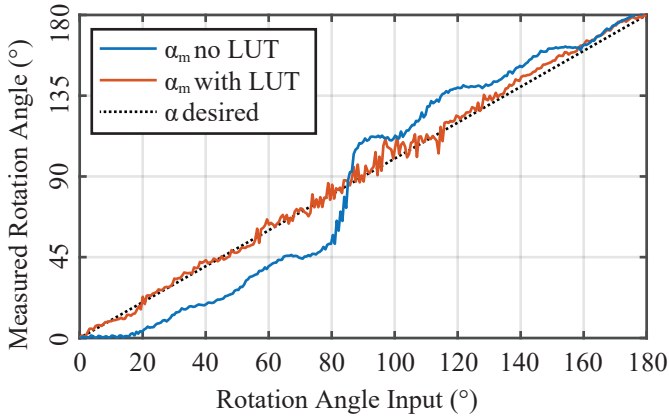


Fig. 4.10: Measured rotation angle α_m for 10 V and 8 V excitation voltage amplitudes for the transducers operating at 40 kHz and 25 kHz, respectively. The blue line shows the trajectory using the simple phase calculating method and the red line uses a look-up table (LUT) measured for this combination of excitation voltages.

calculates the required phase shifts and duty cycles for the transducers and forwards them to a Cyclone IV FPGA board. The FPGA generates one signal for each transducer operating at 25 kHz, which is inverted and amplified by one gate driver IC (IX4428) per transducer. This is required for individually controlling the phase shifts of the transducers and allowing the rotation of the levitating object. Additionally, two signals for the transducers operating at 40 kHz are generated on the FPGA and are amplified by an L298N dual H-bridge board. An overview of the system is shown in Fig. 4.11.

The methods presented in this work facilitate the reliable transport of small and fragile objects located on acoustically reflective surfaces, if the gripper is positioned precisely above the object. For objects with high density ($\rho \geq 1 \text{ g/cm}^3$), some oscillations occur during the picking process. The added slopes to the edges of the reflector plate reduce the disturbances of the pressure field during the movement of the reflector plate significantly and improve the stability during the picking process. Objects with a maximum density of $\rho = 7.3 \text{ g/cm}^3$ were picked up using this gripper. The higher density compared to the gripper shown in Fig. 4.5 is explained by the improved stability of the reflector.

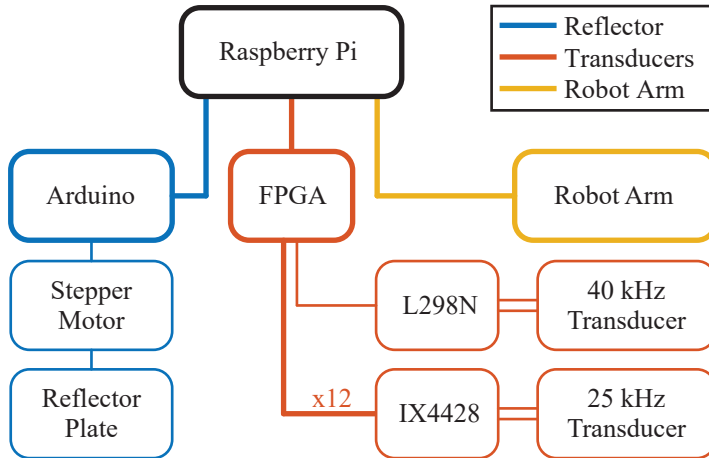


Fig. 4.11: Overview of the components used to control the gripper. The robot arm and the stepper motor, which is used to move the reflector plate, are controlled by a Raspberry Pi, which also calculates the required phase shifts and duty cycles for the transducers and forwards them to a Cyclone IV FPGA board. The FPGA generates one signal for each transducer operating at 25 kHz, which is inverted and amplified by one gate driver IC per transducer (IX4428). Additionally, two signals for the transducers operating at 40 kHz are generated on the FPGA and are amplified by an L298N dual H-bridge board.

The stabilization of asymmetric objects with piezoelectric transducers operating at 25 kHz requires a suitable choice of operating voltages. If the operating voltage is chosen too low, the stabilizing torque is too weak to stop the rotation of the particle. However, for very high operating voltage, the particle tilts around the horizontal axis with the lowest stiffness or even starts to wobble around this axis, when the horizontal and vertical forces are of similar strength. The operating voltages, which yielded the best stability during our experiments are shown in Tab. 4.1. With suitable operating voltages, the object can be kept in a stable position even during the movement of the robot arm, which can cause vibrations of the gripper.

The best stability is achieved if the orientation angle α of the object is not changed before arriving at the target location since the initial

Tab. 4.1: Best suited operating voltages (RMS) for the transducers operating at 25 kHz and 40 kHz and for different levitated object materials.

Material	40 kHz Voltage	25 kHz Voltage
Styrofoam	10 V	8 V
PLA	19 V	16.5 V
Tin	25 V	20 V

orientation ($\alpha = 0^\circ$) is the most stable as shown in Fig. 4.12. The simplest approach for calculating the phase shifts for the transducers operating at 25 kHz is

$$\varphi_j = \begin{cases} 180^\circ & \alpha_j > 210^\circ \\ 6(\alpha_j - 180^\circ) & 180^\circ < \alpha_j \leq 210^\circ \\ 0^\circ & 30^\circ < \alpha_j \leq 180^\circ \\ 6\alpha_j + 180^\circ & \text{otherwise} \end{cases} \quad (4.6)$$

where $\alpha_j = \alpha + j \cdot 30^\circ$ is the rotation angle relative to the j -th transducer, assuming uniformly distributed transducers. This approach results in smooth phase shift changes for each transducer. As shown in Fig. 4.10, there is a deviation between the measured orientation angle α_m and the input angle α . Two kinds of deviations occur during a revolution. First, the non-uniform distribution of the transducers causes a slower rotation for the largest part of the revolution and a faster rotation for rotation angles around 90° . Furthermore, the linear phase shift change of each transducer from 0° to 180° results in a non-linear orientation angle change during each 30° rotation interval. Both kinds of deviation can be compensated for by a look-up table (LUT) for fixed operating voltages as shown in Fig. 4.10. The look-up table was generated using video footage and OpenCV image processing algorithms for the rotation angle detection. For slight deviations of operating voltages, which are often required for objects of different shape, the look-up table can still be used with small orientation inaccuracy. For objects of different materials, the operating voltages differ too much from the ones used for the look-up table and relatively large inaccuracies can occur. Therefore, it is recommended to use an individual look-up table for each material.

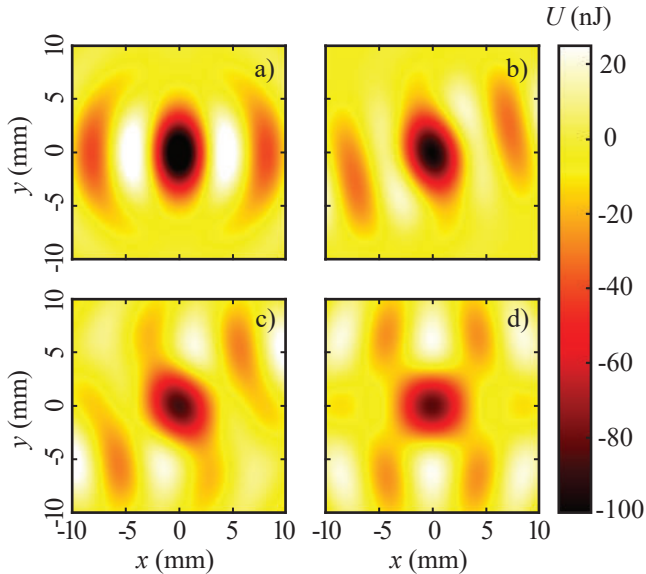


Fig. 4.12: Top view of the Gor'kov potential for rotation angles of (a) 0° , (b) 30° , (c) 45° and (d) 90° .

This work presents the first ultrasonic robot gripper, which allows the contact-less transport of small and fragile objects in a controlled manner. Its capability of controlling the orientation of levitating objects is required for applications in micro-manufacturing processes. With the presented methods, high positioning and orientation accuracy can be achieved. Oscillations during the picking process and the movement of the robotic arm limit the stability and reliability of the transport and should therefore be further reduced in future research. There is still potential for improvements in gripper design, since this work has focused on picking methods rather than gripper optimization. If very high positioning accuracy is required, the system can be extended with a closed-loop control system using the image processing algorithms used for the look-up table generation [108].

5

Liquid Gripper

Chapter Abstract

Acoustic droplet ejection (ADE) is a method used to transfer live cells, proteins and other sensitive substances from a source well to a receiving plate in a gentle manner. It is used to eject droplets in the nano and pico litre range, which are then caught by a target substrate. During this work, a novel acoustic droplet ejection method, which creates an air cavity in the liquid source was developed. During the collapse of this cavity, a Worthington jet is formed and a droplet in the micro litre range is ejected from the tip of the jet to a height up to 10 cm. The droplet can then be caught by an acoustic liquid levitator. This device reduces the complexity, the volume and the cost and does not require a contact-based solution for the catching of the droplet compared to current ADE methods. It facilitates the use of contact-less acoustic transportation methods for applications, for which this technology was previously not profitable.

5.1 Introduction

The possibility of levitating liquid droplets in standing waves by means of acoustic radiation forces has been known since 1933 [27]. In the meantime, methods have been developed, which allow the manipulation of the position and the merging of multiple droplets during levitation using acoustic forces [109]. For these methods, the droplets are inserted manually into the acoustic field with a pipette or syringe, or a nozzle is used to automatically create a droplet [5, 110–114].

Acoustic droplet ejection (ADE) is a non-contact method for droplet generation without the restriction of a nozzle [5, 115–117]. Ultrasonic

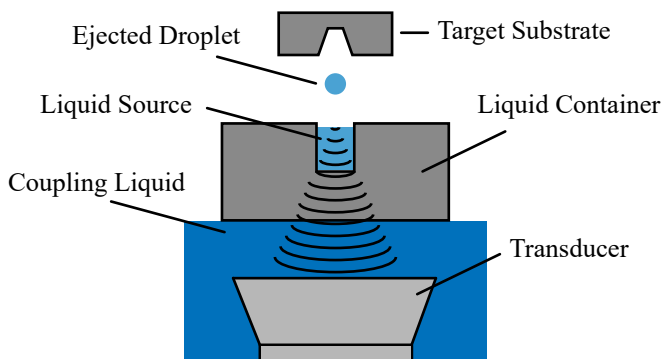


Fig. 5.1: Illustration of the currently used ADE method. An ultrasonic pulse is generated by a transducer and focused through a coupling liquid, the liquid container and the liquid source on the surface of the liquid, such that a droplet in the pico or nano litre range is ejected. The droplet is then caught by a target substrate, which is placed above the liquid source.

pulses are used to eject small amounts of liquids in the nano or pico litre range. The pulses are generated by piezoelectric transducers, which are submerged in the liquid or coupled to the liquid via the source well container and a coupling liquid (water). The ultrasonic waves travel through the liquid to be ejected and are focussed on its surface resulting in the ejection of a small droplet. The ejected droplets are caught by a target substrate that is placed above the liquid container. This system is illustrated in Fig. 5.1.

ADE is currently used for drug discovery [118–120], compound management [121–123], genomics [124, 125], synthetic biology [126–128], proteomics [129–131], and personalized medicine [5, 132, 133]. Such systems are capable of ejecting 200 - 500 droplets per second with a coefficient of variation $CV < 4\%$ [134].

Contact-based droplet ejection methods can be used to eject droplets with adjustable volume and ejection height. They generate Worthington jets, which can be observed when a solid object or a liquid droplet is dropped into a liquid container. In the process, an air cavity is formed in the liquid. During the collapse of the cavity, the liquid fronts move towards the center of the cavity and the kinetic energy of the moving liquid and the lack of space inside the cavity cause a part of the liquid

to be pushed upwards resulting in the formation of a jet. If certain conditions are met, a droplet is formed at the tip of the jet, which is ejected to heights up to a few centimeters. This process is examined in detail in [79, 80, 135–137]. The same principle applies for granular jets generated by underground cavity collapses [138].

The aim of this work is the development of a contact-less transportation method for liquid droplets, which does not require mechanical contact for catching the droplet to prevent contamination. For this purpose, a method was developed that generates an air cavity in a liquid source by means of an ultrasonic pulse instead of a solid object. After the cavity generated by the ultrasonic pulse collapses, a Worthington jet is formed as for the contact-based method. The droplet formed on the tip of the jet is then to be caught acoustically and levitated sufficiently stable, in such a way that the gripper, in which the droplet levitates, can be moved to a target. Subsequently, the droplet can be dropped onto the target.

As a result, contact-less and contamination-free transport of liquid droplets is possible using a compact and cost-effective air-coupled ultrasonic robot gripper.

5.2 Acoustic Droplet Ejection

To generate a Worthington jet, a method was developed that uses piezoelectric transducers to generate an ultrasonic pulse that is focused slightly below the surface of a liquid source. Thereby, a pressure cone and an air cavity is formed inside the liquid as illustrated in Fig. 5.2. A spherical cap arrangement of piezoelectric transducers, was used for the verification of the developed method. The transducers are operated at their resonance frequency of 40 kHz. The excitation signals are generated on a Cyclone IV FPGA board and amplified by an L298N dual H-bridge board.

In order to generate a pulse, it has to be possible to adjust the acoustic output of the transducers with high bandwidth. This is achieved by adjusting the duty cycle, which is the ratio between high and low time of a square wave signal. For a duty cycle of 50 %, the maximum output is achieved. For any other duty cycle, the 40 kHz component of the excitation signal and therefore the acoustic output is reduced. The effective component of the excitation signal depending on the duty cycle

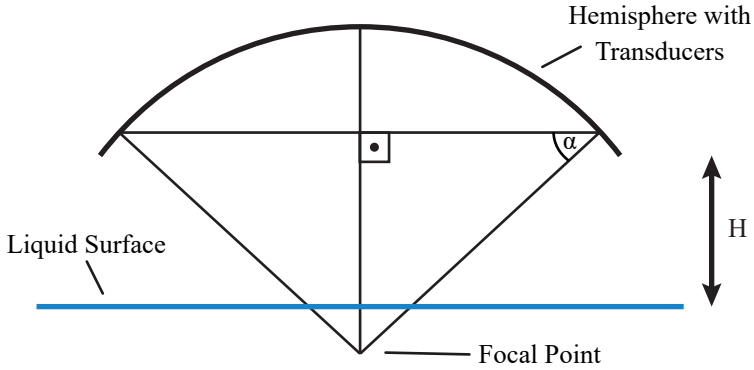


Fig. 5.2: Schematic of the droplet ejector. Experiments have shown that the cavity angle α has to be smaller than $\approx 60^\circ$ in order to be able to eject droplets. The distance H between the ejector and the liquid surface has to be chosen such that the sound waves are focused a few millimeters below the liquid surface.

can be calculated as

$$\alpha_{\text{duty}} = 4D - 4D^2 \quad (5.1)$$

where D denotes the duty cycle (value between 0 and 1), resulting in a duty cycle dependent pressure P_{duty} of

$$P_{\text{duty}} = \alpha_{\text{duty}} P_{50}, \quad (5.2)$$

where P_{50} denotes the pressure at a duty cycle of 50%. This formula was verified by measurements of the generated acoustic pressure.

The ejector is positioned in such a way that the sound waves are focused and constructively superimposed a few millimeters below the liquid surface. The duty cycle of the excitation voltage signal of the transducers is then adjusted in a sawtooth or triangular shape resulting in a droplet ejection if all conditions for a droplet generation are met. The conditions are examined in [79, 80].

To modify the droplet ejection, the excitation voltage V_{ex} , the pulse length L , the pulse shape and the distance between the ejector and the liquid surface H can be adjusted. The presented measurements were taken for a triangular shaped excitation signal. For this arrangement, an

excitation voltage between 23 V and 29 V resulted in the most consistent behaviour. The excitation voltage affects mainly the droplet diameter d_{drop} , but also the ejection height h_{eject} , as shown in Fig. 5.3. The ejection height and droplet diameter for an impulse length of $a = 6.14$ ms can be calculated as

$$h[\text{mm}] = h_{V,0} + q_{V,h}(V_{\text{ex}}[\text{V}] - 23 \text{ V})^2 \quad (5.3)$$

with $h_{V,0} = 23.8$ mm, $q_{V,h} = 0.21$ mm/V² and

$$d[\text{mm}] = d_{V,0} + q_{V,d}V_{\text{ex}}[\text{V}] \quad (5.4)$$

with $d_{V,0} = -1.45$ mm and $q_{V,d} = 0.143$ mm/V as it was obtained using a curve fitting tool.

The pulse length should be set between $a = 5$ ms and $a = 12$ ms and affects the droplet diameter and the ejection height as shown in Fig. 5.4. The ejection height and droplet diameter for an excitation voltage of $V_{\text{ex}} = 25$ V can be calculated as

$$h(a)[\text{mm}] = h_{a,0} + q_{a,h}a[\text{ms}] \quad (5.5)$$

with $h_{a,0} = 37.5$ mm, $q_{a,h} = -2.4$ mm/ms and

$$d(a)[\text{mm}] = q_d(a[\text{ms}] - a_0)^{\frac{1}{3}} \quad (5.6)$$

with $a_0 = 4$ ms and $q_d = 1.8$ mm/ms ^{$\frac{1}{3}$} as it was obtained using a curve fitting tool.

The distance between the ejector and the liquid surface has a large influence on the ejection process. It has to be set precisely and is not recommended to be used as a parameter for adjusting the droplet volume and ejection height. For the ejector used for the experiments, a distance between ejector and liquid surface of $H = 23.5$ mm was used.

The parameters were set on a PC and sent to the FPGA using UART communication. Afterwards, a signal to start the ejection process was sent to the FPGA. It is very important to handle the timing of the duty cycle adjustments on the FPGA due to the required timing accuracy. If the duty cycle adjustments are sent via UART to the FPGA, the pulse length and shape are less accurate and the variation of droplet diameter and ejection height increases.

The measurements show that it is possible to adjust the droplet volume and the ejection height by adjusting the pulse length and the excitation voltage. Similar results were obtained using other arrangements

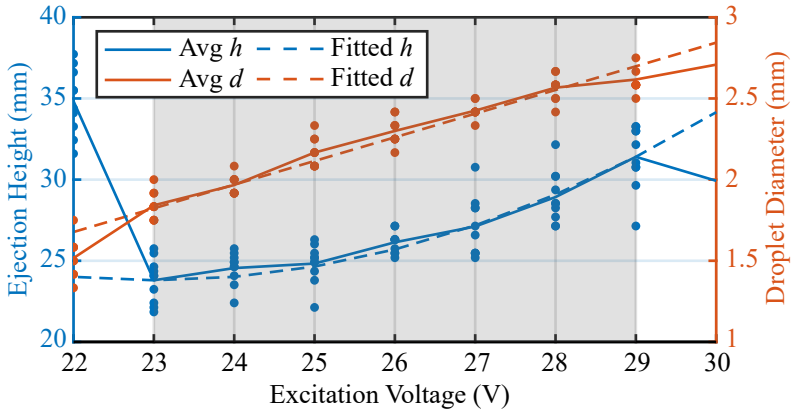


Fig. 5.3: The measured ejection height and droplet diameter for a distance of 23.5 mm between the ejector and the liquid surface and an impulse length of 6.14 ms. The ejection height and the droplet diameter can both be adjusted by varying the excitation voltage between 23 V and 29 V.

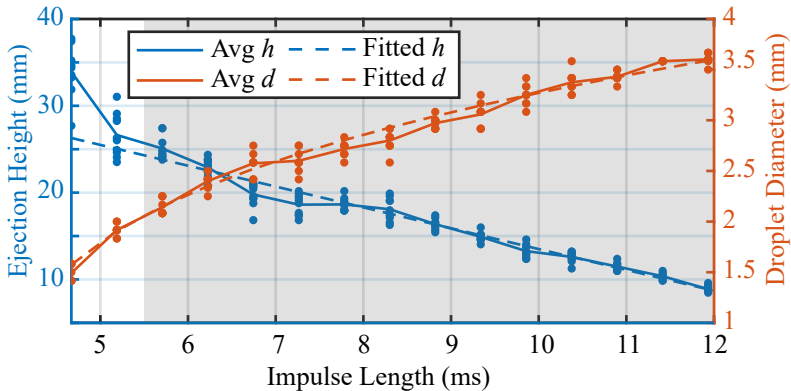


Fig. 5.4: The measured ejection height and droplet diameter for a distance of 23.5 mm between the ejector and the liquid surface and an excitation voltage of 25 V. The ejection height and the droplet diameter can both be adjusted by varying the impulse length between 5.5 ms and 12 ms. In combination with the excitation voltage variation, the droplet diameter and ejection height can be adjusted individually.

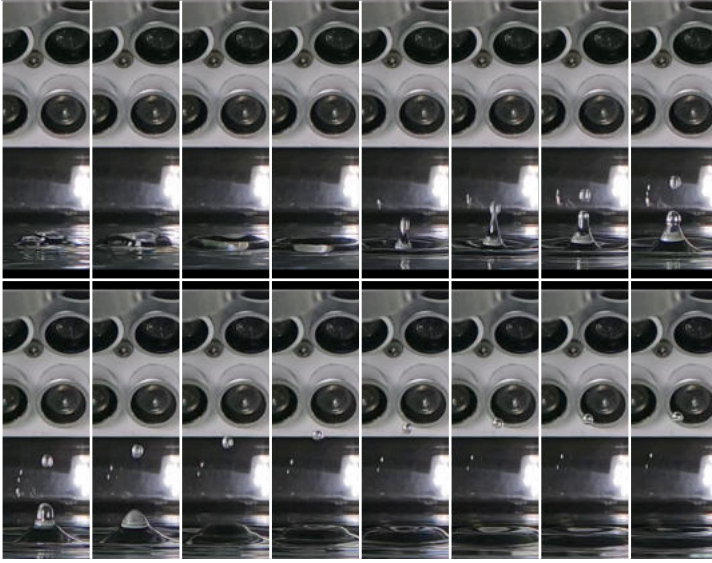


Fig. 5.5: Sequence of frames of an acoustic droplet ejection process conducted at an excitation voltage $V_{\text{ex}} = 25$ V, impulse length $a = 6.139$ ms and distance between the lower bound of the hemisphere and the water surface of $H = 23.5$ mm. The time between the frames is 5 ms.

of transducers with less transducers or smaller transducers arranged on the same gripper shape.

Pictures of a droplet ejection process illustrating the Worthington jet and droplet formation are shown in Fig. 5.5.

5.3 Droplet Levitation

Acoustic levitation of liquid droplets can be achieved using standing waves that are formed between a transducer and reflector, two opposing transducers, or two opposing arrays of transducers [35, 109, 139, 140]. Due to large trapping forces, low operating voltages are sufficient for the levitation of liquid droplets. Therefore, stable levitation of liquid droplets is achievable.

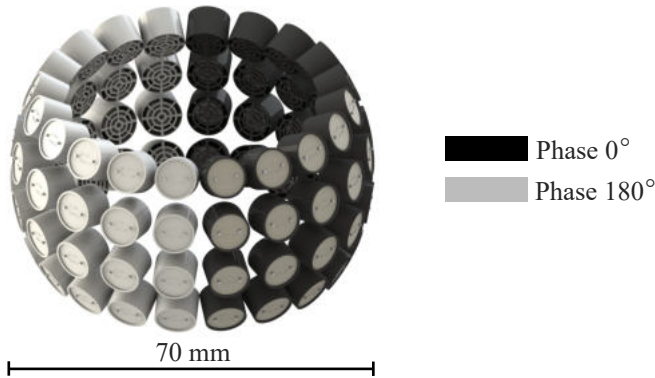


Fig. 5.6: The arrangement of transducers used to levitate and catch ejected droplets. A twin trap is used to generate the acoustic forces. Therefore, a phase shift of 180° was applied between the two horizontal halves of the transducers. The arrangement has an inner diameter of 56 mm and an outer diameter of 70 mm.

For an ultrasonic liquid gripper, a droplet is ejected using an ultrasonic pulse and has to be caught afterwards using an acoustic catcher. Standing wave levitators can not be used for the catching process since the lower part of the levitator would block the pulse for the droplet ejection. Therefore, another arrangement of transducers has to be developed, which is capable to levitate liquid droplets without transducers placed below the droplet. Using transducers in a ring-shaped arrangement, twin traps can be generated [62, 92]. However, the acoustic radiation forces caused by twin traps are significantly lower compared to standing waves. This can be compensated by increasing the excitation voltage applied to the transducers.

A ring-shaped array consisting of 64 piezoelectric transducer operating at their resonance frequency of 40 kHz, as shown in Fig. 5.6, was used to evaluate the feasibility of the liquid droplet levitation by means of twin traps.

At the required excitation voltage of $V_{\text{ex}} > 20 \text{ V}$, vibrations were excited, which caused unstable droplet levitation. It was observed that the transducers started to vibrate at high excitation voltages. Therefore, an improved method of mounting the transducers was developed, which significantly reduced or even eliminated these vibrations. For this

purpose, the transducers were embedded in the 3D printed holder and glued in place, which prevented the vibrations from occurring even for excitation voltages of $V_{\text{ex}} > 20 \text{ V}$. Position measurements of solid objects levitating in an array using the initial and improved mounting methods are shown in Fig. 5.7. A Sony RX100IV camera was used to record video footage at 1000 FPS, which was evaluated using OpenCV image processing algorithms in Python. The stability achieved with this levitator was verified by levitation of an expanded polystyrene object during the launch of a rocket, as described in Appendix B.

With this method, it is possible to levitate liquid droplets (cf. Fig. 5.8, without blocking the ultrasonic pulse for the ejection of droplets). The levitation was tested using syringes and pipettes to insert the droplet, which is quite challenging, since the syringe and pipette disturb the acoustic field. If the droplet is inserted successfully, the levitation is stable enough to allow movement of the levitator using a robotic arm.

5.4 Droplet Catching

By combining an ejector as described in section 5.2 and a ring-shaped transducer array as described in section 5.3, a liquid gripper can be built that is capable of acoustically ejecting and levitating droplets. What remains for the entire transport process to be completed is the catching process.

Two different configurations of the gripper are possible. Either the ejector is located below the catcher in such a way that the ejected droplet is ejected through a hole in the ejector to the catcher, or the catcher is located below the ejector in such a way that the ultrasonic pulse has to propagate through the ejector. Both variants are possible, but at the required ejection height of the first method, the ejection height variance is very high and the reliability very low. Slight deviations in temperature, humidity, distance between ejector and liquid surface, and other factors will result in the droplet not being caught. The reliability of the second method is better, but the deviations of ejection height and not perfectly vertical ejection result in droplets that are not caught.

The system shown in Fig. 5.9 is thus capable of acoustically ejecting, catching and transporting a droplet. Compared to state-of-the-art acoustic droplet ejection systems, the transducers are coupled to the liquid through air instead of liquid coupling between the ultrasonic transducer and the liquid container. To increase the reliability of the system, a

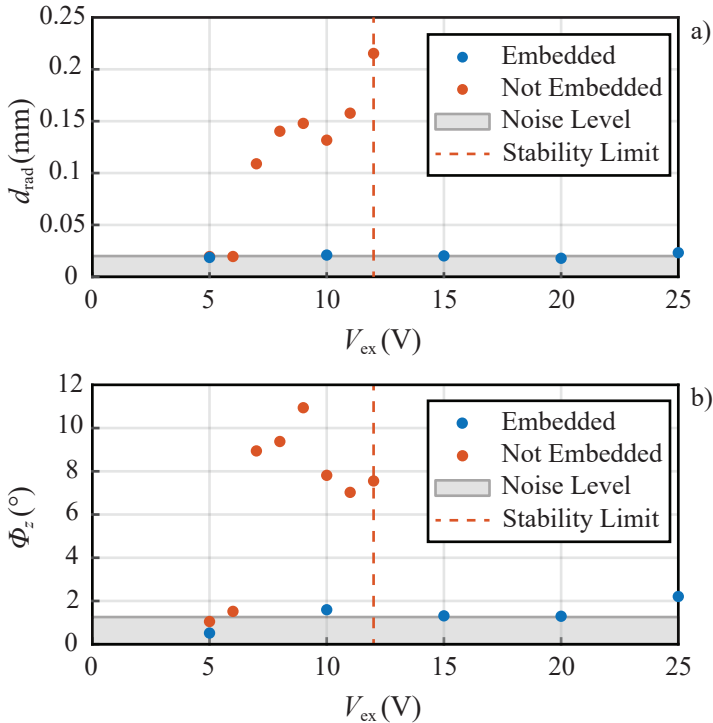


Fig. 5.7: Standard deviation of the position in radial direction (a) and the orientation angle around the vertical axis (b) for excitation voltages between 5 V and 25 V. The measurements are compared for the same arrangement with embedded transducers (blue) and not embedded transducers (red). The maximum excitation voltage without embedded transducers was determined to be 12 V. For larger voltages the vibrations were too strong and the particle was ejected from the acoustic field. With embedded transducers, excitation voltages up to 25 V can be applied while still achieving stable levitation.

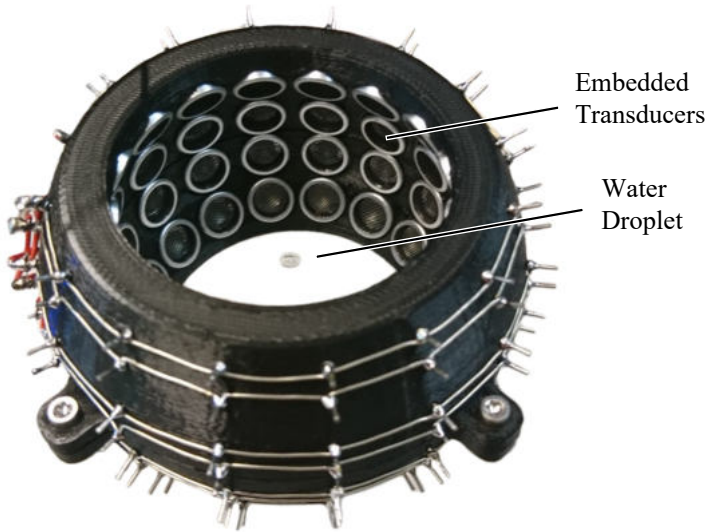


Fig. 5.8: The arrangement, which is used to catch liquid droplets. A water droplet was inserted using a syringe. An excitation voltage of $V_{\text{ex}} = 23 \text{ V}$ was used. The levitation was stable enough to move the gripper while the droplet was levitating. The gripper has an inner diameter of 56 mm and an outer diameter of 74 mm.

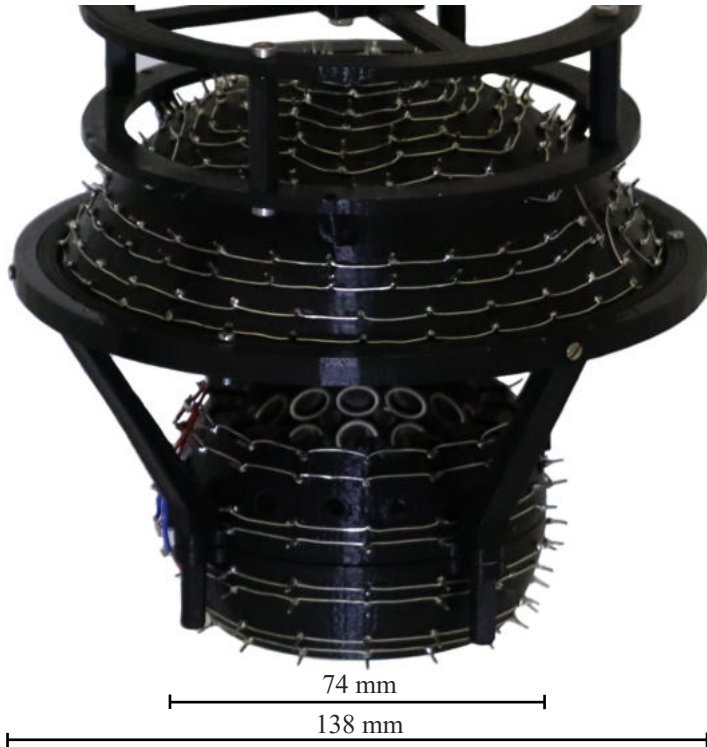


Fig. 5.9: The first robot gripper, which is capable of ejecting liquid droplets, catching them, and transporting them to a target in a contamination free manner. The upper part of the gripper is used to generate an ultrasonic pulse which is focussed slightly below the surface of the liquid located below the gripper. As a result, a droplet is ejected, which can be caught by the lower part of the gripper.

closed-loop control system would be conceivable, which measures the position of the droplet and could thus adjust the pressure field in such a way that the droplet can be caught. For this purpose, the transducers would have to be controlled individually. The control system would be similar to the one described in section 3.5. Furthermore, the system could be extended by temperature, humidity and distance sensors, which can be taken into account when positioning the ejector for improved reliability. The complexity would significantly increase, but it would be necessary for the development of a system that works reliably and in an automated manner.

6

Outlook

6.1 Solid Grippers

The grippers presented in this work are capable of transporting objects smaller than half the wavelength, which corresponds to about 4.3 mm and 6.9 mm at the excitation frequencies 40 kHz and 25 kHz, respectively. It is possible to

- ▶ transport low density objects ($\rho \leq 0.1 \text{ g/cm}^3$) to and from acoustically transparent surfaces using a single-sided gripper. Thereby, the position and orientation can be controlled in five degrees of freedom;
- ▶ transport low density objects ($\rho \leq 0.1 \text{ g/cm}^3$) to and from acoustically reflective surfaces using a single-sided gripper. Thereby, the position and orientation can be controlled in five degrees of freedom;
- ▶ transport high density objects ($\rho \leq 7.3 \text{ g/cm}^3$) to and from acoustically transparent surfaces using a double-sided gripper. Thereby, the position and orientation can be controlled in six degrees of freedom;
- ▶ transport high density objects ($\rho \leq 7.3 \text{ g/cm}^3$) to and from acoustically reflective surfaces using a reflector gripper. Thereby, the position and orientation can be controlled in four degrees of freedom.

Additionally, it is possible to control the position and orientation with a closed-loop control system for all grippers. Cameras and image

processing algorithms presented in this work can be used to detect the position and orientation of the levitating objects.

Thus, transport processes for the targeted object size range ($d < 1$ cm) can be automated under certain conditions. For the moment, a relatively large reflector is used to pick up high density objects from acoustically reflective surfaces. Thereby, it is only possible to transport objects located in flat environments since the gripper requires a large space for its movement. If the size of the reflector can be reduced and its shape optimized, further transport processes can be optimized using such a gripper.

A gripper, which can operate without a reflector, would have even fewer requirements for the environment. The single-sided gripper can currently only transport very light objects ($\rho < 0.1$ g/cm³). In order to increase the weight of the objects to be transported, methods must be developed that maximize the vertical acoustic radiation force while taking reflections and object geometry into account. This also includes optimizing the positioning of the transducers. For this purpose, the forces have to be calculated using the surface integral (Eq. 2.3) rather than using the Gor'kov potential approximation. This would require individual control of the transducers which further increases the complexity of the system.

In order to use acoustic robot grippers for the transport of much larger objects, methods that can exert an acoustic force at several points on a large object and thereby pick up and transport the object need to be developed. Similar methods were already presented for mid-air manipulation of large objects [72, 73].

The current state of the grippers only allows low throughput, since the transport of individual components takes a long time, especially for high-density objects. This is due to the lack of stability during strong accelerations. To improve the stability of the grippers, more powerful and expensive transducers can be used. Furthermore, it has recently been shown that a calibration of the transducers can significantly improve their performance [90].

6.2 Liquid Grippers

Current ADE methods are complex, expensive, and require contact-based target plates. The goal of developing a contact-less liquid gripper is to open up more applications that are currently not feasible with ADE methods due to the high cost or contact-based target plates.

The gripper developed in this work is capable of ejecting droplets with adjustable droplet size and ejection height. The ejection process works reliably for constant ambient conditions, i.e. temperature and humidity, and precise positioning of the gripper. If the gripper is to be used in automated processes, the gripper needs to be equipped with sensors that measure these conditions.

Using the droplet levitator presented in this work, liquid droplets can be levitated in a reliable manner. However, it is difficult to insert the droplet into the levitation field. Using a syringe or a pipette disturbs the pressure field and thereby influences the levitation stability. If the droplet is inserted successfully, the levitation is stable enough to move the levitator using a robot arm.

For the liquid gripper, a droplet is ejected using an ultrasonic pulse and is to be caught by the levitator subsequently. The pressure field is thereby not disturbed by a syringe or a pipette. Nevertheless, the catching process still does not work very reliable, since the ejection height varies and the droplets are not always ejected perfectly vertical. A closed-loop control system could be used in the future to detect the position and the trajectory of the droplet in order to catch it. Cameras and image processing algorithms can be used for the position detection, but the detection of liquid droplets is more difficult compared to solid objects due to their transparency. Therefore, other types of sensors could be evaluated as well. Furthermore, individual control of the transducers of the droplet catcher would be required in order to manipulate the pressure field, such that the trap is moved to the catching position.

If the ejection and catching process operate reliably, the gripper can be used to inspect, transport, or merge liquid droplets in an automated, contact-less, cost-effective, and contamination-free manner. The gripper would be significantly more compact compared to current ADE devices. Due to the reduced costs, it would be possible to use contact-less acoustic transportation methods for applications, for which it was previously not profitable.

Appendices



Measurements of Acoustic Pressure Fields using Schlieren Photography

A.1 Introduction

Standing acoustic waves can be used to pick up, levitate and manipulate small objects and liquids. When developing and analysing an acoustic levitation device, the pressure field can be calculated analytically. Sound wave reflections caused by the environment, the object shape and material properties are often not taken into account for simplicity reasons. Schlieren photography can be used to verify the accuracy of the calculations by visualizing the pressure field in a non intrusive way. This chapter presents an implementation of a Schlieren photography system that is easy and quick to set up and calibrate. With its help, a quick comparison between the calculated and the actual pressure field can be carried out. Various optical components were procured and custom parts were designed and manufactured in order to keep them in a fixed position relative to each other. This allows the calibration time for the system to be kept to a minimum. The final system was used to visualize pressure fields inside common acoustic levitation devices. A comparison between various image enhancement methods was carried out.

A.2 Schlieren Photography

Schlieren photography, first mentioned in 1864 by August Toepler [141], is a technique that visualizes density variations in gaseous media. It is used for visualisations in the fields of fluid mechanics and engineering,

e.g., for studying the breathing of animals and humans or the analysis of shock waves created by fast moving objects [142].

Schlieren photography works on the principle of Snell's law of refraction [143]. With its help changes in the refractive indexes of two media can be visualized. A change in the refractive index can be the result of several factors such as changes in the composition of the gas [144, 145], temperature changes [145] or changes in the density of the gas as a result of mechanical forces [142].

The speed of light, except in a vacuum, is dependent on the refractive index of the medium it travels in. Schlieren photography is based on this principle. The dependency can be described as

$$v = \frac{c}{n}, \quad (\text{A.1})$$

where v is the speed of light in the medium, c the speed of light in vacuum and n the refractive index of the medium. When a light ray travels through inhomogeneous media and encounters a change in the refractive index, it gets deflected according to Snell's law of refraction. The relation between the amount of deflection ϵ for a given refractive index gradient is approximated as [146]

$$\epsilon \approx Cl \frac{d\rho}{dy}, \quad (\text{A.2})$$

where C , $\frac{d\rho}{dy}$ and l denote the Gladstone-Dale constant, the air-density gradient and the travel distance through air with density gradient, respectively. This results in a deflection distance Δa of

$$\Delta a = d \tan(\epsilon) \approx d\epsilon, \quad (\text{A.3})$$

as illustrated in Fig A.1 [147].

The deflection of the light ray can be used to block strong deflections using a razor blade and thereby visualize pressure gradients.

A.2.1 Topology

There are different types of Schlieren photography topologies. All of them focus light into a focus point and block deflected light rays. A camera is placed behind the focus point and detects brightness changes depending on the amount of deflected and blocked light rays. In this

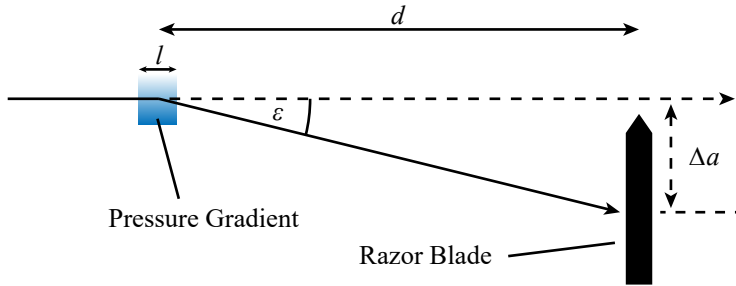


Fig. A.1: Illustration of Snell's law for light rays travelling through a pressure gradient of length l .

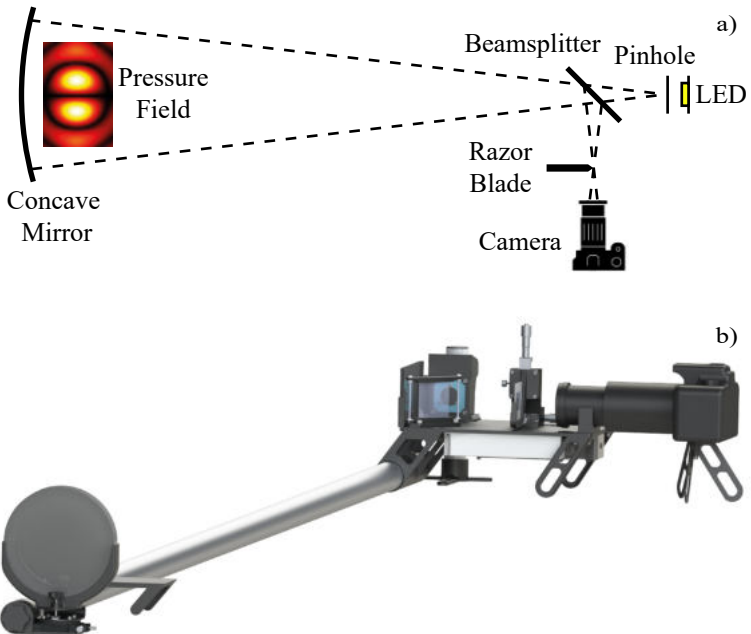


Fig. A.2: (a) The Schlieren photography topology with a beamsplitter, which was used for the device developed in this work and (b) a rendering of the system.

work, a beamsplitter setup, as illustrated in Fig. A.2a, was used to visualize acoustic pressure fields.

An LED (Citizen CLU721-1206C4-403M2K1, 4750 lm) is used to generate high intensity light, which is converted to a point source using a 50 μm pinhole (Edmund Optics 56-282). The light passes through the beamsplitter (Edmund Optics 43-359), which reflects 50% of the light and transmits the other 50%. The light then travels through the pressure field that is to be visualized, before being reflected by the concave mirror (Edmund Optics 71-026) and travelling through the pressure field for a second time. The beamsplitter then reflects 50% of the light, which is focused on the edge of a razor blade. The camera (Canon EOS 250D with a Canon EF-S 55-250 mm lens) is used to capture an image focussed on the edge of the razor blade, which visualizes the pressure field. The system is very sensitive regarding slight movements of components. The components, especially the mirror and the razor blade, have to be positioned very accurately, which is achieved by precise holders and microsleds as visualized in Fig. A.2b.

The razor blade can be replaced by a rainbow filter. A rainbow filter uses a color gradient printed onto a photographic film. Pressure gradients result in a change of color in the final image instead of a change of brightness for razor blades [147].

A movement subtraction algorithm was used to reduce noise in the captured images. It uses multiple images taken in short time intervals and takes the mean value of each pixel.

A.2.2 Results

The system was tested using a TinyLev levitator [35] and the double-sided robot gripper presented in Section 3.4. The pressure field was visualized using a razor blade and a 1 mm rainbow filter. The captured images and the calculated pressure fields are shown in Fig. A.3 and Fig. A.4.

The visualizations of the pressure fields agree very well with the calculated pressure fields, as shown in Fig. A.5. Schlieren photography can thus be used to visualize pressure fields without disturbing it and to detect defects in a device. In addition, this technology can also be used to visualize and investigate other disturbance factors such as reflections from the environment or pressure fluctuations due to the heating of the transducers.

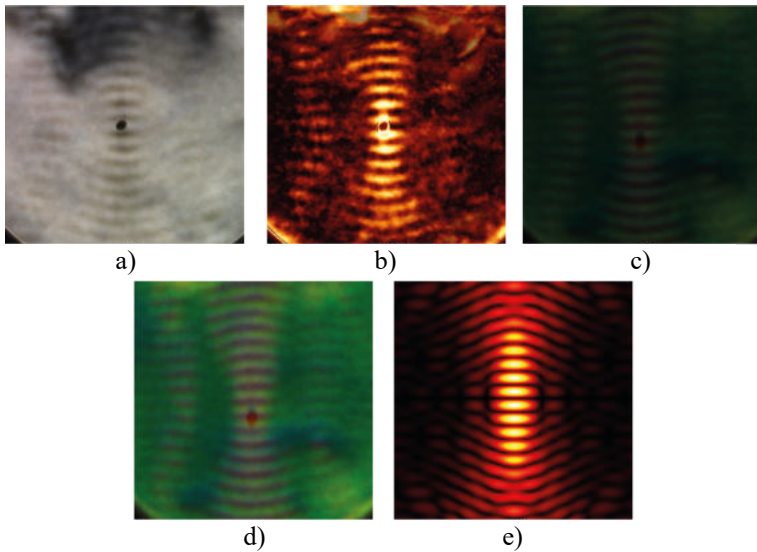


Fig. A.3: Schlieren photography images using pressure fields generated by a TinyLev levitation device. All images were taken with activated movement subtraction algorithm. a) razor blade image b) custom colormap (yellow fox) c) 1 mm rainbow filter image d) 1 mm rainbow filter image with enhanced brightness and saturation, and e) calculated pressure field.

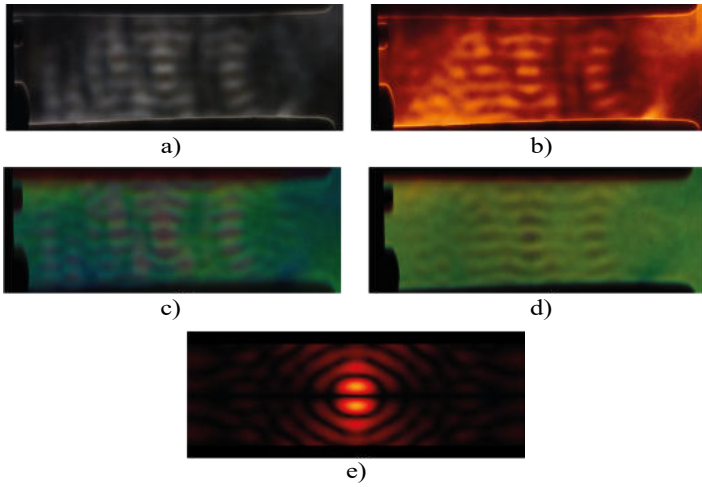


Fig. A.4: Schlieren photography images using pressure fields generated by a double-sided acoustic robot gripper. All images were taken with activated movement subtraction algorithm. a) razor blade image b) custom colormap (afmhot) c) 1 mm rainbow filter image with enhanced brightness and saturation, d) 2 mm rainbow filter image with enhanced brightness and saturation, and e) calculated pressure field.

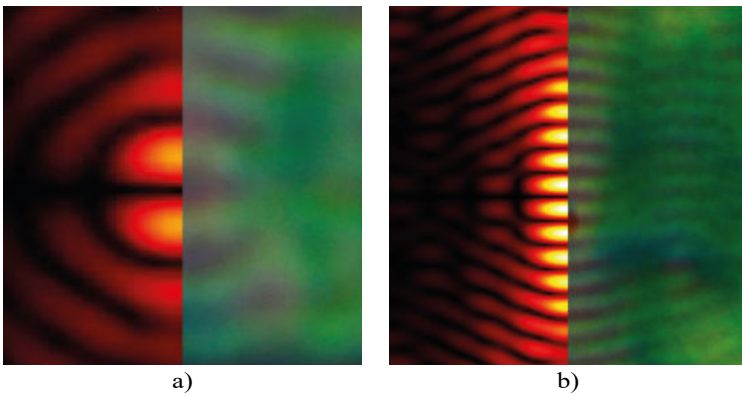


Fig. A.5: Comparison between the visualized and calculated pressure field for (a) a double-sided acoustic robot gripper and (b) a TinyLev levitator.

B

Stability Evaluation for an Acoustic Levitator During a Rocket Launch

B.1 Introduction

The stability that can be achieved with acoustic levitation systems is significantly increased when the transducers are embedded in the holder, as demonstrated in Chapter 5. The ring-shaped array used for the high-bandwidth manipulation experiments (Section 3.6) and the droplet levitator (Section 5.3) was used to evaluate the maximum acceleration of the levitator before light objects are ejected from the acoustic trap.

For this purpose, the opportunity to provide the payload for a rocket launch of project PICCARD by Akademische Raumfahrt Initiative Schweiz (ARIS) [148] was utilized. Thereby three cubesat units, as shown in Fig. B.1a, were provided and the test system was integrated in the units. The rocket was designed such that the payload could be inserted into the nosecone. Project PICCARD had the target of building a hybrid-propellant rocket capable of reaching an apogee of 30 000 ft and to recover all parts safely [148].

B.2 Rocket Launch

Due to the procedure required before the launch of a rocket, the payload had to be inserted into the nosecone a few hours before the launch. Thus, the levitator had to be capable of levitating an expanded polystyrene ball for about seven hours using power provided by lithium ion batteries inside the payload. Furthermore, two Raspberry Pi Zero Ws with an

attached camera (Raspberry Pi Camera Module V2), a Raspberry Pi Zero W with an attached LED module (Raspberry Pi Bright Pi) and an IMU (MPU9250) were powered using a power bank (Anker PowerCore, 13 000 mAh, 5 W). A delay of four hours between the insertion of the payload and the start of capturing video footage was implemented in order to save memory space on the SD cards to ensure that video footage was captured during the launch. The bottom cubesat was used for the batteries and the power bank, the middle cubesat for the levitator and the top cubesat for the Raspberry Pis and the sensors.

The rocket shown in Fig. B.1d was launched at the European Rocketry Challenge (EuRoC) 2021 in Portugal. Due to a broken connector between the filling line and the intermediate tank, the launch of PICCARD to its maximum capability was not an option. After the successful launch of the PICCARD rocket, an apogee of about 21 000 ft was detected. The planned separation of the nosecone after apogee did not work. This resulted in a brief ballistic flight, whereas the high roll rate caused the nosecone shear pins to break and shortly after, the parachutes (cf. Fig. B.1c) being pulled [148]. The high loads caused the levitating object to be ejected from the acoustic trap.

During the launch of the rocket, the object levitated stably in the acoustic trap, as shown in Fig. B.1b. The measurement of the accelerations in Fig. B.2a-d show, that the levitator withstood accelerations up to 13 g. The vertical position of the levitating object, shown in Fig. B.2e, was evaluated using the video footage of the Raspberry Pi camera modules and image processing algorithms. It shows, that the object moves significantly inside the trap when the levitator is accelerated. The moment when the shear pins of the nosecone broke and caused the object to be ejected from the trap is indicated by the red line.

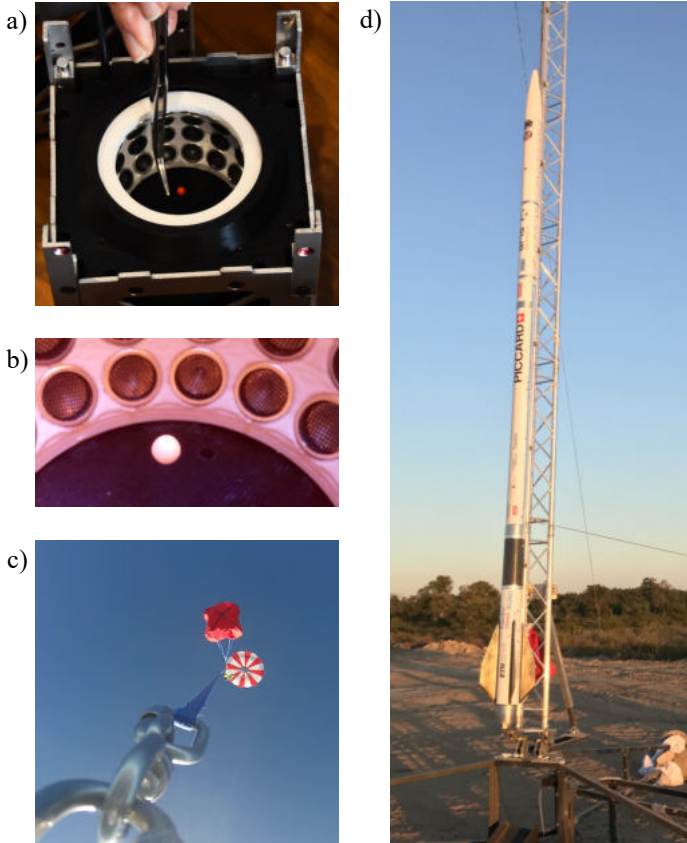


Fig. B.1: (a) The levitator, which was used to test the stability of a levitating expanded polystyrene ball in a cubesat unit, (b) the levitating object during the rocket launch captured by a Raspberri Pi and an attached camera module, (c) the parachute, which caused the object to be ejected from the acoustic trap, and (d) the PICCARD rocket from the ARIS project, which carried the levitator as a payload.

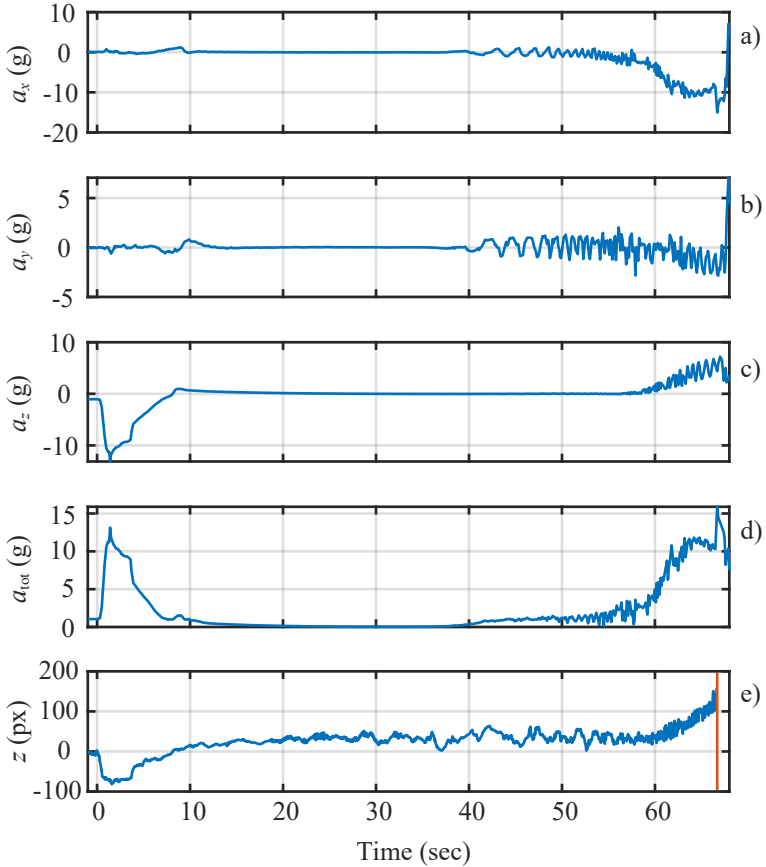


Fig. B.2: Acceleration measurement data of an IMU located inside the rocket in (a) x -, (b) y -, (c) z -direction and (d) the total acceleration normalized with the gravity of earth (g). (e) shows a measurement of the vertical position of an expanded polystyrene ball inside the acoustic levitator. The moment when the shear pins of the nosecone broke and caused the object to be ejected from the acoustic trap is indicated by the red line.

Bibliography

- [1] Soft Robotics Inc. [Online]. Available: <https://www.softroboticsinc.com/>
- [2] K. C. Galloway, K. P. Becker, B. Phillips, J. Kirby, S. Licht, D. Tchernov, R. J. Wood, and D. F. Gruber, “Soft robotic grippers for biological sampling on deep reefs,” *Soft Robotics*, vol. 3, no. 1, pp. 23–33, 2016, pMID: 27625917. DOI: [10.1089/soro.2015.0019](https://doi.org/10.1089/soro.2015.0019), [PDF].
- [3] J. Shintake, V. Cacucciolo, D. Floreano, and H. Shea, “Soft robotic grippers,” *Advanced Materials*, vol. 30, no. 29, p. 1707035, 2018, DOI: [10.1002/adma.201707035](https://doi.org/10.1002/adma.201707035), [PDF].
- [4] S. Song, C. Majidi, and M. Sitti, “Geckogripper: A soft, inflatable robotic gripper using gecko-inspired elastomer micro-fiber adhesives,” *RSSJ International Conference on Intelligent Robots and Systems*, pp. 4624–4629, 2014, DOI: [10.1109/IROS.2014.6943218](https://doi.org/10.1109/IROS.2014.6943218), [PDF].
- [5] Q. Guo, X. Su, X. Zhang, M. Shao, H. Yu, and D. Li, “A review on acoustic droplet ejection technology and system,” *Soft Matter*, vol. 17, pp. 3010–3021, 2021, DOI: [10.1039/D0SM02193H](https://doi.org/10.1039/D0SM02193H), [PDF].
- [6] S. Santesson and S. Nilsson, “Airborne chemistry: Acoustic levitation in chemical analysis,” *Analytical and Bioanalytical Chemistry*, vol. 378, pp. 1704–1709, 2004, DOI: [10.1007/s00216-003-2403-2](https://doi.org/10.1007/s00216-003-2403-2), [PDF].
- [7] W. J. Xie, C. D. Cao, Y. J. Lü, Z. Y. Hong, and B. Wei, “Acoustic method for levitation of small living animals,” *Applied Physics Letters*, vol. 89, no. 21, p. 214102, 2006, DOI: [10.1063/1.2396893](https://doi.org/10.1063/1.2396893), [PDF].
- [8] M. Sundvik, H. J. Nieminen, A. Salmi, P. Panula, and E. Hægström, “Effects of acoustic levitation on the development of zebrafish, *Danio rerio*, embryos,” *Scientific Reports*, vol. 5, no. 1, p. 13596, 2015, DOI: [10.1038/srep13596](https://doi.org/10.1038/srep13596), [PDF].
- [9] J. K. R. Weber, C. Benmore, S. Tumber, A. Taylor, C. Rey, L. Taylor, and S. Byrn, “Acoustic levitation: Recent developments and emerging opportunities in biomaterials research,” *Eur*

- ropean Biophysics Journal : EBJ*, vol. 41, pp. 397–403, 2011, DOI: [10.1007/s00249-011-0767-3](https://doi.org/10.1007/s00249-011-0767-3), [PDF].
- [10] B. R. Wood, P. Heraud, S. Stojkovic, D. Morrison, J. Beardall, and D. McNaughton, “A portable raman acoustic levitation spectroscopic system for the identification and environmental monitoring of algal cells,” *Analytical Chemistry*, vol. 77, no. 15, pp. 4955–4961, 2005, DOI: [10.1021/ac050281z](https://doi.org/10.1021/ac050281z), [PDF].
- [11] L. Puskar, R. Tuckermann, T. Frosch, J. Popp, V. Ly, D. McNaughton, and B. R. Wood, “Raman acoustic levitation spectroscopy of red blood cells and *Plasmodium falciparum* trophozoites,” *Lab Chip*, vol. 7, no. 9, pp. 1125–1131, 2007, DOI: [10.1039/B706997A](https://doi.org/10.1039/B706997A), [PDF].
- [12] V. Contreras, R. Valencia, J. Peralta, H. Sobral, M. A. Meneses-Nava, and H. Martinez, “Chemical elemental analysis of single acoustic-levitated water droplets by laser-induced breakdown spectroscopy,” *Opt. Lett.*, vol. 43, no. 10, pp. 2260–2263, 2018, DOI: [10.1364/OL.43.002260](https://doi.org/10.1364/OL.43.002260), [PDF].
- [13] A. M. Seddon, S. J. Richardson, K. Rastogi, T. S. Plivelic, A. M. Squires, and C. Pfrang, “Control of nanomaterial self-assembly in ultrasonically levitated droplets,” *Journal of Physical Chemistry Letters*, vol. 7, no. 7, pp. 1341–1345, 2016, DOI: [10.1021/acs.jpcclett.6b00449](https://doi.org/10.1021/acs.jpcclett.6b00449), [PDF].
- [14] Y. Hashimoto, Y. Koike, and S. Ueha, “Acoustic levitation of planar objects using a longitudinal vibration mode,” *Journal of the Acoustical Society of Japan (E)*, vol. 16, no. 3, pp. 189–192, 1995, DOI: [10.1250/ast.16.189](https://doi.org/10.1250/ast.16.189), [PDF].
- [15] Y. Hashimoto, Y. Koike, and S. Ueha, “Near-field acoustic levitation of planar specimens using flexural vibration,” *Journal of the Acoustical Society of America*, vol. 100, no. 4, pp. 2057–2061, 1996, DOI: [10.1121/1.417915](https://doi.org/10.1121/1.417915), [PDF].
- [16] Y. Hashimoto, Y. Koike, and S. Ueha, “Transporting objects without contact using flexural traveling waves,” *Journal of the Acoustical Society of America*, vol. 103, no. 6, pp. 3230–3233, 1998, DOI: [10.1121/1.423039](https://doi.org/10.1121/1.423039), [PDF].

-
- [17] G. Reinhart, J. Hoepfner, and J. Zimmermann, “Non-contact wafer handling using high-intensity ultrasonics,” *SEMI Advanced Semiconductor Manufacturing Conference*, pp. 139–140, 2001, DOI: [10.1109/ASMC.2001.925636](https://doi.org/10.1109/ASMC.2001.925636), [PDF].
- [18] D. Foresti, G. Sambatakakis, S. Bottan, and D. Poulikakos, “Morphing surfaces enable acoustophoretic contactless transport of ultrahigh-density matter in air,” *Scientific Reports*, vol. 3, no. 1, p. 3176, 2013, DOI: [10.1038/srep03176](https://doi.org/10.1038/srep03176), [PDF].
- [19] P. C. Nordine, D. Merkley, J. Sickel, S. Finkelman, R. Telle, A. Kaiser, and R. Prieler, “A levitation instrument for containerless study of molten materials,” *Review of Scientific Instruments*, vol. 83, no. 12, p. 125107, 2012, DOI: [10.1063/1.4770125](https://doi.org/10.1063/1.4770125), [PDF].
- [20] N. Yan, Z. Y. Hong, D. Geng, and B. Wei, “A comparison of acoustic levitation with microgravity processing for containerless solidification of ternary Al–Cu–Sn alloy,” *Applied Physics A*, vol. 120, 2015, DOI: [10.1007/s00339-015-9151-y](https://doi.org/10.1007/s00339-015-9151-y), [PDF].
- [21] K. Ohsaka and E. Trinh, “Three-lobed shape bifurcation of rotating liquid drops,” *Physical Review Letters*, vol. 84, pp. 1700–1703, 2000, DOI: [10.1103/PhysRevLett.84.1700](https://doi.org/10.1103/PhysRevLett.84.1700), [PDF].
- [22] C. Shen, W. Xie, and B. Wei, “Parametrically excited sectorial oscillation of liquid drops floating in ultrasound,” *Physical Review E*, vol. 81, p. 46305, 2010, DOI: [10.1103/PhysRevE.81.046305](https://doi.org/10.1103/PhysRevE.81.046305), [PDF].
- [23] J. Arcenegui-Troya, A. Belman-Martínez, A. A. Castrejón-Pita, and J. R. Castrejón-Pita, “A simple levitated-drop tensiometer,” *Review of Scientific Instruments*, vol. 90, no. 9, p. 095109, 2019, DOI: [10.1063/1.5096959](https://doi.org/10.1063/1.5096959), [PDF].
- [24] S. Tsujino, A. Shinoda, and T. Tomizaki, “On-demand droplet loading of ultrasonic acoustic levitator and its application for protein crystallography experiments,” *Applied Physics Letters*, vol. 114, no. 21, p. 213702, 2019, DOI: [10.1063/1.5095574](https://doi.org/10.1063/1.5095574), [PDF].
- [25] E. Chladini, “Entdeckungen über die Theorie des Klages (in German),” *Weidmanns Erben und Reich*, 1787, DOI: [10.3931/e-rara-4235](https://doi.org/10.3931/e-rara-4235), [PDF].

- [26] A. Kundt, “Ueber eine neue Art akustischer Staubfiguren und über die Anwendung derselben zur Bestimmung der Schallgeschwindigkeit in festen Koerpern und Gasen (in German),” *Annalen der Physik*, vol. 203, no. 4, pp. 497–523, 1866, DOI: [10.1002/andp.18662030402](https://doi.org/10.1002/andp.18662030402), [PDF].
- [27] K. Bücks and H. Müller, “Ueber einige Beobachtungen an schwingenden Piezoquarzen und ihrem Schallfeld (in German),” *Zeitschrift für Physik*, vol. 84, no. 1, pp. 75–86, 1933, DOI: [10.1007/BF01330275](https://doi.org/10.1007/BF01330275), [PDF].
- [28] M. A. B. Andrade, N. Pérez, and J. C. Adamowski, “Review of progress in acoustic levitation,” *Brazilian Journal of Physics*, vol. 48, no. 2, pp. 190–213, 2018, DOI: [10.1007/s13538-017-0552-6](https://doi.org/10.1007/s13538-017-0552-6), [PDF].
- [29] W. J. Xie and B. Wei, “Dependence of acoustic levitation capabilities on geometric parameters,” *Physical Review E*, vol. 66, p. 026605, 2002, DOI: [10.1103/PhysRevE.66.026605](https://doi.org/10.1103/PhysRevE.66.026605), [PDF].
- [30] M. A. B. Andrade, F. Buiocchi, and J. C. Adamowski, “Finite element analysis and optimization of a single-axis acoustic levitator,” *IEEE Transactions on Ultrasonics, Ferroelectrics, and Frequency Control*, vol. 57, no. 2, pp. 469–479, 2010, DOI: [10.1109/TUFFC.2010.1427](https://doi.org/10.1109/TUFFC.2010.1427), [PDF].
- [31] R. Whymark, “Acoustic field positioning for containerless processing,” *Ultrasonics*, vol. 13, no. 6, pp. 251–261, 1975, DOI: [10.1016/0041-624X\(75\)90072-4](https://doi.org/10.1016/0041-624X(75)90072-4), [PDF].
- [32] W. A. Oran, L. H. Berge, and H. W. Parker, “Parametric study of an acoustic levitation system,” *Review of Scientific Instruments*, vol. 51, no. 5, pp. 626–631, 1980, DOI: [10.1063/1.1136268](https://doi.org/10.1063/1.1136268), [PDF].
- [33] E. H. Trinh, “Compact acoustic levitation device for studies in fluid dynamics and material science in the laboratory and microgravity,” *Review of Scientific Instruments*, vol. 56, no. 11, pp. 2059–2065, 1985, DOI: [10.1063/1.1138419](https://doi.org/10.1063/1.1138419), [PDF].
- [34] J. K. R. Weber, C. A. Rey, J. Neufeind, and C. J. Benmore, “Acoustic levitator for structure measurements on low temperature liquid droplets,” *Review of Scientific Instruments*, vol. 80, no. 8, p. 083904, 2009, DOI: [10.1063/1.3196177](https://doi.org/10.1063/1.3196177), [PDF].

-
- [35] A. Marzo, A. Barnes, and B. W. Drinkwater, “Tinylev: A multi-emitter single-axis acoustic levitator,” *Review of Scientific Instruments*, vol. 88, no. 8, p. 085105, 2017, DOI: [10.1063/1.4989995](https://doi.org/10.1063/1.4989995), [PDF].
- [36] M. Röthlisberger, G. Schmidli, M. Schuck, and J. W. Kolar, “Multi-frequency acoustic levitation and trapping of particles in all degrees of freedom,” *IEEE Transactions on Ultrasonics, Ferroelectrics, and Frequency Control*, vol. 69, no. 4, pp. 1572–1575, 2022, DOI: [10.1109/TUFFC.2022.3149302](https://doi.org/10.1109/TUFFC.2022.3149302), [PDF].
- [37] E. Trinh, J. Robey, N. Jacobi, and T. Wang, “Dual-temperature acoustic levitation and sample transport apparatus,” *Journal of the Acoustical Society of America*, vol. 79, no. 3, pp. 604–612, 1986, DOI: [10.1121/1.393450](https://doi.org/10.1121/1.393450), [PDF].
- [38] H. Hatano, Y. Kanai, Y. Ikegami, T. Fujii, and K. Saito, “Ultrasonic levitation and positioning of samples,” *Japanese Journal of Applied Physics*, vol. 21, no. S3, p. 202, 1982, DOI: [10.7567/JJAPS.21S3.202](https://doi.org/10.7567/JJAPS.21S3.202), [PDF].
- [39] S. L. Min, R. G. Holt, and R. E. Apfel, “Simulation of drop dynamics in an acoustic positioning chamber,” *Journal of the Acoustical Society of America*, vol. 91, no. 6, pp. 3157–3165, 1992, DOI: [10.1121/1.402854](https://doi.org/10.1121/1.402854), [PDF].
- [40] T. G. Wang, E. H. Trinh, A. P. Croonquist, and D. D. Elleman, “Shapes of rotating free drops: Spacelab experimental results,” *Phys. Rev. Lett.*, vol. 56, pp. 452–455, 1986, DOI: [10.1103/PhysRevLett.56.452](https://doi.org/10.1103/PhysRevLett.56.452), [PDF].
- [41] T. Wang, E. Trinh, W.-K. Rhim, D. Kerrisk, M. Barmatz, and D. Elleman, “Containerless processing technologies at the Jet Propulsion Laboratory,” *Acta Astronautica*, vol. 11, no. 3, pp. 233–237, 1984, DOI: [10.1016/0094-5765\(84\)90113-9](https://doi.org/10.1016/0094-5765(84)90113-9), [PDF].
- [42] T. Wang, “Acoustic levitation and manipulation for space applications,” *Ultrasonics Symposium*, pp. 471–475, 1979, DOI: [10.1109/ULTSYM.1979.197246](https://doi.org/10.1109/ULTSYM.1979.197246), [PDF].
- [43] T. G. Wang, A. V. Anilkumar, C. P. Lee, and K. C. Lin, “Bifurcation of rotating liquid drops: Results from USML-1 experiments

- in space,” *Journal of Fluid Mechanics*, vol. 276, p. 389–403, 1994, DOI: [10.1017/S0022112094002612](https://doi.org/10.1017/S0022112094002612), [PDF].
- [44] T. G. Wang, A. V. Anilkumar, and C. P. Lee, “Oscillations of liquid drops: Results from USML-1 experiments in space,” *Journal of Fluid Mechanics*, vol. 308, p. 1–14, 1996, DOI: [10.1017/S002211209600136X](https://doi.org/10.1017/S002211209600136X), [PDF].
- [45] E. Lierke, R. Grossbach, K. Flogel, and P. Clancy, “Acoustic positioning for space processing of materials science samples in mirror furnaces,” *Ultrasonics Symposium*, pp. 1129–1139, 1983, DOI: [10.1109/ULTSYM.1983.198240](https://doi.org/10.1109/ULTSYM.1983.198240), [PDF].
- [46] E. G. Lierke, “Acoustic levitation - a comprehensive survey of principles and applications,” *Acta Acustica united with Acustica*, vol. 82, no. 2, pp. 220–237, 1996, [PDF].
- [47] E. G. Lierke, “Deformation and displacement of liquid drops in an optimized acoustic standing wave levitator,” *Acta Acustica united with Acustica*, vol. 88, no. 2, pp. 206–217, 2002, [PDF].
- [48] H. W. S. Clair, “Agglomeration of smoke, fog, or dust particles by sonic waves,” *Ind. Eng. Chem.*, vol. 41, no. 11, pp. 2434–2438, 1949, DOI: [10.1021/ie50479a022](https://doi.org/10.1021/ie50479a022), [PDF].
- [49] C. H. Allen and I. Rudnick, “A powerful high frequency siren,” *Journal of the Acoustical Society of America*, vol. 19, no. 5, pp. 857–865, 1947, DOI: [10.1121/1.1916631](https://doi.org/10.1121/1.1916631), [PDF].
- [50] F. H. Busse and T. G. Wang, “Torque generated by orthogonal acoustic waves—theory,” *Journal of the Acoustical Society of America*, vol. 69, no. 6, pp. 1634–1638, 1981, DOI: [10.1121/1.385940](https://doi.org/10.1121/1.385940), [PDF].
- [51] H. W. S. Clair, “An electromagnetic sound generator for producing intense high frequency sound,” *Review of Scientific Instruments*, vol. 12, no. 5, pp. 250–256, 1941, DOI: [10.1063/1.1769874](https://doi.org/10.1063/1.1769874), [PDF].
- [52] W. J. Xie, C. D. Cao, Y. J. Lü, and B. Wei, “Levitation of iridium and liquid mercury by ultrasound,” *Physical Review Letters*, vol. 89, p. 104304, 2002, DOI: [10.1103/PhysRevLett.89.104304](https://doi.org/10.1103/PhysRevLett.89.104304), [PDF].

-
- [53] T. H. T. Hatanaka, Y. K. Y. Koike, K. N. K. Nakamura, S. U. S. Ueha, and Y. H. Y. Hashimoto, “Characteristics of underwater near-field acoustic radiation force acting on a planar object,” *Japanese Journal of Applied Physics*, vol. 38, no. 11A, p. L1284, 1999, DOI: [10.1143/JJAP.38.L1284](https://doi.org/10.1143/JJAP.38.L1284), [PDF].
- [54] E. Matsuo, Y. Koike, K. Nakamura, S. Ueha, and Y. Hashimoto, “Holding characteristics of planar objects suspended by near-field acoustic levitation,” *Ultrasonics*, vol. 38, no. 1, pp. 60–63, 2000, DOI: [10.1016/S0041-624X\(99\)00046-3](https://doi.org/10.1016/S0041-624X(99)00046-3), [PDF].
- [55] S. Ueha, Y. Hashimoto, and Y. Koike, “Non-contact transportation using near-field acoustic levitation,” *Ultrasonics*, vol. 38, no. 1, pp. 26–32, 2000, DOI: [10.1016/S0041-624X\(99\)00052-9](https://doi.org/10.1016/S0041-624X(99)00052-9), [PDF].
- [56] H. Nomura, T. Kamakura, and K. Matsuda, “Theoretical and experimental examination of near-field acoustic levitation,” *Journal of the Acoustical Society of America*, vol. 111, no. 4, pp. 1578–1583, 2002, DOI: [10.1121/1.1453452](https://doi.org/10.1121/1.1453452), [PDF].
- [57] A. Minikes, I. Bucher, and S. Haber, “Levitation force induced by pressure radiation in gas squeeze films,” *Journal of the Acoustical Society of America*, vol. 116, no. 1, pp. 217–226, 2004, DOI: [10.1121/1.1760110](https://doi.org/10.1121/1.1760110), [PDF].
- [58] C. Chen, J. Wang, B. Jia, and F. Li, “Design of a noncontact spherical bearing based on near-field acoustic levitation,” *Journal of Intelligent Material Systems and Structures*, vol. 25, no. 6, pp. 755–767, 2014, DOI: [10.1177/1045389X13512903](https://doi.org/10.1177/1045389X13512903), [PDF].
- [59] S. Zhao, S. Mojzisch, and J. Wallaschek, “An ultrasonic levitation journal bearing able to control spindle center position,” *Mechanical Systems and Signal Processing*, vol. 36, no. 1, pp. 168–181, 2013, DOI: [10.1016/j.ymsp.2012.05.006](https://doi.org/10.1016/j.ymsp.2012.05.006), [PDF].
- [60] S. Zhao and J. Wallaschek, “A standing wave acoustic levitation system for large planar objects,” *Archive of Applied Mechanics*, vol. 81, no. 2, pp. 123–139, 2011, DOI: [10.1007/s00419-009-0401-3](https://doi.org/10.1007/s00419-009-0401-3), [PDF].
- [61] M. A. B. Andrade, A. L. Bernassau, and J. C. Adamowski, “Acoustic levitation of a large solid sphere,” *Applied Physics Letters*, vol. 109, no. 4, p. 044101, 2016, DOI: [10.1063/1.4959862](https://doi.org/10.1063/1.4959862), [PDF].

- [62] A. Marzo, S. A. Seah, B. W. Drinkwater, D. R. Sahoo, B. Long, and S. Subramanian, “Holographic acoustic elements for manipulation of levitated objects,” *Nature Communications*, vol. 6, pp. 1–7, 2015, DOI: [10.1038/ncomms9661](https://doi.org/10.1038/ncomms9661), [PDF].
- [63] J. Fletcher, T. Wang, M. Saffren, and D. Elleman, US Patent US3 882 732A, 1975, [PDF].
- [64] A. Haake and J. Dual, “Micro-manipulation of small particles by node position control of an ultrasonic standing wave,” *Ultrasonics*, vol. 40, no. 1, pp. 317–322, 2002, DOI: [10.1016/S0041-624X\(02\)00114-2](https://doi.org/10.1016/S0041-624X(02)00114-2), [PDF].
- [65] C. R. P. Courtney, C.-K. Ong, B. W. Drinkwater, A. L. Bernassau, P. D. Wilcox, and D. R. S. Cumming, “Manipulation of particles in two dimensions using phase controllable ultrasonic standing waves,” *Proceedings of the Royal Society A: Mathematical, Physical and Engineering Sciences*, vol. 468, no. 2138, pp. 337–360, 2012, DOI: [10.1098/rspa.2011.0269](https://doi.org/10.1098/rspa.2011.0269), [PDF].
- [66] T. Matsui, E. Ohdaira, N. Masuzawa, and M. I. M. Ide, “Translation of an object using phase-controlled sound sources in acoustic levitation,” *Japanese Journal of Applied Physics*, vol. 34, no. 5S, p. 2771, 1995, DOI: [10.1143/JJAP.34.2771](https://doi.org/10.1143/JJAP.34.2771), [PDF].
- [67] T. Kozuka, K. Yasui, T. Tuziuti, A. Towata, and Y. Iida, “Non-contact acoustic manipulation in air,” *Japanese Journal of Applied Physics*, vol. 46, no. 7S, p. 4948, 2007, DOI: [10.1143/JJAP.46.4948](https://doi.org/10.1143/JJAP.46.4948), [PDF].
- [68] T. G. Wang, H. Kanber, and I. Rudnick, “First-order torques and solid-body spinning velocities in intense sound fields,” *Phys. Rev. Lett.*, vol. 38, pp. 128–130, 1977, DOI: [10.1103/PhysRevLett.38.128](https://doi.org/10.1103/PhysRevLett.38.128), [PDF].
- [69] Z. Hong, J. Yin, W. Zhai, N. Yan, W. Wang, J. Zhang, and B. W. Drinkwater, “Dynamics of levitated objects in acoustic vortex fields,” *Scientific Reports*, vol. 7, no. 1, pp. 1–7, 2017, DOI: [10.1038/s41598-017-07477-1](https://doi.org/10.1038/s41598-017-07477-1), [PDF].
- [70] B. Zhang, Z. Hong, and B. Drinkwater, “Transfer of orbital angular momentum to freely levitated high-density objects in airborne

- acoustic vortices,” *Phys. Rev. Applied*, vol. 18, p. 024029, 2022, DOI: [10.1103/PhysRevApplied.18.024029](https://doi.org/10.1103/PhysRevApplied.18.024029), [PDF].
- [71] P. Helander, T. Puranen, A. Meriläinen, G. Maconi, A. Penttilä, M. Gritsevich, I. Kassamakov, A. Salmi, K. Muinonen, and E. Hæggström, “Omnidirectional microscopy by ultrasonic sample control,” *Applied Physics Letters*, vol. 116, no. 19, p. 194101, 2020, DOI: [10.1063/5.0002602](https://doi.org/10.1063/5.0002602), [PDF].
- [72] S. Inoue, S. Mogami, T. Ichiyama, A. Noda, Y. Makino, and H. Shinoda, “Acoustical boundary hologram for macroscopic rigid-body levitation,” *Journal of the Acoustical Society of America*, vol. 145, no. 1, pp. 328–337, 2019, DOI: [10.1121/1.5087130](https://doi.org/10.1121/1.5087130), [PDF].
- [73] C. Andersson, “Acoustic levitation of multi-wavelength spherical bodies using transducer arrays of non-specialized geometries,” *Journal of the Acoustical Society of America*, vol. 151, no. 5, pp. 2999–3006, 2022, DOI: [10.1121/10.0010358](https://doi.org/10.1121/10.0010358), [PDF].
- [74] J. Nakahara, B. Yang, and J. R. Smith, “Contact-less manipulation of millimeter-scale objects via ultrasonic levitation,” *8th IEEE RAS/EMBS International Conference for Biomedical Robotics and Biomechanics (BioRob)*, pp. 264–271, 2020, DOI: [10.1109/BioRob49111.2020.9224384](https://doi.org/10.1109/BioRob49111.2020.9224384), [PDF].
- [75] S. Kondo and K. Okubo, “Mid-air acoustic tweezers for non-contact pick up using multi-channel controlled ultrasonic transducer arrays,” *Japanese Journal of Applied Physics*, vol. 60, p. SDDD16, 2021, DOI: [10.35848/1347-4065/abfebd](https://doi.org/10.35848/1347-4065/abfebd), [PDF].
- [76] V. Vandaele, A. Delchambre, and P. Lambert, “Acoustic wave levitation: Handling of components,” *Journal of Applied Physics*, vol. 109, no. 12, p. 124901, 2011, DOI: [10.1063/1.3594245](https://doi.org/10.1063/1.3594245), [PDF].
- [77] Q. Xiu-Pei, G. De-Lu, H. Zhen-Yu, and W. Bing-Bo, “Rotation mechanism of ultrasonically levitated cylinders,” *Acta Physica Sinica*, vol. 66, no. 12, p. 124301, 2017, DOI: [10.7498/aps.66.124301](https://doi.org/10.7498/aps.66.124301), [PDF].
- [78] L. Cox, A. Croxford, B. W. Drinkwater, and A. Marzo, “Acoustic lock: Position and orientation trapping of non-spherical sub-wavelength particles in mid-air using a single-axis acoustic levi-

- tator,” *Applied Physics Letters*, vol. 113, no. 5, p. 054101, 2018, DOI: [10.1063/1.5042518](https://doi.org/10.1063/1.5042518), [PDF].
- [79] S. Gekle and J. M. Gordillo, “Generation and breakup of Worthington jets after cavity collapse. Part 1. Jet formation,” *Journal of Fluid Mechanics*, vol. 663, p. 293–330, 2010, DOI: [10.1017/S0022112010003526](https://doi.org/10.1017/S0022112010003526), [PDF].
- [80] J. M. Gordillo and S. Gekle, “Generation and breakup of Worthington jets after cavity collapse. Part 2. Tip breakup of stretched jets,” *Journal of Fluid Mechanics*, vol. 663, p. 331–346, 2010, DOI: [10.1017/S0022112010003538](https://doi.org/10.1017/S0022112010003538), [PDF].
- [81] M. Nad, “Ultrasonic horn design for ultrasonic machining technologies,” *Applied and Computational Mechanics*, vol. 4, 2010, [PDF]. [Online]. Available: <https://dSPACE5.zcu.cz/bitstream/11025/1392/1/34.pdf>
- [82] J. A. Gallego-Juarez, “Piezoelectric ceramics and ultrasonic transducers,” *Journal of Physics E*, vol. 22, no. 10, p. 804, 1989, DOI: [10.1088/0022-3735/22/10/001](https://doi.org/10.1088/0022-3735/22/10/001), [PDF].
- [83] G. Amza and D. Drimer, “The design and construction of solid concentrators for ultrasonic energy,” *Ultrasonics*, vol. 14, no. 5, pp. 223–226, 1976, DOI: [10.1016/0041-624X\(76\)90022-6](https://doi.org/10.1016/0041-624X(76)90022-6), [PDF].
- [84] X. Lu, J. Twiefel, Z. Ma, T. Yu, J. Wallaschek, and P. Fischer, “Dynamic acoustic levitator based on subwavelength aperture control,” *Advanced Science*, vol. 8, no. 15, p. 2100888, 2021, DOI: [10.1002/advs.202100888](https://doi.org/10.1002/advs.202100888), [PDF].
- [85] M. H. Kandemir and M. Çalışkan, “Standing wave acoustic levitation on an annular plate,” *Journal of Sound and Vibration*, vol. 382, pp. 227 – 237, 2016, DOI: [10.1016/j.jsv.2016.06.043](https://doi.org/10.1016/j.jsv.2016.06.043), [PDF].
- [86] H. Huang and D. Paramo, “Broadband electrical impedance matching for piezoelectric ultrasound transducers,” *IEEE Transactions on Ultrasonics, Ferroelectrics, and Frequency Control*, vol. 58, no. 12, pp. 2699–2707, 2011, DOI: [10.1109/TUFFC.2011.2132](https://doi.org/10.1109/TUFFC.2011.2132), [PDF].
- [87] A. Marzo, M. Caleap, and B. W. Drinkwater, “Acoustic virtual vortices with tunable orbital angular momentum for trapping of

- mie particles,” *Phys. Rev. Lett.*, vol. 120, p. 044301, 2018, DOI: [10.1103/PhysRevLett.120.044301](https://doi.org/10.1103/PhysRevLett.120.044301), [PDF].
- [88] T. Carter, S. Seah, B. Long, B. Drinkwater, and S. Subramanian, “Ultrahaptics: Multi-point mid-air haptic feedback for touch surfaces,” *Proceedings of the 26th Annual ACM Symposium on User Interface Software and Technology (UIST)*, pp. 505–514, 2013, DOI: [10.1145/2501988.2502018](https://doi.org/10.1145/2501988.2502018), [PDF].
- [89] M. Röthlisberger, M. Schuck, L. Kulmer, and J. W. Kolar, “Contactless picking of objects using an acoustic gripper,” *Actuators*, vol. 10, no. 4, 2021, DOI: [10.3390/act10040070](https://doi.org/10.3390/act10040070), [PDF].
- [90] G. Allevato, T. Fregy, C. Haugwitz, M. Rutsch, J. Hinrichs, R. Müller, M. Pesavento, and M. Kupnik, “Calibration of air-coupled ultrasonic phased arrays. Is it worth it?” *International Ultrasonics Symposium (IUS)*, 2022, [PDF].
- [91] T. Fushimi, “Nonlinear dynamics of phased array levitators,” Ph.D. dissertation, University of Bristol, 2020, [PDF].
- [92] M. Röthlisberger, M. Schuck, and J. W. Kolar, “Kilohertz-frequency rotation of acoustically levitated particles,” *IEEE Transactions on Ultrasonics, Ferroelectrics, and Frequency Control*, vol. 69, no. 4, pp. 1528–1534, 2022, DOI: [10.1109/TUFFC.2022.3149131](https://doi.org/10.1109/TUFFC.2022.3149131), [PDF].
- [93] T. Puranen, P. Helander, A. Meriläinen, G. Maconi, A. Penttilä, M. Gritsevich, I. Kassamakov, A. Salmi, K. Muinonen, and E. Hæggström, “Multifrequency acoustic levitation,” *IEEE International Ultrasonics Symposium (IUS)*, pp. 916–919, 2019, DOI: [10.1109/ULTSYM.2019.8926200](https://doi.org/10.1109/ULTSYM.2019.8926200), [PDF].
- [94] A. Marzo and B. Drinkwater, “Holographic acoustic tweezers,” *Proceedings of the National Academy of Sciences*, vol. 116, p. 201813047, 2018, DOI: [10.1073/pnas.1813047115](https://doi.org/10.1073/pnas.1813047115), [PDF].
- [95] A. Marzo, A. Ghobrial, L. Cox, M. Caleap, A. Croxford, and B. W. Drinkwater, “Realization of compact tractor beams using acoustic delay-lines,” *Applied Physics Letters*, vol. 110, no. 1, p. 014102, 2017, DOI: [10.1063/1.4972407](https://doi.org/10.1063/1.4972407), [PDF].

- [96] C. Woehler, *3D Computer Vision*. Springer-Verlag London, 2013, DOI: [10.1007/978-1-4471-4150-1](https://doi.org/10.1007/978-1-4471-4150-1), [PDF].
- [97] P. Sturm, *Pinhole Camera Model*. Springer US, Boston, 2014, pp. 610–613, DOI: [10.1007/978-0-387-31439-6](https://doi.org/10.1007/978-0-387-31439-6), [PDF].
- [98] D. Kaur and Y. Kaur, “Various image segmentation techniques: A review,” *International Journal of Computer Science and Mobile Computing*, 2014, [PDF]. [Online]. Available: <http://ijcsmc.com/docs/papers/May2014/V3I5201499a84.pdf>
- [99] S. Skogestad and I. Postlethwaite, *Multivariable Feedback Control - Analysis and Design*. John Wiley and Sons, 2005, [PDF].
- [100] V. T. Rathod, “A review of electric impedance matching techniques for piezoelectric sensors, actuators and transducers,” *Electronics*, vol. 8, no. 2, p. 169, 2019, DOI: [10.3390/electronics8020169](https://doi.org/10.3390/electronics8020169), [PDF].
- [101] F. P. Bowden and R. G. Lord, “The aerodynamic resistance to a sphere rotating at high speed,” *Proceedings of the Royal Society of London. Series A. Mathematical and Physical Sciences*, vol. 271, no. 1345, pp. 143–153, 1963, DOI: [10.1098/rspa.1963.0010](https://doi.org/10.1098/rspa.1963.0010), [PDF].
- [102] F. Nelli, *Image Analysis and Computer Vision with OpenCV*. Apress, 2018, DOI: [10.1007/978-1-4842-3913-1](https://doi.org/10.1007/978-1-4842-3913-1), [PDF].
- [103] T. Fushimi, A. Marzo, B. W. Drinkwater, and T. L. Hill, “Acoustophoretic volumetric displays using a fast-moving levitated particle,” *Applied Physics Letters*, 2019, DOI: [10.1063/1.5113467](https://doi.org/10.1063/1.5113467), [PDF].
- [104] M. Röthlisberger, M. Schuck, L. Kulmer, and J. W. Kolar, “Automated insertion of objects into an acoustic robotic gripper,” *1st International Electronic Conference on Actuator Technology: Materials, Devices and Applications*, vol. 64, no. 1, 2020, DOI: [10.3390/IeCAT2020-08510](https://doi.org/10.3390/IeCAT2020-08510), [PDF].
- [105] L. Savioja and U. P. Svensson, “Overview of geometrical room acoustic modeling techniques,” *Journal of the Acoustical Society of America*, vol. 138, no. 2, pp. 708–730, 2015, DOI: [10.1121/1.4926438](https://doi.org/10.1121/1.4926438), [PDF].

-
- [106] A. Rathnayake and W. K. Wanniarachchi, “Image source method based acoustic simulation for 3-D room environment,” *International Journal of Scientific and Technology Research*, vol. 8, pp. 222–228, 2019, [PDF]. [Online]. Available: <http://dr.lib.sjp.ac.lk/handle/123456789/12354>
- [107] T. Schwarz, P. Hahn, G. Petit-Pierre, and J. Dual, “Rotation of fibers and other non-spherical particles by the acoustic radiation torque,” *Microfluidics and Nanofluidics*, vol. 18, no. 1, pp. 65–79, 2015, DOI: [10.1007/s10404-014-1408-9](https://doi.org/10.1007/s10404-014-1408-9), [PDF].
- [108] M. Röthlisberger, T. Wilhelm, M. Schuck, and J. W. Kolar, “Contactless positioning of objects on acoustically reflective surfaces by means of ultrasonic forces,” *International Ultrasonics Symposium (IUS)*, 2022, [PDF].
- [109] M. A. B. Andrade, T. S. A. Camargo, and A. Marzo, “Automatic contactless injection, transportation, merging, and ejection of droplets with a multifocal point acoustic levitator,” *Review of Scientific Instruments*, vol. 89, no. 12, p. 125105, 2018, DOI: [10.1063/1.5063715](https://doi.org/10.1063/1.5063715), [PDF].
- [110] R. Ellson, “Picoliter: Enabling precise transfer of nanoliter and picoliter volumes,” *Drug Discovery Today*, vol. 7, 2002, DOI: [10.1016/S1359-6446\(02\)02176-1](https://doi.org/10.1016/S1359-6446(02)02176-1), [PDF].
- [111] R. Ellson, M. Mutz, B. Browning, L. J. Lee, M. F. J. Miller, and R. J. Papen, “Transfer of low nanoliter volumes between microplates using focused acoustics - automation considerations,” *JALA: Journal of the Association for Laboratory Automation*, vol. 8, no. 5, pp. 29–34, 2003, DOI: [10.1016/S1535-5535-03-00011-X](https://doi.org/10.1016/S1535-5535-03-00011-X), [PDF].
- [112] D. Harris, M. Mutz, M. Sonntag, R. Stearns, J. Shieh, S. Pickett, R. Ellson, and J. Olechno, “Low nanoliter acoustic transfer of aqueous fluids with high precision and accuracy of volume transfer and positional placement,” *JALA: Journal of the Association for Laboratory Automation*, vol. 13, no. 2, pp. 97–102, 2008, DOI: [10.1016/j.jala.2007.12.002](https://doi.org/10.1016/j.jala.2007.12.002), [PDF].
- [113] J. Olechno, C. Green, and L. Rasmussen, “Why a special issue on acoustic liquid handling?” *Journal of Laboratory Automation*,

- vol. 21, no. 1, pp. 1–3, 2016, DOI: [10.1177/2211068215619712](https://doi.org/10.1177/2211068215619712), [PDF].
- [114] J. Olechno, R. Stearns, R. Ellson, and E. Heron, “Acoustic droplet ejection technology,” *Innovations in Pharmaceutical Technology*, vol. 19, p. 40, 2019, [PDF]. [Online]. Available: https://www.researchgate.net/publication/333985097_Acoustic_Droplet_Ejection_Technology
- [115] S. A. Elrod, B. Hadimioglu, B. T. Khuri-Yakub, E. G. Rawson, E. Richley, C. F. Quate, N. N. Mansour, and T. S. Lundgren, “Nozzleless droplet formation with focused acoustic beams,” *Journal of Applied Physics*, vol. 65, no. 9, pp. 3441–3447, 1989, DOI: [10.1063/1.342663](https://doi.org/10.1063/1.342663), [PDF].
- [116] B. Hadimioglu, R. Stearns, and R. Ellson, “Moving liquids with sound: The physics of acoustic droplet ejection for robust laboratory automation in life sciences,” *Journal of Laboratory Automation*, vol. 21, no. 1, pp. 4–18, 2016, DOI: [10.1177/2211068215615096](https://doi.org/10.1177/2211068215615096), [PDF].
- [117] A. Nadim and J. Sterling, *Transport of Droplets by Acoustics*, 2015, DOI: “[10.1007/978-3-642-27758-0](https://doi.org/10.1007/978-3-642-27758-0)”, [PDF].
- [118] F. Madoux, A. Tanner, M. Vessels, L. Willetts, S. Hou, L. Scampavia, and T. Spicer, “A 1536-well 3D viability assay to assess the cytotoxic effect of drugs on spheroids,” *SLAS Discovery*, vol. 0, p. 247255521668630, 2017, DOI: [10.1177/2472555216686308](https://doi.org/10.1177/2472555216686308), [PDF].
- [119] J. Saarela, E. Kuleskiy, K. Laamanen, T. Pemovska, V. Pietiäinen, S. Potdar, C. von Schantz-Fant, L. Turunen, P. Östling, and K. Wennerberg, “A personalised medicine drug sensitivity and resistance testing platform and utilisation of acoustic droplet ejection at the institute for molecular medicine finland,” *Synergy*, vol. 1, no. 1, p. 78, 2014, DOI: [10.1016/j.synres.2014.07.001](https://doi.org/10.1016/j.synres.2014.07.001), [PDF].
- [120] J. Naylor, A. Rossi, and D. C. Hornigold, “Acoustic dispensing preserves the potency of therapeutic peptides throughout the entire drug discovery workflow,” *Journal of Laboratory Automation*, vol. 21, no. 1, pp. 90–96, 2016, DOI: [10.1177/2211068215587915](https://doi.org/10.1177/2211068215587915), [PDF].

- [121] K. Cross, R. Craggs, D. Swift, A. Sitaram, S. Daya, M. Roberts, S. Hawley, P. Owen, and B. Isherwood, “Delivering an automated and integrated approach to combination screening using acoustic-droplet technology,” *SLAS Technology*, vol. 21, no. 1, pp. 143–152, 2016, DOI: [10.1177/2211068215579163](https://doi.org/10.1177/2211068215579163), [PDF].
- [122] E. Salzer, E. Nixon, G. Drewes, F. Reinhard, G. Bergamini, and C. Rau, “Screening pools of compounds against multiple endogenously expressed targets in a chemoproteomics binding assay.” *Journal of Laboratory Automation*, vol. 21, pp. 133–42, 2016, DOI: [10.1177/2211068215595355](https://doi.org/10.1177/2211068215595355), [PDF].
- [123] T. D. Dawes, R. Turincio, S. W. Jones, R. A. Rodriguez, D. Gadiagellan, P. Thana, K. R. Clark, A. E. Gustafson, L. Orren, M. Liimatta, D. P. Gross, T. Maurer, and M. H. Beresini, “Compound transfer by acoustic droplet ejection promotes quality and efficiency in ultra-high-throughput screening campaigns.” *Journal of Laboratory Automation*, vol. 21, pp. 64–75, 2016, DOI: [10.1177/2211068215590588](https://doi.org/10.1177/2211068215590588), [PDF].
- [124] C. Cain-Hom, R. Pabalate, A. Pham, H. N. Patel, R. Wiler, and J. C. Cox, “Mammalian genotyping using acoustic droplet ejection for enhanced data reproducibility, superior throughput, and minimized cross-contamination,” *Journal of Laboratory Automation*, vol. 21, no. 1, pp. 37–48, 2016, DOI: [10.1177/2211068215601637](https://doi.org/10.1177/2211068215601637), [PDF].
- [125] M. Y. Mayday, L. M. Khan, E. D. Chow, M. S. Zinter, and J. L. DeRisi, “Miniaturization and optimization of 384-well compatible RNA sequencing library preparation.” *PLOS One*, vol. 14, p. e0206194, 2019, DOI: [10.1371/journal.pone.0206194](https://doi.org/10.1371/journal.pone.0206194), [PDF].
- [126] P. Kanigowska, Y. Shen, Y. Zheng, S. Rosser, and Y. Cai, “Smart DNA fabrication using sound waves: Applying acoustic dispensing technologies to synthetic biology.” *Journal of Laboratory Automation*, vol. 21, pp. 49–56, 2016, DOI: [10.1177/2211068215593754](https://doi.org/10.1177/2211068215593754), [PDF].
- [127] E. B. Shapland, V. Holmes, C. D. Reeves, E. Sorokin, M. Durot, D. Platt, C. Allen, J. Dean, Z. Serber, J. Newman, and S. Chandran, “Low-cost, high-throughput sequencing of DNA assemblies

- using a highly multiplexed nextera process,” *ACS Synth. Biol.*, vol. 4, no. 7, pp. 860–866, 2015, DOI: [10.1021/sb500362n](https://doi.org/10.1021/sb500362n), [PDF].
- [128] L. A. Mitchell, L. H. McCulloch, S. Pinglay, H. Berger, N. Bosco, R. Brosh, M. Bulajić, E. Huang, M. S. Hogan, J. A. Martin, E. O. Mazzoni, T. Davoli, M. T. Maurano, and J. D. Boeke, “De novo assembly and delivery to mouse cells of a 101 kb functional human gene.” *Genetics*, vol. 218, 2021, DOI: [10.1093/genetics/iyab038](https://doi.org/10.1093/genetics/iyab038), [PDF].
- [129] J. Rong, I. Pass, P. W. Diaz, T. A. Ngo, M. Sauer, G. Magnusson, F.-Y. Zeng, C. A. Hassig, M. R. Jackson, N. D. P. Cosford, S.-I. Matsuzawa, and J. C. Reed, “Cell-based high-throughput luciferase reporter gene assays for identifying and profiling chemical modulators of endoplasmic reticulum signaling protein, IRE1.” *Journal of Biomolecular Screening*, vol. 20, pp. 1232–45, 2015, DOI: [10.1177/1087057115600414](https://doi.org/10.1177/1087057115600414), [PDF].
- [130] D. L. Ericson, X. Yin, A. Scalia, Y. N. Samara, R. Stearns, H. Vlahos, R. Ellson, R. M. Sweet, and A. S. Soares, “Acoustic methods to monitor protein crystallization and to detect protein crystals in suspensions of agarose and lipidic cubic phase.” *Journal of Laboratory Automation*, vol. 21, pp. 107–14, 2016, DOI: [10.1177/2211068215616365](https://doi.org/10.1177/2211068215616365), [PDF].
- [131] L. B. Pinheiro, H. O’Brien, J. Druce, H. Do, P. Kay, M. Daniels, J. You, D. Burke, K. Griffiths, and K. R. Emslie, “Interlaboratory reproducibility of droplet digital polymerase chain reaction using a new DNA reference material format.” *Analytical Chemistry*, vol. 89, pp. 11 243–11 251, 2017, DOI: [10.1021/acs.analchem.6b05032](https://doi.org/10.1021/acs.analchem.6b05032), [PDF].
- [132] E. Kuleskiy, J. Saarela, L. Turunen, and K. Wennerberg, “Precision cancer medicine in the acoustic dispensing era: Ex vivo primary cell drug sensitivity testing.” *Journal of Laboratory Automation*, vol. 21, pp. 27–36, 2016, DOI: [10.1177/2211068215618869](https://doi.org/10.1177/2211068215618869), [PDF].
- [133] K. Blom, P. Nygren, J. Alvarsson, R. Larsson, and C. R. Andersson, “Ex vivo assessment of drug activity in patient tumor cells as a basis for tailored cancer therapy.” *Journal of Laboratory Automation*, vol. 21, pp. 178–87, 2016, DOI: [10.1177/2211068215598117](https://doi.org/10.1177/2211068215598117), [PDF].

- [134] E. K. Sackmann, L. Majlof, A. Hahn-Windgassen, B. Eaton, T. Bandzava, J. Daulton, A. Vandenbroucke, M. Mock, R. G. Stearns, S. Hinkson, and S. S. Datwani, “Technologies that enable accurate and precise nano- to milliliter-scale liquid dispensing of aqueous reagents using acoustic droplet ejection.” *Journal of Laboratory Automation*, vol. 21, pp. 166–77, 2016, DOI: [10.1177/2211068215602191](https://doi.org/10.1177/2211068215602191), [PDF].
- [135] S. Gekle, J. M. Gordillo, D. van der Meer, and D. Lohse, “High-speed jet formation after solid object impact,” *Phys. Rev. Lett.*, vol. 102, pp. 595–598, 2009, DOI: [10.1103/PhysRevLett.102.034502](https://doi.org/10.1103/PhysRevLett.102.034502), [PDF].
- [136] B. W. Zeff, B. Kleber, J. Fineberg, and D. P. Lathrop, “Singularity dynamics in curvature collapse and jet eruption on a fluid surface,” *Nature*, vol. 403, no. 6768, pp. 401–404, 2000, DOI: [10.1038/35000151](https://doi.org/10.1038/35000151), [PDF].
- [137] C. J. M. van Rijn, J. Westerweel, B. van Brummen, A. Antkowiak, and D. Bonn, “Self-similar jet evolution after drop impact on a liquid surface,” *Phys. Rev. Fluids*, vol. 6, p. 034801, 2021, DOI: [10.1103/PhysRevFluids.6.034801](https://doi.org/10.1103/PhysRevFluids.6.034801), [PDF].
- [138] F. E. Loranca-Ramos, J. L. Carrillo-Estrada, and F. Pacheco-Vázquez, “Craters and granular jets generated by underground cavity collapse,” *Phys. Rev. Lett.*, vol. 115, p. 028001, 2015, DOI: [10.1103/PhysRevLett.115.028001](https://doi.org/10.1103/PhysRevLett.115.028001), [PDF].
- [139] D. Zang, Y. Yu, Z. Chen, X. Li, H. Wu, and X. Geng, “Acoustic levitation of liquid drops: Dynamics, manipulation and phase transitions,” *Advances in Colloid and Interface Science*, vol. 243, pp. 77–85, 2017, DOI: [10.1016/j.cis.2017.03.003](https://doi.org/10.1016/j.cis.2017.03.003), [PDF].
- [140] R. H. Morris, E. R. Dye, P. Docker, and M. I. Newton, “Beyond the Langevin horn: Transducer arrays for the acoustic levitation of liquid drops,” *Physics of Fluids*, vol. 31, no. 10, p. 101301, 2019, DOI: [10.1063/1.5117335](https://doi.org/10.1063/1.5117335), [PDF].
- [141] A. Toepler, *Beobachtungen nach einer neuen optischen Methode*. Cohen, 1864, [PDF]. [Online]. Available: <https://www.digitale-sammlungen.de/view/bsb10134892>

- [142] M. Biss, G. Settles, M. Hargather, L. Dodson, and J. Miller, “High-speed digital shadowgraphy of shock waves from explosions and gunshots,” *26th International Symposium on Shock Waves*, pp. 91–96, 2009, DOI: [10.1007/978-3-540-85168-4](https://doi.org/10.1007/978-3-540-85168-4), [PDF].
- [143] F. R. Chromey, *To Measure the Sky: An Introduction to Observational Astronomy*, 2nd ed. Cambridge University Press, 2016, DOI: [10.1017/CBO9781316424117](https://doi.org/10.1017/CBO9781316424117), [PDF].
- [144] L. Mrňa, J. Pavelka, P. Horník, and J. Hrabovský, “Use of Schlieren methods to study gas flow in laser technology,” *Optics and Measurement International Conference 2016*, 2016, DOI: [10.1117/12.2257212](https://doi.org/10.1117/12.2257212), [PDF].
- [145] M. J. Hargather and G. S. Settles, “Natural-background-oriented Schlieren imaging,” *Experiments in Fluids*, vol. 48, no. 1, pp. 59–68, 2009, DOI: [10.1007/s00348-009-0709-3](https://doi.org/10.1007/s00348-009-0709-3), [PDF].
- [146] G. S. Settles, *Schlieren and Shadowgraph Techniques*. Springer Berlin Heidelberg, 2006, DOI: [10.1007/978-3-642-56640-0](https://doi.org/10.1007/978-3-642-56640-0), [PDF].
- [147] V. Contreras and A. Marzo, “Adjusting single-axis acoustic levitators in real time using rainbow Schlieren deflectometry,” *Review of Scientific Instruments*, vol. 92, no. 1, p. 015107, 2021, DOI: [10.1063/5.0013347](https://doi.org/10.1063/5.0013347), [PDF].
- [148] Akademische Raumfahrt Initiative Schweiz, “ARIS Annual Report 2020/21,” ETH Zurich, Tech. Rep., 2021.

Curriculum Vitae

Personal Information

Name	Marc Röthlisberger
Date of birth	August 6, 1995
Nationality	Swiss
Citizen of	Ballwil, Switzerland

Education

2019 – 2022	Doctorate, ETH Zurich Power Electronic Systems Laboratory (PES)
2017 – 2019	MSc ETH, ETH Zurich Information Technology and Electrical Engineering
2013 – 2016	BSc ETH, ETH Zurich Information Technology and Electrical Engineering
2007 – 2013	High School, Baldegg Physics and Applied Mathematics

Work Experience

2020 – 2021	Chief Technology Officer at No-Touch Robotics
2018 – 2018	Research Assistant, ETH Zurich Seminar for Applied Mathematics (SAM)
2014 – 2018	Teaching Project at Primary Schools Ausbildungs- und Beratungszentrum für Informatikunterricht
2014 – 2014	Teaching Assistant, ETH Zurich Integrated Systems Laboratory (IIS)